The Polymers, Composites, 3BsMaterials 2025 International Joint Conferences

April 16 to 18 2025, Albufeira, Portugal

Conference Proceedings

DOI:

https://doi.org/10.26799/cp-polymers-composites-3Bsmaterials-2025

Proceedings of the Polymers, Composites, 3BsMaterials 2025 Joint International Conferences
AlBufeira, Portugal – April 16 – 18, 2025
DOI: https://doi.org/10.26799/cp-polymers-composites-3Bsmaterials-2025

Prediction of Proof Test Outcomes for Type 4 High Pressure Hydrogen Vessels with Composite Layers Using Machine Learning Models

Lina ACHOUR[1,2], Sébastien DESTERCKE[3], Benedict MARTUS[4], David CHARRY[4], Zoheir ABOURA[1], Kamel KHELLIL[1]

[1.] Université de technologie de Compiègne, Roberval, Compiègne, France
lina.achour@utc.fr, zoheir.aboura@utc.fr and kamel.khellil@utc.fr
[2.] H2-Power, OPmobility. ZAC du Bois de Plaisance, 214 Avenue de la Mare Gessart, 60280 Venette
[3.] Université de technologie de Compiègne, CNRS, Heudiasyc, Compiègne, France
sebastien.destercke@hds.utc.fr
[4.] Université de technologie de Compiègne. 60200 Compiègne
benedict.martus@etu.utc.fr and david.charry@etu.utc.fr

Abstract

This study presents a machine learning-based approach for predicting the outcome of the Proof Test, a critical mechanical compliance test on Type IV high-pressure hydrogen vessels (HPVs). These vessels, composed of a polymer liner and carbon composite layers, undergo extreme pressure testing to verify their structural integrity and safety. The goal is to provide a fast and reliable predictive tool to anticipate test outcomes using process parameters collected during the filament winding stage. The dataset consists of 233 vessels, with over 180 passing the test, resulting in a natural class imbalance. 54 production parameters were averaged per vessel to create a compact feature set. Missing values were imputed using a conditional interpolation strategy based on similar test outcomes. A Random Forest classifier was trained using 70% of the data and evaluated on the remaining 30%, achieving 94% accuracy and a ROC-AUC of 0.8686. The confusion matrix reveals strong performances, particularly in identifying failed vessels, with very few false negatives. Feature importance analysis identified winding speed as the most critical variable, followed by winding time, liner inner pressure, doctor blade settings, and fiber tension. However, the relatively low individual importance scores highlight the potential significance of nonlinear interactions between parameters. A preliminary comparison with Burst Test results also supports the model's potential as a non-destructive validation tool. Overall, this work demonstrates the feasibility of integrating machine learning into composite vessel manufacturing, offering a path toward reduced testing costs, enhanced safety, and greater automation in the hydrogen industry.

Keywords: Composite/Polymer structures, Type IV hydrogen vessels, Proof Test, filament winding, machine learning, Random Forest, predictive maintenance, non-destructive validation.

1. Introduction

High-pressure hydrogen vessels of Type IV (HPV) are essential components for hydrogen storage in fuel cell vehicles and other mobility or industrial applications. These vessels are composed of a polymer liner surrounded by carbon fiber-reinforced composite layers, offering the dual benefits of light weight and high mechanical performance [1]. Their structural configuration ensures resistance to fatigue and internal pressure, while maintaining durability and safety over repeated load cycles [2].

A key phase in the qualification of these vessels is the Proof Test, a mechanical resistance test performed at 1.5 times the normal working pressure to verify the vessel's structural integrity before it enters service. This critical step assesses the vessel's ability to withstand extreme pressure conditions, ensuring its safety and compliance [3] . Despite the robust design of these vessels, process variability during manufacturing, particularly in the wet filament winding stage can lead to inconsistencies in performance and occasional failures during this test. Each vessel comprises multiple winding layers, and a wide range of process parameters (temperature, speed, tension, resin application, etc.) influence the quality of the final structure.

DOI: https://doi.org/10.26799/cp-polymers-composites-3Bsmaterials-2025

Given the complexity of the manufacturing process and the multitude of interacting variables, purely physical modeling approaches to predict compliance test outcomes are neither scalable nor practical. Instead, data-driven methods, and more specifically machine learning, offer a promising alternative. These methods are well suited to model nonlinear interactions and capture weak signals within large datasets, even in the presence of class imbalance.

In this work, we propose a predictive model based on a Random Forest Classifier to anticipate the outcome of the Proof Test using production parameters collected in real-time. The goal is to develop a robust, interpretable, and scalable approach to assist manufacturers in identifying potential failures early in the process, reducing reliance on costly physical testing and supporting a move toward test automation and zero-reject production in the hydrogen storage industry. The article is structured as follows: Section 2 presents the methodology, including data acquisition, preprocessing, and modeling approach. Section 3 discusses the model's predictive performance and interprets the influence of key process parameters. Section 4 concludes with the main findings, practical implications, and future research directions aimed at extending this work toward broader structural performance evaluation.

2. Methodology

This study is based on data collected from the continuous wet filament winding production of 233 Type IV hydrogen vessels. For each vessel, 54 process parameters such as winding speed, resin temperature, tension, and inner liner pressure were monitored across all winding layers. To construct a compact and consistent dataset, the values of each parameter were averaged across all winding layers per vessel, capturing the overall production behavior while reducing dimensionality.

As is common in industrial environments, sensor readings sometimes included missing or faulty values. These were treated by interpolation using average values from vessels sharing the same Proof Test outcome, under the assumption that similar test results reflect comparable process characteristics.

One of the major challenges in this study lies in the inherent class imbalance: while over 180 vessels passed the Proof Test, only about 40 failed. This imbalance can distort the learning process by favoring the dominant class, requiring specific corrective measures during model training [4] [5] [6] [7]. We used a Random Forest Classifier [8] due to its robustness against overfitting and its ability to handle nonlinear interactions. The dataset was split into 70% for model training and 30% for testing. This split ensures that the model's predictive ability is evaluated on unseen data while preserving enough cases for effective learning. Performance evaluation relied on multiple indicators, including accuracy, ROC-AUC score, and the confusion matrix, which together provided a detailed view of how well the model distinguishes between passing and failing vessels. Given the class imbalance and the moderate size of the dataset, special care was taken to avoid bias and ensure meaningful learning of patterns associated with both outcomes.

3. Results and discussion

The Random Forest model achieved a test accuracy of 94% and an ROC-AUC of 0.8686, see Table 1 for more detailed results. The confusion matrix (Fig. 1) revealed 56 true positives (passed/predicted passed), 10 true negatives (failed/predicted failed), and only 4 false negatives (predicted passed but actually failed), which is critical for safety applications.

		Predicted class	
		Proof test OK	Proof test NOK
True class	Proof test OK	56	0
	Proof test NOK	4	10

Figure 1: Confusion matrix.

Table 1: Random forest classifier performances

DOI: https://doi.org/10.26799/cp-polymers-composites-3Bsmaterials-2025

Class	Precision	Recall	F1-Score	Support
Proof test OK	0.93	1.00	0.97	56
Proof test Nok	1.00	0.71	0.83	14
Accuracy			**0.94**	70

The Random Forest algorithm, in addition to its predictive capabilities, provides a ranking of feature importance, which revealed that winding speed emerged as the most influential parameter in predicting the outcome of the Proof Test, followed by winding time (i.e., the total time required to complete the filament winding of each vessel), liner inner pressure (measured during winding to ensure the liner maintains its shape), doctor blade (a component that regulates the amount of resin applied to the fibers during impregnation) setting, and fiber tension. This ranking aligns with hypotheses found in the literature, which suggest that these parameters are closely linked to the structural quality and mechanical integrity of Type IV hydrogen vessel [9].

Winding speed, in particular, plays a critical role in the placement quality and consistency of carbon fibers. If the speed is too high, it may lead to misalignment or poor fiber compaction, whereas speeds that are too low could affect production efficiency and resin distribution. In both cases, deviations from optimal winding speed can compromise fiber architecture, leading to stress concentration zones or defects that reduce the vessel's resistance under pressure, as validated by its high importance in our model.

Winding time, which corresponds to the total time taken to complete the filament winding of a vessel, is inherently linked to process control. A longer winding time may reflect a slower, more controlled deposition of fibers, improving homogeneity and adhesion between layers factors that can enhance overall mechanical performance.

Liner inner pressure, maintained during winding, ensures the polymer liner retains its geometry under the forces of fiber deposition. Inadequate internal pressure may result in liner deformation, creating defects or poor contact at the liner-composite interface, which in turn could weaken the vessel's resistance during the Proof Test.

The Doctor blade, which regulates the amount of resin deposited on the fibers before winding, directly affects resin-fiber impregnation quality. An insufficient or excessive resin layer may impair the fiber-matrix bond, compromising the structural cohesion and mechanical properties of the composite shell.

Finally, fiber tension influences the alignment and compaction of the fibers within the composite. Improper tension can lead to waviness, gaps, or stress irregularities, reducing the vessel's ability to withstand internal pressure.

However, the relatively low absolute importance values (with the highest around 0.22 on a normalized scale where the maximum possible is 1) indicate that no single parameter solely drives the model's decisions. Instead, these results underscore the complex interplay and nonlinear interactions among parameters during the filament winding process supporting the use of machine learning methods capable of capturing such dependencies, which are difficult to capture using purely physical models.

4. Conclusion

This study demonstrates the potential of machine learning specifically a Random Forest classifier to predict the outcome of the Proof Test for Type IV high-pressure hydrogen vessels based on real-time production data. Despite the complexity of the filament winding process and the imbalance in the dataset, the model achieved a high accuracy of 94%, correctly identifying both compliant and non-compliant vessels. Feature importance analysis highlighted winding speed as the most influential parameter, followed by winding time, liner inner pressure, doctor blade setting, and fiber tension. These results are consistent with literature, which underscores the critical role of process control in ensuring the mechanical integrity of composite vessels.

DOI: https://doi.org/10.26799/cp-polymers-composites-3Bsmaterials-2025

Beyond predictive performance, this approach offers practical advantages: early detection of at-risk vessels, reduction of costly destructive testing, and enhanced process monitoring. However, the current model's performance remains dependent on the quality and quantity of available data. Future work will aim to enrich the dataset with additional samples and parameters, explore the influence of parameter interactions in greater depth, and investigate the feasibility of extending the model to predict other destructive test outcomes, such as porosity content and Burst test results. Preliminary steps in this direction have already been initiated by comparing Proof Test predictions with actual Burst Test results for a small set of vessels. While these two tests assess different mechanical thresholds, they are both influenced by the same underlying manufacturing conditions. By using our model to predict Proof Test outcomes for vessels that had already undergone the Burst Test, we aismed to explore whether the model's decisions could reflect broader structural performance. This cross-comparison offers an initial step toward extending our approach as a potential proxy for multiple validation tests and reducing reliance on systematic destructive testing. This direction holds promise for developing robust, data-driven quality control tools that complement physical testing and support more efficient and reliable hydrogen vessel production.

Acknowledgements

This project is carried out in cooperation with OPmobility.

References

[1] M. Ravichandran et al, *Recent developments in Polymer Matrix Composites – A review.* IOP Conference Series: Materials Science and Engineering, 988(1), 012096, 2020.

[2] B. Patamaprohm, *Conception et durabilité de réservoirs en composites destinés au stockage de l'hydrogène*, Ecole Nationale Supérieure des Mines de Paris, 2014.

[3] E. Lainé et al, *Instrumented tests on composite pres-sure vessels (type IV) under internal wa-ter pressure.* International Journal of Hydrogen Energy, 2021, vol. 46, no 1, p. 1334-1346.

[4] C. Gilets et al, *Softmin discrete minimax classifier for imbalanced classes and prior probability shifts.* Machine Learning, 2024, vol. 113, no 2, p. 605-645.

[5] H. Haibo et E. A. Garcia, *Learning from imbalanced data. IEEE Transactions on knowledge and engineering 21(9), 1263–1284*, 2009.

[6] A. Kumar et al, *A review on unbalanced data classification*. In Proceedings of International Joint Conference on Advances in Computational Intelligence: IJCACI 2021,pp. 197–208. Springer, 2022.

[7] L. Wang et al, *Review of classification methods on unbalanced data sets*. Ieee Access 9, 64606–64628, 2021.

[8] A. Parmar et al, *A review on random forest: An ensemble classifier.* In : International conference on intelligent data communication technologies and internet of things (ICICI) 2018. Springer International Publishing,2019. p. 758-763.

[9] R. Rehma et al, *Numerical analysis of the impact of winding angles on the mechanical performance of filament wound type 4 composite pressure vessels for compressed hydrogen gas storage,* Heliyon. 2024 Jun 29;10(13):e33796. doi: 10.1016/j.heliyon.2024.e33796. PMID: 39050469; PMCID: PMC11267002.

Proceedings of the Polymers, Composites, 3BsMaterials 2025 Joint International Conferences
AlBufeira, Portugal – April 16 – 18, 2025
DOI: https://doi.org/10.26799/cp-polymers-composites-3Bsmaterials-2025

Development of infrared polymer optical filters based on sulfur and cross-linking agents

Morgane Guerchoux[1], Olivier Muller[1], Célia Bruder[1], Vadim Allheily[1], Nicolas Requier[1], Bastien Lallemand[1], Anne-Sophie Schuller[2], Christelle Delaite[2], Lionel Merlat[1]

[1] French-German Research Institute of Saint-Louis (ISL), Saint-Louis, France / [2] Laboratory of photochemistry and macromolecular engineering of Mulhouse - EA4567 (LPIM), University of Haute-Alsace (UHA), Mulhouse, France
Morgane.guerchoux@isl.eu / Olivier.muller@isl.eu

Abstract
Based on the inverse vulcanization process, sulfur-based polymers were developed for optical purposes in the infrared spectral range using divinylbenzene (DVB) as a cross-linking agent to stabilize the system. Differential scanning calorimetry (DSC) revealed a good thermal stability for the ratio S-DVB 50 wt% - 50 wt% composition, with a glass transition temperature (Tg) above 60 °C. FT-IR spectroscopy showed a broad transmission range between 2 and 5 µm, with an absorption band between 3.2 and 3.6 µm and a maximum of 61 % at 3 µm which is still below that of germanium, a conventional IR material used as reference in this study. The structural similarity index measure (SSIM) yielded values close to 1, indicating minimal wavefront distortion.

Keywords: MWIR, optical filters, sulfur-based polymers, divinylbenzene, inverse vulcanization process

1. Introduction
Numerous applications [1] operate within an infrared spectral range from 2 to 5 µm, including mid-wave infrared (MWIR) thermal imaging, gas detection spectroscopy, and more. Infrared (IR) applications require the use of IR-transparent materials [2] such as germanium, zinc selenide, or chalcogenide glasses. While widely used, these materials have some drawbacks: they are expensive, potentially toxic, and often difficult to process. These limitations have prompted extensive research efforts to identify alternative IR materials.
Sulfur exhibits interesting properties in the infrared region [1],[2]- namely a high transparency in the IR spectrum- and is primarily obtained as a byproduct of petroleum refining. When heated, elemental sulfur (S_8) undergoes ring-opening and can self-polymerize. However, the resulting polymer is unstable over time. To overcome this limitation, a crosslinker [3] is added to stabilize the material, providing both thermal and mechanical stability.
Here, we report on the free-radical copolymerization of elemental sulfur with divinylbenzene (DVB). The resulting sulfur-based polymers were characterized to evaluate their potential as alternatives to conventional IR materials.

2. Synthesis of optical windows
Optical windows were synthesized using the inverse vulcanization process, in which the resulting material is primarily composed of sulfur forming the polymer backbone, interconnected by organic linkers.
Sulfur (S_8) and divinylbenzene (DVB) stabilised with 4 tert-butylpyrocatechol were purchased from Sigma-Aldrich and used as received, without further purification.
The synthesis procedure is as follows: elemental sulfur is placed in a sealed vessel equipped with a septum and a balloon to prevent overpressure, and heated in an oil bath preheated at 140 °C. Once the sulfur is completely molten, divinylbenzene (DVB) is added via a syringe. The reaction mixture is stirred until it

DOI: https://doi.org/10.26799/cp-polymers-composites-3Bsmaterials-2025
becomes homogeneous and forms a single transparent phase. The magnetic stir bar is positioned above the liquid surface, remaining inside the vial. The reaction time has been set to six hours.
Four compositions were developed: Sample A (70 wt% S), Sample B (60 wt% S), and Samples C and D (50 wt% S). Figure 1 shows the synthesized sulfur–divinylbenzene (S-DVB) polymers and the thicknesses of samples B, C, and D after having been removed from the mold and manually polished. Sample A was damaged when removed from the glass vial, as it stuck to the glass during the process. It is possible that the DVB content was too low to sufficiently stabilize the polymer network in this case (Figure 1).

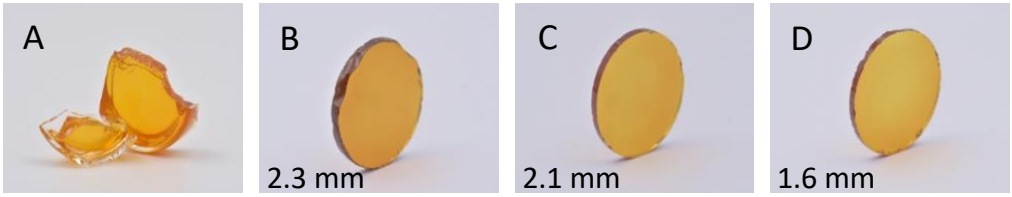

Figure 1: Polymers of Sulfur and DVB – with different ratios

3. Characterization of polymers (S-DVB)

3.1. Differential Scanning Calorimetry (DSC)

Differential Scanning Calorimetry (TA Instruments Discovery Q2500) was carried out under N_2 flow with hermetic Tzero aluminium crucibles. The measure was performed from -30 °C to 150 °C with a heating rate of 5 °C/min. Two identical cycles are done during the analysis and only the second cycle is shown on this report, Figure 2. Glass transition temperatures (Tg) are given on the legend of the Figure 2 and show an increasing trend as the amount of DVB increases. In fact, the network becomes more rigid through cross-linking, which is due to the aromatic rings in the DVB structure. Sample A (S-DVB 70/30) exhibits an additional thermal event around 135 °C, likely due to the melting or the allotrope transition of residual unreacted sulfur, suggesting an incomplete network formation at low DVB content, which could explain why it broke during demoulding. The Tg values for the 60/40 and 50/50 ratios are close. This may indicate a plateau in the thermal stability of the samples. Further tests with higher concentrations of DVB should be carried out.

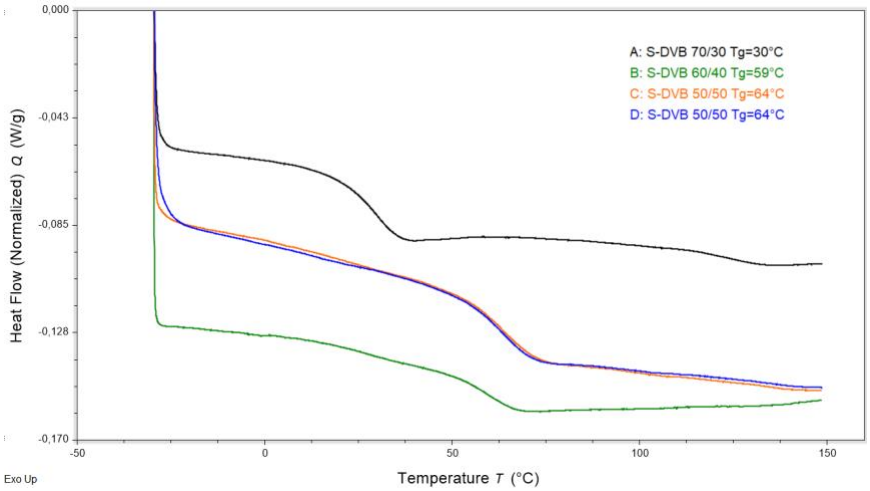

Figure 2: DSC curves of S-DVB polymers with varying weight ratios

3.2. Fourier Transform Infra-Red spectroscopy (FTIR)

A Perkin Elmer Fourier Transform Infrared Spectrometer (FTIR) was used to collect infrared spectra from 2 µm to 5 µm. The figure 3 shows the normalized FT-IR transmittance spectra for three optical filters of

DOI: https://doi.org/10.26799/cp-polymers-composites-3Bsmaterials-2025
(S-DVB) polymers compared with an uncoated germanium (Ge) reference. The normalization process eliminates the influence of the sample thickness, allowing for a direct comparison of the optical properties. All S-DVB samples exhibit a broad transmission window with several specific absorption bands attributed to sulfur-based vibrations and DVB-derived functionalities. They show similar spectral features, indicating a consistent chemical composition and a satisfaying network formation across these formulations. Unlike the S-S bonds of sulfur, which provide transparency in the mid-infrared region, the C-H or heteroatom-hydrogen bonds of DVB are responsible for the absorption in this spectral zone. A compromise must be found between the sulfur content and the DVB.
There is a slight variation in transmittance levels for these three samples, with a slightly higher transmittance for sample B compare to the others. These transmittances are interesting for our study and show that these samples can be used for mid-infrared applications, but they are still lower than the reference example, undoped Ge, which has a stable transmittance between 2 and 5 µm of around 85 %.

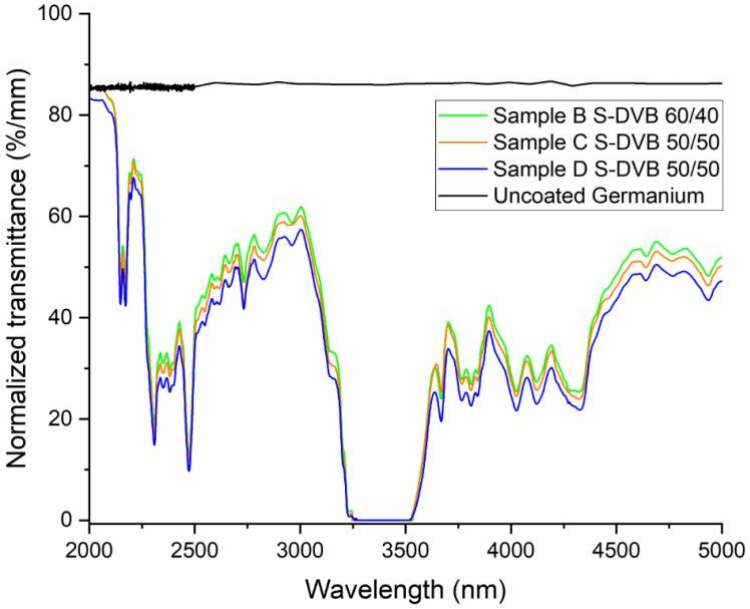

Figure 3: Normalized FT-IR transmission spectra of S-DVB polymers with different DVB contents (S-DVB 60/40, 50/50) compared to an uncoated germanium substrate

Even though the thickness was not accounted for in this characterization, it plays a significant role and should be considered. Since transmittance is closely linked to the thickness, it is essential to minimize the thickness while preserving the characteristics of a bulk sample. These initial filters have a thickness between 1.6 and 2.3 mm, but the aim will be to have a standard thickness around 1 mm, which is sufficient to carry on some infrared optical imaging tests.

3.3. IR optical imaging test

Complementary to their spectrophotometric characterizations, we attempted to assess the imaging performance of the optical filters on a dedicated optical setup shown on the figure 4. We use an IR imager (FLIR A6750) having its highest sensitivity in the spectral range 1 – 5 µm pointing towards a blackbody source whose temperature is set at 393 K, allowing some IR radiations in the appropriate spectral range. To obtain the optimal field of view, one needs to place the sample at an intermediate focal point. Accordingly, the cameras' imaging lens was replaced with a series of CaF_2 lenses (details on figure 4). CaF_2 lenses have been selected due to their optimal transmittances in the mid-IR region. Actually, the series of lenses has been calculated to perfectly image the blackbody in the plane of the cameras' sensor.

DOI: https://doi.org/10.26799/cp-polymers-composites-3Bsmaterials-2025

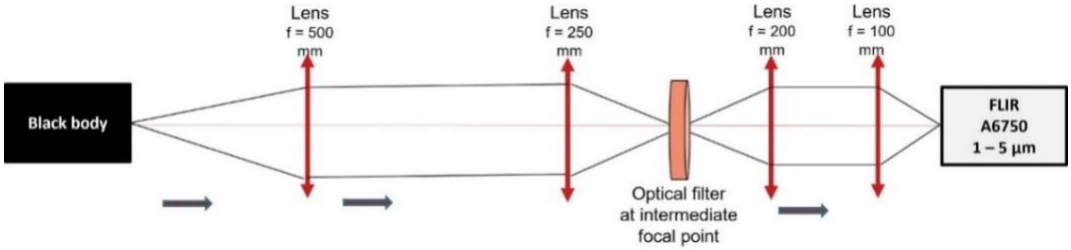

Figure 4: Optical setup for IR imaging experiments. To maximize the field of view, the sample is placed at the intermediate focal point of the optical system

Using this methodology, the images shown in figure 5 were obtained. For each optical filter B, C or D a comparison was made with the reference, i.e., without any optical filter on the optical bench. Two types of information can be extracted from these results. The first is the transmittance: a visual comparison can be made between the reference and the image obtained by the IR camera. The transmittance for the three samples B, C and D is fairly low. The second piece of information is the measurement of the structural similarity index (SSIM). This calculation determines whether there is a disturbance in the wavefront caused by the sample. A value of 1 indicates that the structure of the images is identical, so the sample is homogeneous and there is no wavefront disturbance. In the opposite case, when the structure of the images does not correspond at all, the value is 0. The SSIMs for the three samples are relatively close to 1, particularly for B. These filters do not induce too many wavefront disturbances.

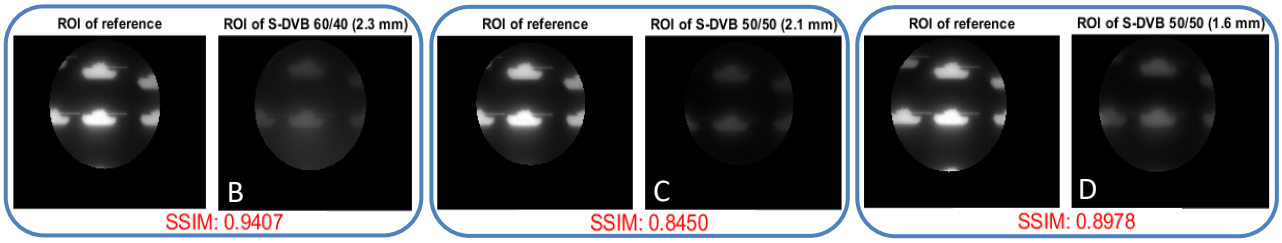

Figure 5: Obtained images with the IR optical imaging test: reference (no filter) compared to filters B, C and D respectively

4. Conclusion

In this study, sulfur-based polymers synthesised by inverse vulcanization with divinylbenzene were successfully transformed into optical windows. FTIR spectroscopy confirmed the existence of a transmission window in the 2 to 5 µm range, suitable for mid-infrared applications, although the transmittance is lower than that of traditional materials such as germanium. Imaging tests using an IR camera revealed that these materials exhibit a low but constant transmittance and a minimal wavefront distortion, as confirmed by SSIM values close to 1. These initial results are interesting but require further investigation of other properties (refractive index, SDT, FT-IR ATR mode etc.) to confirm whether S-DVB polymers have some potential as cost-effective alternatives to IR materials.

References

1. P. Sangwoo, L. Duhwan, C. Hongkwan, “Inverse Vulcanization Polymers with Enhanced Thermal Properties via Divinylbenzene Homopolymerization-Assisted Cross-Linking”, *ACS Macro Lett*, 8, 1670-1675, 2019.
2. S. Namnabat, J.J. Gabriel., “Optical properties of sulfur copolymers for infrared applications”, *Proceedings of SPIE Defense & Security*, Vol. 8983, 89830D-1, 2015.
3. X. Wu, J.A. Smith “Catalytic inverse vulcanization”, *Nature Communications*, 10:647, 2019.

Proceedings of the Polymers, Composites, 3BsMaterials 2025 Joint International Conferences
AlBufeira, Portugal – April 16 – 18, 2025
DOI: https://doi.org/10.26799/cp-polymers-composites-3Bsmaterials-2025

Modeling the Drying Kinetics of Polymer Volatile Systems Using Thermogravimetric Analysis Data

E. G. Viehböck[1,2,*], T. Ehrmann [2], G. R. Berger-Weber[2],
A. Hammer[2], M. Kirchmayr[3],C. Paulik[1,4]
[1] Competence Center CHASE GmbH, Linz, Austria
[2] Institute of Polymer Processing and Digital Transformation, Johannes Kepler University Linz, Linz, Austria
[3]EREMA Engineering Recycling Maschinen und Anlagen Ges.m.b.H., Ansfelden, Austria
[4] Institute of Chemical Technology of Organic Materials, Johannes Kepler University Linz, Linz, Austria

Abstract

Thermogravimetric analysis (TGA) is a well-established technique for investigating the drying kinetics of moist polymers by monitoring mass loss under controlled temperature conditions. In this study, lumped parameter models originally developed for food drying, such as the modified Page and Verma models, were applied to polymer drying processes with good agreement. These empirical models are capable of capturing drying procedures with Fickian as well as with anomalous non-Fickian diffusion behavior, observed at different temperature regimes. We used a model system based on polyamide 6 (PA6) with water as its volatile component. Its drying kinetics were characterized experimentally and served as the foundation for developing and validating predictive drying models. The temperature dependence of the drying process was effectively captured through Arrhenius-type behavior and fitted using nonlinear regression techniques, enabling the development of predictive models with adjusted R^2 values consistently exceeding 0.99. Such models allow to interpolate the drying behavior across various process conditions and to optimize the drying procedures for mitigating polymer degradation while drying to the desired moisture content. Furthermore, the predictive capability of these models paves the way for designing industrial drying processes with reduced need on extensive experiments. In conclusion, looking at the similarities in moisture transport mechanisms between food and polymer systems offers a robust framework for understanding and controlling volatile removal in polymer processing.

Keywords: thermogravimetrical analysis, polymer drying, drying kinetics, modeling, sorption, desorption, volatile removal, polymer processing

1. Introduction

Efficient moisture removal from hygroscopic polymers is essential for stable melt processing and high product quality. Polyamide 6 (PA6) readily absorbs ambient water, which—if not fully removed—can cause hydrolytic degradation, foaming, and ultimately reduced product performance. Conventional drying protocols based on fixed hold-times are often energy-intensive and poorly adaptable to different grades or processing conditions.

Isothermal thermogravimetric analysis (TGA) combined with kinetic modeling offers a predictive alternative. By characterizing drying behavior under controlled thermal conditions, optimized drying schedules can be derived. Among various modeling approaches, the Verma model—with parameters adapted for temperature dependence—offers a balance between physical interpretability and computational efficiency [1].

In this study, PA6 specimens with uniform water content were dried isothermally at various temperatures. After data processing, the Verma model was fitted to each drying curve and generalized across the temperature range using simple temperature-dependent functions. This framework enables accurate prediction of moisture content as a function of time and temperature, offering a scalable tool for energy-efficient industrial PA6 drying.

2. Experimental Methodology

2.1 Sample Preparation

Polyamide 6 (PA6) granules (Ultramid B3S, BASF) were first vacuum-dried at 80 °C for 4 hours to ensure a residual moisture content below 0.1 wt-%. Disc-shaped specimens were then produced by a hot press at 230 °C, applying a load of 10 metric tons for 2 minutes. The resulting specimens had a diameter of 2.2 mm and a thickness of 1.21 mm.

DOI: https://doi.org/10.26799/cp-polymers-composites-3Bsmaterials-2025

Subsequent water uptake was induced by immersing the specimens in distilled water at 23 ± 1 °C until an equilibrium state was reached, which was confirmed through periodic gravimetric measurements using an analytical balance. Fickian diffusion behavior was verified using the halftime method, indicating an average saturation time of approximately 15 hours at room temperature [2]. To ensure consistent saturation, all specimens were immersed for a longer duration. The final equilibrium moisture content was determined to be 10.21 ± 0.14 wt% (n = 15). This relatively high uptake is attributed to the reduced crystallinity of the hot-pressed samples (28.7%) compared to the raw granules (45.7%), as determined by differential scanning calorimetry (DSC). The lower crystallinity increases the amorphous fraction, thereby facilitating water uptake [3].

2.2 Isothermal TGA Measurements

Isothermal drying experiments were conducted using a PerkinElmer EGA 4000 top-loading thermobalance (Waltham, MA, USA), which allows for high-resolution mass change measurements under controlled temperature conditions. Each saturated specimen was placed into the microbalance pan at ambient temperature. The system was then heated at a controlled ramp rate of 20 K/min to the target isothermal temperature. The drying process was monitored until the mass loss plateaued, indicating that an equilibrium had been reached.

2.3 Data Processing

2.3.1 Determination of the equilibrium mass m_{eq}

A top-loading microbalance was used in this study, which reduces typical systematic errors associated with other TGA configurations, such as those caused by sample movement or furnace design. Nevertheless, blank measurements were performed to further eliminate measurement artifacts, particularly during the heating phase. Since TGA requires the specimen to be introduced at room temperature followed by a ramp-up to the target isothermal level (20 K/min in this case), buoyancy effects and changes in gas density can artificially increase the measured mass during this transition. To correct for these effects, blank measurements were subtracted from the sample measurements during the ramping phase.

2.3.2 Normalization of the drying curves

To facilitate comparison between drying curves at different temperatures, normalization was applied using the concept of the moisture ratio (MR), which is commonly found in the literature [4, 5, 6]. The MR is defined as:

$$MR(t) = \frac{m(t) - m_{eq}}{m_0 - m_{eq}}, \tag{1}$$

where $m(t)$ is the mass at a given time t, m_0 is the initial saturated mass, and m_{eq} is the final equilibrium mass after complete drying. This dimensionless ratio enables the drying kinetics to be compared independently of absolute water content.

3. Model Development

To capture the isothermal drying kinetics of PA6, we adopted a food drying model proposed by Verma et al.[1]. This form distinguishes a fast and a slow moisture-removal mechanism and defines the moisture ratio $MR(t)$ as follows:

$$MR(t) = A\exp(-k_0 t) + (1 - A)\exp(-k_1 t). \tag{2}$$

Here A $(0 < A < 1)$ serves as a weighting factor that balances the contributions of the two drying phases, distinguishing between the faster and slower moisture removal mechanisms. The parameters k_0 and k_1 represent the corresponding drying rate constants for each phase.

DOI: https://doi.org/10.26799/cp-polymers-composites-3Bsmaterials-2025

Since the objective is to develop a predictive model applicable across a wide temperature range, each parameter of the Verma model was treated as temperature dependent. For this purpose, individual isothermal experiments were conducted at discrete temperature levels, and the corresponding model parameters were independently fitted for each temperature. The resulting temperature-dependent parameter values were then plotted as a function of temperature. To enable interpolation and prediction across the entire temperature range, each parameter was subsequently modelled as a continuous function of temperature using the following expressions:

$$A(T) = s_A T - d_A;$$
$$k_i(T) = \exp(s_i T - d_i) \ (i = 0,1). \tag{3}$$

The parameter $A(T)$ is described as a linear function of temperature, where s_A denotes the slope and d_A the offset, capturing how the weighting between the two drying mechanisms changes with temperature. The drying rate constants k_i are modeled as exponential functions of temperature, with s_i and d_i for $(i = 0,1)$ representing the slope and offset in the logarithmic domain, respectively.

4. Results and Discussion

The Verma model, as adapted in this study, was evaluated across a broad temperature range (50 °C to 120 °C) using isothermal thermogravimetric analysis (TGA) data. For each isothermal measurement, the normalized moisture ratio (MR) was computed and fitted with the two-term exponential Verma model. This allowed the extraction of three key parameters: the weighting factor A and the drying rate constants k_0 and k_1.

Initially, these parameters were independently fitted at each temperature. The resulting temperature dependence of each parameter was then modeled using simple empirical functions. This parameterization enables a continuous prediction of the drying behavior across the investigated temperature range.

A comparison between the model predictions and the experimental drying curves at each isothermal level is illustrated in Figure 1, demonstrating the capability of the model to reproduce the characteristic drying behaviour.

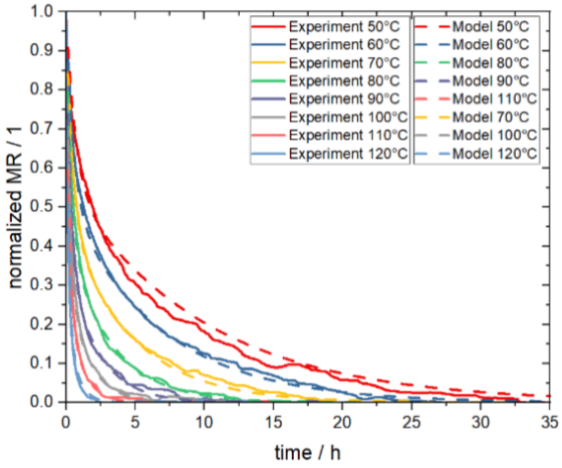

Fig. 1: Comparison between experimentally measured drying data and Verma modelled data.

The corresponding temperature dependence of the fitted parameters is summarized in Figure 2, highlighting the systematic trends used to generalize the model across temperatures.

DOI: https://doi.org/10.26799/cp-polymers-composites-3Bsmaterials-2025

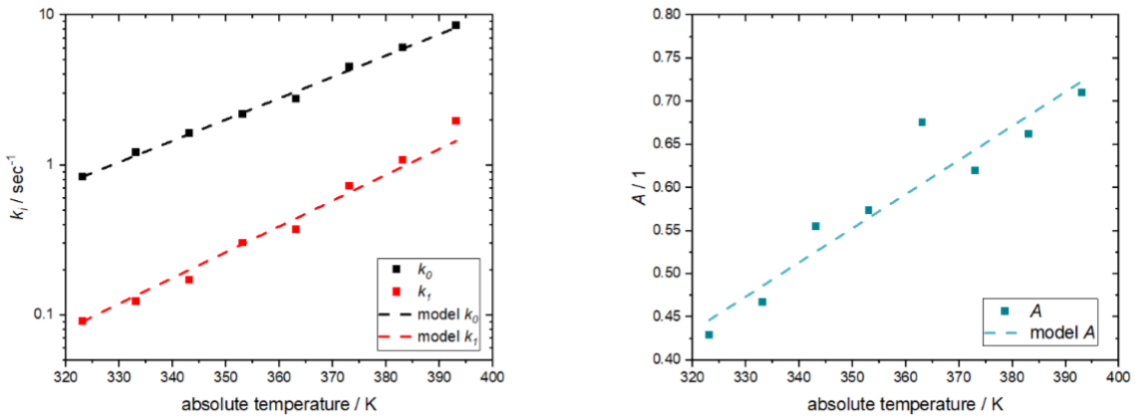

Fig. 2: Temperature-dependent drying kinetics parameters: drying rate constants k_0 and k_1 (left) and weighting factor A (right).

The quality of the model fit was assessed using the coefficient of determination R^2. Across all temperature levels, the model achieved R^2 values greater than 0.99, indicating excellent agreement between the predicted and experimental drying curves. These results confirm that the Verma model, when extended with temperature-dependent parameters, provides a robust framework for capturing the drying kinetics of PA6 under isothermal conditions.

5. Conclusion and Outlook

By describing the drying behavior with only six global parameters, this approach offers a practical and scalable method for predictive modeling in industrial drying simulations. Further work may extend the approach to non-isothermal or multi-stage drying processes or may be extended to account for the influence of varying crystallinity levels, as literature suggests that volatile absorption predominantly occurs in the amorphous regions of semicrystalline polymers.

Acknowledgements

The authors acknowledge support through the FTI initiative circular economy “circPLAST-mr”, funded by the BMK (federal ministry for climate, environment, energy and innovation) and the FFG (Austrian Research Promotion Agency)—funding number 889843.

References

[1] Lalit R. Verma, R. A. Bucklin, J. B. Endan, and F. T. Wratten, “Effects of Drying Air Parameters on Rice Drying Models,” *Transactions of the ASAE*, vol. 28, no. 1, pp. 296–301, 1985, doi: 10.13031/2013.32245.

[2] V. Kanellopoulos, M. A. Ali, S. Sundvall, and S. Das, “Experimental and Theoretical Study on the Desorption of Alcohols and Ketones from Polyolefins,” *Ind. Eng. Chem. Res.*, vol. 52, no. 45, pp. 15855–15862, Nov. 2013, doi: 10.1021/ie402479e.

[3] V. Miri, O. Persyn, J.-M. Lefebvre, and R. Seguela, “Effect of water absorption on the plastic deformation behavior of nylon 6,” *European Polymer Journal*, vol. 45, no. 3, pp. 757–762, Mar. 2009, doi: 10.1016/j.eurpolymj.2008.12.008.

[4] S.-H. Kim, F. Tanaka, and F. Tanaka, “Drying kinetics and determination of effective moisture diffusivity and activation energy in cucumber pericarp tissues using thin-layer drying models,” *FSTR*, vol. 27, no. 2, pp. 181–192, 2021, doi: 10.3136/fstr.27.181.

[5] R. Hasibuan, W. N. Sari, R. Manurung, and V. Alexande, “Drying Kinetic Models of Rice Applying Fluidized Bed Dryer,” *MMEP*, vol. 10, no. 1, pp. 334–339, Feb. 2023, doi: 10.18280/mmep.100138.

[6] Z. Erbay and F. Icier, “A Review of Thin Layer Drying of Foods: Theory, Modeling, and Experimental Results,” *Critical Reviews in Food Science and Nutrition*, vol. 50, no. 5, pp. 441–464, May 2010, doi: 10.1080/10408390802437063.

Proceedings of the Polymers, Composites, 3BsMaterials 2025 Joint International Conferences
AlBufeira, Portugal – April 16 – 18, 2025
DOI: https://doi.org/10.26799/cp-polymers-composites-3Bsmaterials-2025

Improving Process Stability in Mechanical Recycling of Thermoplastic Composites with a Lab-Scale Dosing System

Tina Mayrhofer[1], János Birtha[2], Christian Marschik[2], Gerald Roman Berger-Weber[3], Klaus Straka[1]
[1]JKU, LIT-Factory, Linz, Austria,
[2]Competence Center CHASE GmbH, Linz, Austria,
[3]JKU, Institute of Polymer Processing and Digital Transformation, Linz, Austria

Abstract
Thermoplastic composites (TC) offer significant advantages over thermoset composites, particularly in their ability to be remelted multiple times, which enables thermoplastic composites to be mechanically recycled, thereby promising a more sustainable solution for lightweight design with endless-fibre reinforcement. The mechanical recycling process involves three key stages: pretreatment, in which the TC-parts are cut to flakes; regranulation, in which these flakes are pelletized into recyclates; and remanufacturing, in which the recycled pellets are reprocessed into new (short) fibre-reinforced TC-parts.
During regranulation, flakes of different size and shape are fed into the (twin-screw) extruder for either the dilution of fibre content or the adjustment of material properties by using additives. However, inconsistent bulk density of the flakes within the screw intake zone may induce variations in the fibre mass content of the final pellets, in particular, if the used gravimetric flake dosing system itself conveys differently depending on flake size. To test and improve process stability, we developed a lab-scale dosing test system that measures flake size distribution and transient output weight. This system comprises four main components: i) the gravimetric dosing unit that transports the flakes onto a conveyor belt, ii) a line scan camera that measures the size and shape of the flakes, iii) the conveyor belt, and iv) a differential scale placed at the end of the conveyor belt that records the weight of the flakes.
This setup was tested using shredded thermoplastic composite flakes, both unfiltered and size-filtered, to verify both the accuracy and the reproducibility of the dosing unit. First experiments validated our hypothesis, demonstrating a strong correlation between flake size and the measured throughput rate of the dosing system. Finally, our results may allow a feedback loop system that can adjust the flake feed rate to the extruder in real time, leading to a better process consistency.

Keywords: Thermoplastic composites, Mechanical recycling, Flake size distribution, Gravimetric dosing system

1. Introduction
The demand for lightweight and sustainable materials has intensified research into thermoplastic composites (TCs) as viable alternatives to traditional thermoset composites. Unlike thermoset materials, which undergo irreversible curing, TCs possess the unique capability to be remelted and reprocessed multiple times, facilitating their mechanical recycling and promoting sustainability in line with circular economy principles [1, 2].
The mechanical recycling of TCs encompasses three primary stages: pretreatment, regranulation, and remanufacturing. Initially, during pretreatment, end-of-life or scrap TC components are shredded into flakes of varying sizes. Subsequently, in the regranulation phase, these flakes are molten, blended with virgin material and pelletized into recyclates, allowing for adjustments in fiber content through dilution or the incorporation of reinforcement materials. Finally, the remanufacturing stage reprocesses the recycled pellets into new fiber-reinforced TC components, thereby preserving their structural integrity [3, 4].
While mechanical recycling offers a promising pathway toward sustainable composite production, maintaining process stability and consistency during regranulation remains a significant challenge. Variations in flake size and bulk density can affect dosing efficiency in extrusion processes, leading to fluctuations in fiber mass content within the final recyclates. Addressing these challenges requires precise monitoring and control of material flow [5].

DOI: https://doi.org/10.26799/cp-polymers-composites-3Bsmaterials-2025

To confront these issues, this study introduces a lab-scale dosing test system designed to assess and enhance process stability in the mechanical recycling of TCs. By analyzing flake size distribution and transient throughput weight, this system aims to develop a feedback mechanism that ensures consistent feed rates during extrusion, ultimately improving the quality and reliability of recycled TC materials.

2. Material and Methods

To evaluate the stability and accuracy of the flake dosing process, a lab-scale dosing test system was developed. This system was designed to measure flake size distribution and transient throughput weight, enabling for analyzing the material flow consistency. Figure 1 illustrates the four key components of the experimental setup. (1) a gravimetric dosing unit that continuously transported TC flakes onto a conveyor belt, (2) a line scan camera positioned above the belt to acquire high-resolution images for size and shape analysis, (3) the conveyor belt itself, which ensured controlled and uniform transport of the flakes, and (4) a differential scale placed at the end of the conveyor belt to record the accumulated weight of the flakes over time. Experiments were conducted using unfiltered shredded TC flakes to assess the precision and stability of the dosing unit. The dosing scale was equipped with a helical screw conveyor and an agitator to ensure continuous material flow by preventing bridging phenomena. The line scan camera data was processed to determine flake size distribution, while the differential scale provided continuous measurement of the flake output. By correlating the flake size distribution with the measured throughput rate, the system allowed for a detailed evaluation of the effects of flake geometry and filling level of the dosing scale on dosing fluctuations.

Each DoE set corresponds to a predefined filling level of the dosing hopper. The dosing ran until the next filling level, however, only the first 60 seconds were analysed. The number of dosed and measured flakes grew with the throughput rate (Table 1), representing the total material in the hopper better well. To cross-check the dosing, the throughput of the dosing scale (item 1 in Fig. 1) was validated by the reference scale (item 4 in Fig. 1), confirming that the observed trends in flake size distribution and weighted average particle size were directly related to the dosing rate.

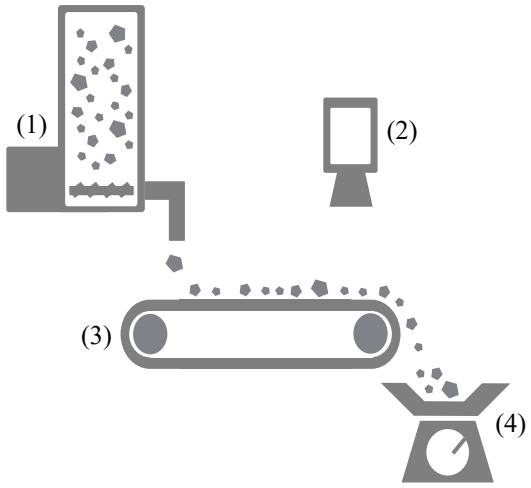

Figure 1: Schematic representation of the experimental setup. (1) gravimetric dosing scale, (2) line scan camera, (3) conveyor belt, (4) differential scale.

3. Results

The altering throughput rate of 3 kg/h, 5 kg/h, and 7 kg/h affect the polydispersity index (PDI) and the weighted mean particle size. The PDI is used to describe the width of the particle size distribution and is defined as the ratio of the weight-average to the number-average. Lower values indicate a more uniform distribution, while higher values reflect greater heterogeneity. As shown in Figure 2, at 7 kg/h throughput, for filling levels from 30 % to 80 %, the PDI is stable within the range of 80 to 100. Bellow the filling level of 30 %, the PDI grows considerably,

DOI: https://doi.org/10.26799/cp-polymers-composites-3Bsmaterials-2025

which is indicative of a broader particle size distribution. This increase in PDI is consistent with the behavior observed at the lower throughput rates, where persistent electrostatic adhesion of small particles to the conveyor belt accumulates to a growing PDI, in other words, small particles were again optically detected in subsequent DoE sets. Nevertheless, small particles should show only minimal impact on the weighted mean particle size. The results from all throughput rates suggest that while particle adhesion and repeated measurements affect the PDI, the weighted mean remains relatively stable, with only minor increases as the dosing scale empties.

Table 1 presents the characteristics of flake size distribution and associated parameters, providing detailed insights into the relationship between flake size, PDI, number of flakes, and sample size under varying experimental conditions. The table highlights the variations in PDI, reflecting the spread of particle sizes across different sample sets, and shows how the number of flakes correlates with the measured size distribution. Additionally, the sample size data provides context for the scale of measurement and the representativeness of each dataset. Since the measurement time was identical across all throughput settings, a greater number of flakes were recorded at the 7 kg/h setting, thereby enhancing the statistical reliability of the results.

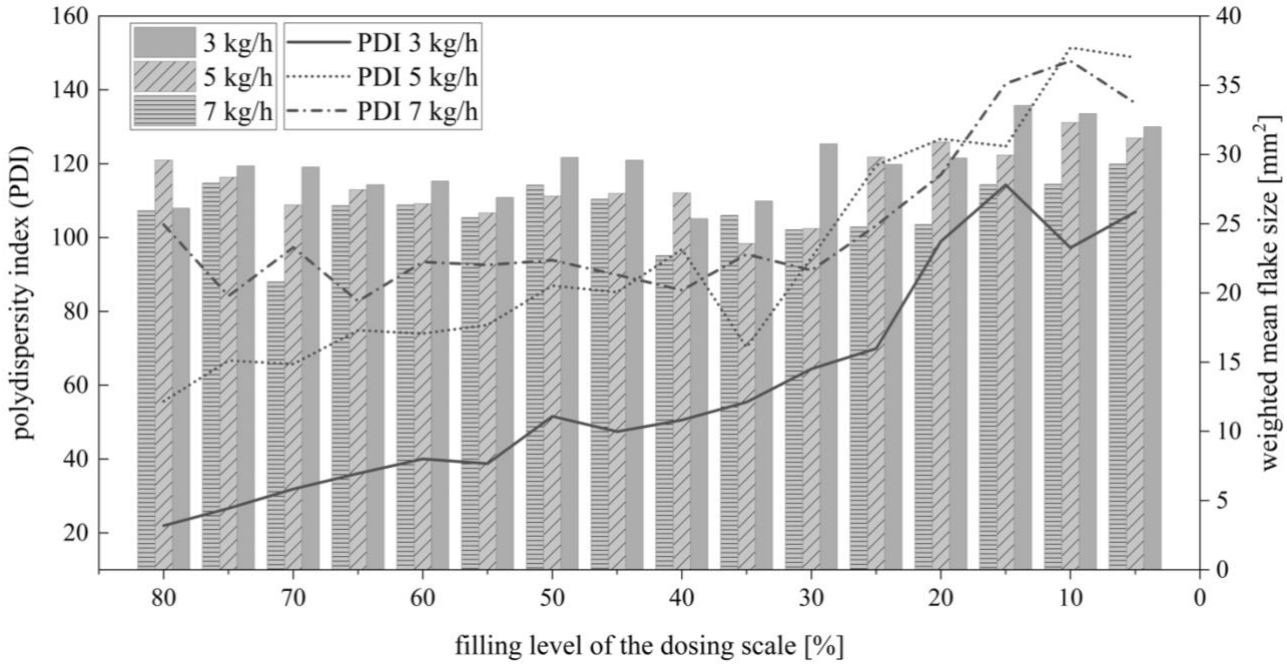

Figure 2: Comparison of the weighted mean flake size (right) and the polydispersity index (PDI) (left) at different throughput rates of the dosing scale. The relative error of the weighted mean is 1.95% at 3 kg/h, 2.12% at 5 kg/h, and 1.99% at 7 kg/h.

Table 1: Characteristics of flake size distribution and associated parameters.

	3 kg/h	**5 kg/h**	**7 kg/h**
Flake size weighted mean [mm^2]	29.177	27.984	25.930
PDI	59.5	94.9	103.5
Number of measured flakes	348,145	1,015,173	1,863,459
Sample size: [%] of the total emptying time	19	32	45

4. Discussion

The results from the throughput rates of 3 kg/h, 5 kg/h, and 7 kg/h on the dosing scale reveal key insights into the dynamics of particle measurement, particularly concerning PDI, weighted mean particle size, and the impact of particle adhesion during the dosing process. While trends in particle behavior remain consistent across the different

DOI: https://doi.org/10.26799/cp-polymers-composites-3Bsmaterials-2025

throughput rates, variations in PDI and the weighted mean particle size highlight the importance of both the dosing rate and the disturbing particle interaction with the conveyor belt.

PDI increases at nearly all throughput rates as particle count rises and the dosing scale empties. However, as only PDI increases and weighted mean does not increase, the height of the particle column in the dosing hopper does not affect the bulk density and the dosing performance, in other words, the gravimetric dosing works well. In fact, the PDI growth is presumably caused by the repeated measurement of smaller particles, that tend to adhere to the conveyor belt instead of being ejected to the differential scale. Sticking behavior was observed by the human operators and particularly evident at 5 kg/h and 3 kg/h, where a noticeable rise in detected flakes suggests that particle adhesion becomes more significant with increased throughput. However, at a throughput rate of 7 kg/h, this effect is delayed, with the PDI only increasing after approximately ten measurement iterations, which correspond to the filling level decreasing from 80% to 30%, suggesting that the adhesion of smaller particles accumulates over time and gradually influences the measurements.

Although small particles raise the PDI, their impact on the weighted mean should be negligible. The measured slight increase in weighted average flake size when emptying the dosing hopper may result from stirrer-induced segregation, causing larger flakes to migrate upward.

The results from the 7 kg/h throughput rate offer insights into the behavior of the dosing system at higher throughput rates. At 7 kg/h, the PDI remained relatively stable at higher filling levels of the dosing scale (80%–30%). However, when the filling level dropped below 30%, a more significant increase in PDI was observed. As with the other throughput rates, this increase in PDI does not significantly affect the weighted mean particle size, further confirming the robustness of the weighted mean as an indicator of particle size under varying throughput conditions. The findings suggest that the PDI is more sensitive to variations in particle behavior and the dynamics of the dosing scale. The slight increase in the weighted mean as the dosing scale empties further supports the notion that the contribution of smaller particles diminishes over time.

5. Conclusion

In summary, the findings of this study emphasize the significant influence of flake size on dosing stability and throughput rate. The lab-scale dosing test system proved to be reproducible and providing reliable measurements across varying throughput conditions. A clear negative correlation was found between mean flake size and throughput rate. These results highlight the potential for improved control over the regranulation process, offering opportunities for the integration of real-time feedback to optimize dosing operations. Additionally, this approach could contribute to more consistent fiber mass content in recycled thermoplastic composites, supporting the development of sustainable and efficient manufacturing practices in the recycling industry.

Acknowledgements

The authors acknowledge financial support by the COMET Centre CHASE, which is funded within the framework of COMET—Competence Centers for Excellent Technologies—by BMVIT, BMDW, and the Federal Provinces of Upper Austria and Vienna. We also acknowledge the support of the Institute of Polymer Processing and Digital Transformation and the LIT-Factory for providing the necessary facilities and resources for conducting the experiments. Finally, we acknowledge the constructive feedback from our colleagues, which played a significant role in refining the quality of this work.

References

[1] A. Lamtai, S. Elkoun, M. Robert, F. Mighri, C. Diez, "Mechanical Recycling of Thermoplastics: A Review of Key Issues," Materials Science, vol. 1, no. 4, pp. 50, 2025.

[2] R. Bernatas, S. Dagreou, A. Despax-Ferreres, A. Barasinski, “Recycling of fiber reinforced composites with a focus on thermoplastic composites,” *Cleaner Engineering and Technology*, vol. 5, p. 100272, 2021.

[3] E. Moritzer, G. Heiderich, "Mechanical Recycling of Continuous Fiber-Reinforced Thermoplastic Sheets," AIP Conference Proceedings, vol. 1713, no. 1, pp. 120013, 2024.

[4] A. Pegoretti, "Towards sustainable structural composites: A review on the recycling of continuous-fiber-reinforced thermoplastics," *Adv. Ind. Eng. Polym. Res.*, vol. 4, no. 2, pp. 105–115, 2021.

[5] Y. S. Türker, F. Öztürk, Y. Öz, "Review of Recycling Methods of Thermoplastic Composite Materials," Journal of Composite Materials, vol. 58, no. 2, pp. 1-15, 2024.

Proceedings of the Polymers, Composites, 3BsMaterials 2025 Joint International Conferences
AlBufeira, Portugal – April 16 – 18, 2025
DOI: https://doi.org/10.26799/cp-polymers-composites-3Bsmaterials-2025

Modification of the Tadmor Model for Improved Melting Simulation of Polyamide 6 in Injection Molding

S. Schaufler[1,2]*, Dominik Altmann[2], U. Stritzinger[2], G. Berger-Weber[2]
[1]Kompetenzzentrum Holz GmbH, Altenberger Straße 69, 4040 Linz, Austria
[2]Institute of Polymer Processing and Digital Transformation, Johannes Kepler University Linz, Altenberger Straße 69, 4040 Linz, Austria

Abstract
Accurate simulation of the plasticizing process in injection moulding is essential for a comprehensive understanding of the process and the development of optimized procedures. Modelling the melting mechanism plays a crucial role in improving the accuracy of plasticizing simulations. Originally developed for single-screw extrusion, the Tadmor model is considered as state-of-the-art for modelling the polymer melting process. However, we observed in screw pull-out tests, that the Tadmor model – the Tadmor model assumes a rectangular melt pool – does not accurately reflect the melting behaviour of polyamide 6 (PA6), which showed a more quadratic melt pool.
Thus, we adapted the Tadmor melting model and benchmarked it with the classical Tadmor model both in analytical simulations and experimental validation using PA6, varying back pressure, circumferential screw velocity, and metering stroke. The melting profile was recorded using ultrasonic sensors, mounted directly on the barrel.
The modified Tadmor model (quadratic melt pool) predicts the actual melting behaviour more accurately, in particular, at small metering strokes.
Keywords: polymer processing, modelling, melting, injection moulding, simulation

1 INTRODUCTION

Melting in polymer processing plays a critical role in determining the final products quality. To ensure proper homogenization and avoid voids in the injection moulding parts, sufficient polymer melting along the screw during the plastification step is required. The mechanism of melting differs between extrusion and injection moulding due to the axial screw movement of the latter. Melting behaviour is strongly affected by the material properties, processing parameters, and screw geometry. Various melting models and simulation tools try to predict the melting behaviour in advance. Unfortunately, the melting mechanism differs within materials. For polyamides accounting for approximately USD 41.0 billion of global market share in 2024 –and projected USD of 59.27 billion by 2030– the importance of accurately modelling their melting behaviour is substantial but still not solved. [1].
One of the most well-known melting models is the Tadmor model [2], which was further developed by Tadmor and Klein [3], and later Tadmor and Gogos [4]. According to this model, melting begins with a melt film formation at the inner barrel surface. The temperature of the melt film can be calculated using the method by Aigner et al. [5]. As the melt film grows, the wall adherence effect causes a drag flow which carts off the melt film and accumulates the melt in a rectangular melt vortex in front of the active screw flight. **Error! Reference source not found.** a) depicts this effect. This vortex grows down the screw channel.
In previous screw pull-out tests, an unexpected melting behavior of PA6 was detected: The melt pool was formed in a quadratic and not rectangular shape with a persistent underneath granulate layer at the channel ground. **Error! Reference source not found.** b) to e) show the formation of a rectangular meltpool according to Tadmor and the observed meltpool growth in PA6 with examples of the phenomena for HDPE and PA6.
Based on the melting model by Tadmor and Gogos, we modified the volume flow rate calculation by assuming a quadratic melt pool instead of the rectangular one originally described. The suitability of both models was evaluated by comparing the simulated melting behaviour to experimental data obtained using ultrasonic sensors along the extruder barrel. The simulations were performed using the Screw Simulation Software (S3) developed at the Johannes Kepler University Linz (JKU).

DOI: https://doi.org/10.26799/cp-polymers-composites-3Bsmaterials-2025

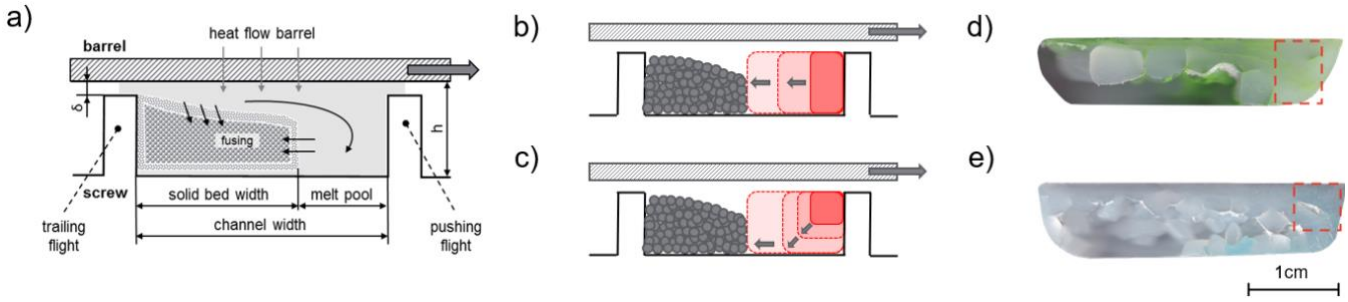

Figure 1: Depiction of the Tadmor melting model including the heat flow and material transport phenomena a) [6]. Development of the melting pool for the classical Tadmor model b). Development of the melting pool in the modified Tadmor melting model c). Cross-sections in the feeding zone after 6D of screw length for PE-HD d) and PA6 e).

2 SIMULATION AND MELTING MODELS

Simulations were conducted with the S3 simulation tool. The material investigated was a PA6 B30S from Lanxess (Köln, Germany). Three different process settings were simulated:

a) Setting 1: Screw velocity of 0.3 m/s, back pressure of 150 bar and metering stroke of 28 mm
b) Setting 2: Screw velocity of 0.7 m/s, back pressure of 150 bar and metering stroke of 28 mm
c) Setting 3: Screw velocity of 0.3 m/s, back pressure of 50 bar and metering stroke of 80 mm

2.1 Tadmor

According to the Tadmor model, melting can be divided into three main steps: First, melt film formation is initiated as soon as the barrel temperature exceeds the material's melting temperature. Second, in the delay-zone, the melt film grows continuously due to heat conduction into the melt film and, dominantly, viscous dissipation within the melt film. A consistent melt layer is formed and transported by drag-induced flow between the barrel and the solid fraction. This mechanism was qualitatively described by Tadmor and Klein [3]. Finally, in the melting zone, a melt vortex is formed at the pushing flight of the screw and grows in a rectangular shape, while the solid-bed progressively decreases towards the screw tip [2].

2.2 Modified Tadmor

To better represent the observed behaviour of polyamide, the volume flow rate –comprising drag, pressure, and back flow—was modified to reflect a quadratic rather than a rectangular melt vortex. The revised model is:

$$\dot{V}_{stand} = \frac{1}{2} iwHv_{1z} - \frac{wH^3}{12\eta}\frac{dp}{dz} - \frac{wH}{\sin\varphi}\dot{s} \tag{1}$$

$$l_{sq} = \sqrt{wH} \tag{2}$$

$$\dot{V}_{sq} = \frac{1}{2} il_{sq}^2 v_{oz} - \frac{l_{sq}^4}{12\eta}\frac{dp}{dz} - \frac{l_{sq}^2}{\sin\varphi}\dot{s} \tag{3}$$

The volume flow rate for a rectangular melt pool $\dot{V}_{stand}$ is a function of the melt pool width w and height H, the barrel velocity in down-channel direction $v_{1z} = v_o\cos\varphi + \dot{s}sin\varphi$;$v_o = D\pi N$ being the velocity of the barrel, including the barrel diameter D and the number of revolutions N; the number of flights per revolution i, the melt viscosity η, the pressure gradient $\frac{dp}{dz}$, the flight angle φ and the axial screw velocity $\dot{s} = \frac{4\dot{m}}{D^2\pi\rho_m}$, with $\dot{m}$ being the mass flow rate without back flow and ρ_m the density of the polymer melt. For the quadratic melt pool, we introduce the equivalent side length of a quadratic melt pool with the same surface area as the rectangular one.

DOI: https://doi.org/10.26799/cp-polymers-composites-3Bsmaterials-2025

When the melt pool height l_{sq} reaches the channel height H, the quadratic melt pool has to transform back into a rectangular one. For addressing simulation stability constraints, the switch between the two formulations was smoothed by a blending factor f_{sq}:

$$f_{sq} = \min\left(1, \left(\frac{w}{H}\right)^6\right) \tag{4}$$

Using f_{sq}, the overall volume flow rate is computed as:

$$\dot{V} = \dot{V}_{stand} * f_{sq} + \dot{V}_{sq} * \left(1 - f_{sq}\right) \tag{5}$$

3 EXPERIMENTAL INVESTIGATION

To validate the simulation results, experiments were conducted using a standard three-zone-screw on an injection moulding machine (E-motion 310/100T) by the company ENGEL (Schwertberg, Austria). Table 1 shows the screw geometry. Process conditions and material were taken from Simulation and melting models section.

Table 1. Geometry of the standard-screw used in the experimental investigation

Description	Abbreviation	Value	Unit
Diameter	D_s	40	mm
L/D ratio	L/D	20	-
Pitch	t	40	mm
Flight width	e	4.8	mm
Channel height of feed section	h_f	6.125	mm
Channel height of metering section	h_m	2.675	mm
Length of feed section	l_f	9	D
Length of compression section	l_c	6	D
Length of metering section	l_m	5	D
Screw clearance	δ	0.125	mm

The melting behaviour was investigated using ultrasound sensors according to Altmann et al. [6]. Three sensors were mounted directly to the barrel at a distance of 220, 354, and 488 mm from the front edge of the barrel.

4 RESULTS

Figure 2 shows the solid bed fractions predicted by the standard or modified Tadmor models and obtained by experimental validation data from the ultrasonic measurements. In general, the altered volume flow rate in the modified Tadmor model lifts the melting curve. This reflects a reduced melting rate, which, for experiments 1 and 2, aligns more closely to the experimental data than the standard Tadmor model does. In experiment 3, the difference between the models becomes less distinct. However, the average deviation to experimental measurements was 0.057 [-] for the standard Tadmor model and 0.040 [-] for the modified version, in other words, the modified model agrees better with the observed data. Notably, the best fit between modified-model simulation and experiment was found at the sensor closest to the screw tip, which suggests that the modified Tadmor model predicts the melting completion point during the plasticizing phase more accurately.

DOI: https://doi.org/10.26799/cp-polymers-composites-3Bsmaterials-2025

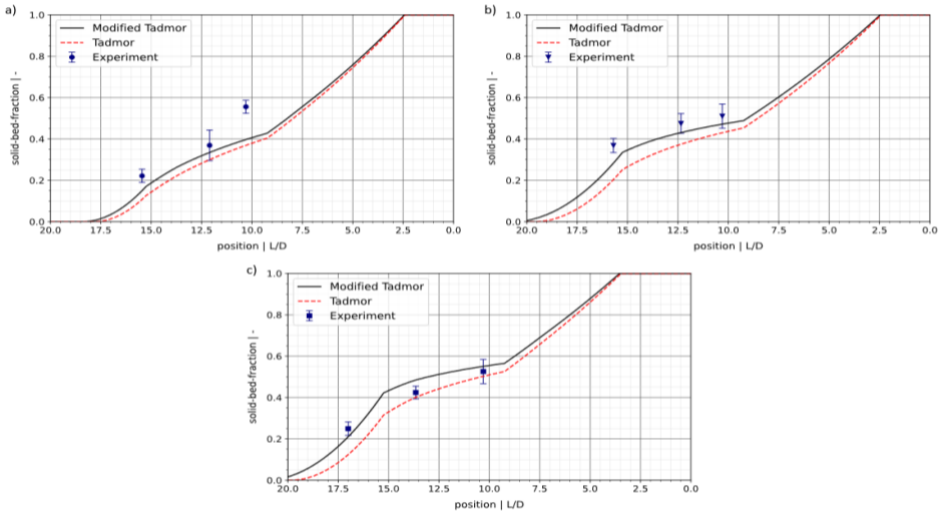

Figure 2: Comparision and validation of the standard and modified Tadmor models with experimental data for a) experiment 1, b) experiment 2, and c) experiment 3.

5 CONCLUSION

The modified Tadmor model significantly improved the prediction of the melting profile for PA6 compared to the classical Tadmor approach. This is particularly valuable for the design of the plasticizing processes and the screw geometries, as it reduces prediction errors and accelerates the overall development cycle. In this study, the volume flow rate was modified. Future work could include changing the modelling of the melting model itself and investigate the influence on the melting profile. In addition, broader testing under varied processing conditions is recommended, as this study focused exclusively on extreme parameter settings.

6 ACKNOWLEDGMENTS

Financial support by ENGEL AUSTRIA GmbH and WOOD K-PLUS, which play a substantial role by conducting parts of this work, are gratefully acknowledged. WOOD K-PLUS is funded by the Austrian Government and the Provincial Government of Upper Austria within the COMET program.

7 REFERENCES

[1] Bulk Chemicals, "Polyamide Market Size, Share & Trends Analysis Report By Product (Polyamide 6, Polyamide 66, Bio-based Polyamide), By Application (Engineering Plastics, Fibers), By Region, And Segment Forecasts, 2025 - 2030," 2024.

[2] Z. Tadmor, "Fundamentals of plasticating extrusion. I. A theoretical model for melting," *Polymer Engineering & Sci*, vol. 6, no. 3, pp. 185–190, 1966, doi: 10.1002/pen.760060303.

[3] Zehev Tadmor and Imrich Klein, *Enginieering Principles of Plasticating Extrusion*. New York: Van Nostrand Reinhold, 1970.

[4] Zehev Tadmor, Costas G. Gogos, *Principles of Polymer Processing*. New Jersey: Wiley-Interscience, 2006.

[5] Michael Aigner, "Computational and experimental modelling of transport phenomena in single screw an plasticating units under consideration of the melt quality," Ph.D thesis, Johannes Kepler University, Linz, 2014.

[6] D. Altmann, B. Praher, and G. Steinbichler, "Simulation of the melting behavior in an injection molding plasticizing unit as measured by pressure and ultrasound measurement technology," in Dresden, Germany, 2019, p. 40003.

Proceedings of the Polymers, Composites, 3BsMaterials 2025 Joint International Conferences
AlBufeira, Portugal – April 16 – 18, 2025
DOI: https://doi.org/10.26799/cp-polymers-composites-3Bsmaterials-2025

Is the Adsorption of Styrene on Clay Enhanced by Polymer?

E. Scholtzova[1]
[1]Department of Theoretical Chemistry, Institute of Inorganic Chemistry, Slovak Academy of Sciences
Dubravska cesta 9, 84536 Bratislava, Slovakia, eva.scholtzova@savba.sk

Abstract
Styrene is a technological compound widely used in material production. Since it belongs to volatile organics with harmful effects, its immobilization from the environment is crucial. The theoretical study of the hybrid styrene-montmorillonite (S-Mt) and styrene-modified montmorillonite by poly(2-methyl-2-oxazoline) polymer, S-P-Mt, showed the effect of the presence of polymer at the surface of the Mt to the trapping of styrene molecules from the environment. The calculated adsorption energies supported by hydrogen bonds analysis favour the S-P-Mt hybrid structure. The presence of polymer caused two times higher stability of the hybrid structures with trapped styrene.

Keywords: styrene, montmorillonite, polymer, pollutant, DFT, modelling, stability

1. Introduction

Styrene belongs to the fundamental industrial chemicals and, unfortunately, is also among the volatile organic compounds [Fig. 1] frequently used, e.g., in producing polystyrene, polyester resins, and glass fibres. Still, it is especially harmful even at very low concentrations. Inhalation causes respiratory problems, nose and throat damage, and lung damage and can also cause neurological effects such as fatigue, concentration problems, and even hearing loss [1].

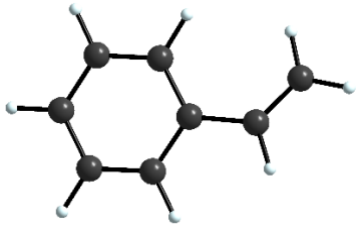

Fig. 1: Styrene molecule.

Regarding these serious effects, it is essential to implement an effective technology for removing styrene from the air, e.g., using a highly efficient ventilation system that supports a set of filters filled with an adsorbent, e.g., clay mineral [2]. In particular, the one mentioned can be created as a polymer-clay composite and be supplied as a consumable material to manufactured products in small quantities (~ 1–2% wt.), which is their quality and thus closes the production cycle and improves the operating economy [3]. In particular, smectites, a group of clay minerals, are suitable as efficient adsorbents of many environmental pollutants. They have a layered structure, and due to their high porosity, large specific surface area, surface charge, and surface functional groups, clay minerals function as adsorbents, filters, flocculates, and carbon stabilizers, for example [4]. They are also often used in combination with polymers because they improve the mechanical and thermal properties of polymers on one hand and own hydrophobic ones on the other [5].

Recently, computational modelling has also played an important role in characterizing the used or newly synthesized advanced materials for potential application in remediation processes [6, 7]. The comparative study of the two synthesized polymer-clay hybrid structures was enriched by the structural characterization of these materials by the DFT method [8], for example.

DOI: https://doi.org/10.26799/cp-polymers-composites-3Bsmaterials-2025

The present study aims to elucidate the effect of a neutral polymer, poly(2-methyl-2-oxazoline), modifying the natural clay mineral from the smectite family group, Ca-montmorillonite, for adsorption of styrene from the environment to improve the health conditions in the technological processes using a modelling approach. A polymer as a surfactant modifies clay surface to enhance its hydrophobic properties, and the synergic effect of polymer and clay properties for successful adsorption of styrene harmful molecules is expected.

2. Computational details

2.1. Computational method

The computational method based on the Density functional theory (DFT) implemented in the *ab initio* VASP program [9] was used for calculations. Since the presence of dispersion forces is expected, the D3 scheme [9] for their corrections was involved. The structural optimization was done at the *gamma* point because of the model's size using an energy cut-off of 400 eV.

The adsorption energy, E_{ads}, as a measure of the stability of hybrid systems, was calculated from the respective total energies, E_{tot}, according to the scheme:

$$E_{ads} = \Sigma E_{tot(products)} - \Sigma E_{tot(reactants)} \quad (1)$$

2.2. Computational models

The structural models representing one montmorillonite (Mt) layer with six octahedral Al^{3+}/Mg^{2+} compensating substitutions for three Ca^{2+} cations were prepared based on models from our previous work [1] to study the mechanism of effective styrene immobilization: first model of pristine Ca-montmorillonite with adsorbed styrene (S-Mt) and second model of hybrid structure of styrene - Ca-montmorillonite (Mt) modified by poly(2-methyl-2-oxazoline) polymer (P), S-P-Mt (Fig. 2). The pentamer unit of studied polymer (Fig. 3) fit the final size of computational cell (4*a*2*b*1*c*) with lattice vectors *a'*= 20.97 Å, *b'*= 18.18 Å, *c'*= 35.0 Å.

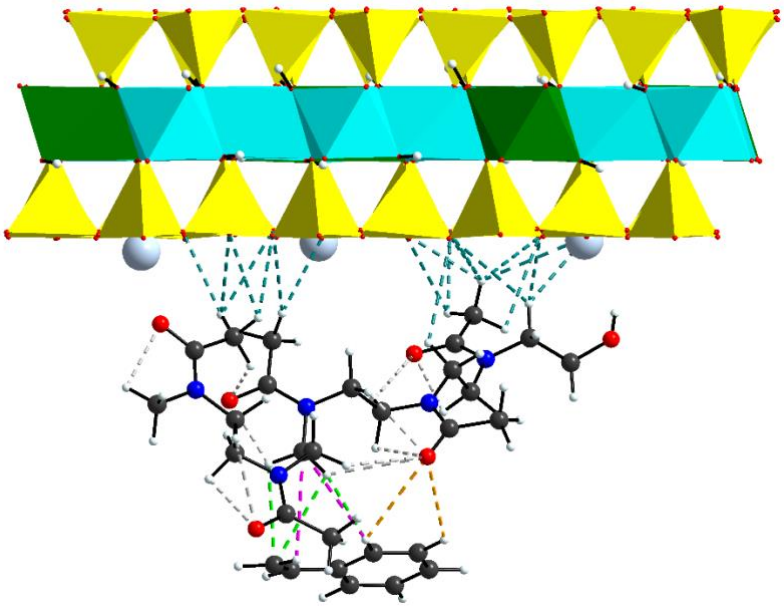

Fig. 2: Hydrogen bonds in the S-P-Mt hybrid structure. Styrene molecule at the bottom, polymer at the middle and Ca-montmorillonite on the top., yellow – tetrahedral sheets, cyan – Al^{3+}- octahedra and green – Mg^{2+}- octahedra form octahedral sheet. Colours of atoms: light blue Ca^{2+} cations, red – oxygen, black – carbon, blue – nitrogen and white – hydrogen atoms. Hydrogen bonds: gold – $C\text{-}H_s\cdots O_p$, green – $C\text{-}H_p\cdots C_s$, magenta – $C\text{-}H_s\cdots C_p$, light grey – $C\text{-}H_p\cdots O_{p\ intra}$ and petrol – $C\text{-}H_p\cdots O_b$.

DOI: https://doi.org/10.26799/cp-polymers-composites-3Bsmaterials-2025

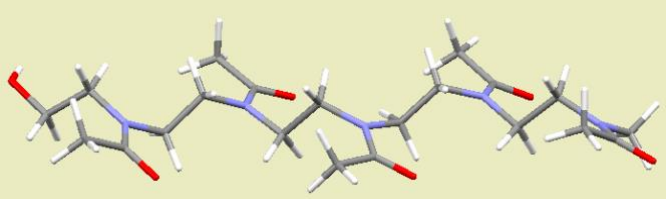

Fig. 3: Pentamer unit of poly(2-methyl-2-oxazoline).

3. Results and discussion

The adsorption energy was calculated, hydrogen bonds were examined in the system with polymer, and values were compared with the system without polymer [1] to evaluate the adsorption efficiency of styrene by montmorillonite modified with polymer (Table 1).

Table 1: D-H···A hydrogen bond distances (minimal, median, maximum) in Å, E_{ads} – calculated adsorption energy in kJ/mol; s-styrene, p-polymer, b-basal oxygens.

System	Hydrogen bond	D-H···A [Å]			E_{ads} [kJ/mol]
		min	median	max	
S-Mt [a)]	$C\text{-}H_s\cdots O_b$	3.12	3.44	3.55	-41.6
S-P-Mt	$C\text{-}H_p\cdots O_b$	2.49	2.85	3.29	-82.4
	$C\text{-}H_p\cdots O_{p\ intra}$	2.44	2.51	3.08	
	$C\text{-}H_s\cdots O_p$	2.94	3.04	3.14	
	$C\text{-}H_s\cdots C_p$	3.21	3.23	3.26	
	$C\text{-}H_p\cdots C_s$	2.92	3.05	3.10	

[a)] Matusik et. al. [1]

3.1. Adsorption energy of styrene

The calculated values of adsorption energy according to Eq. 1 revealed that the styrene molecule is adsorbed at least with twofold higher efficiency by polymer-modified clay (-82.4 kJ/mol) than pristine Ca-montmorillonite (-41.6 kJ/mol [1]).

3.2. Hydrogen bonds

The hydrogen bonds were evaluated according to criteria published by Desiraju and Steiner [10]. The D-H···A distances are present in Table 1 for illustration in minimal, median and maximal values. For the styrene-clay system (S-Mt), just one type of hydrogen bond exists ($C\text{-}H_s\cdots O_b$) of the weak strength (Table 1). The polymer in the system induced other types of hydrogen bonds of different strengths. An important fact is that polymer interacts with the clay surface by the moderate-to-weak $C\text{-}H_p\cdots O_b$ hydrogen bonds, which stabilize the modified clay structure. The $C\text{-}H_p\cdots O_p$ intra hydrogen bonds of moderate strength contribute to this stability by internal stabilization of the polymer unit. The styrene molecule interacts with the polymer through weak $C\text{-}H_s\cdots O_p$, $C\text{-}H_s\cdots C_p$ and $C\text{-}H_p\cdots C_s$ hydrogen bonds (Fig. 2). The presence of the additional functional groups in the interlayer space of clay plays a significant role in the enhanced adsorption effectivity of styrene due to the present additional interactions which act in the interlayer space of modified clay. The hydrogen bond strength correlates with the calculated adsorption energies. It should be mentioned that in both systems, except for the discussed hydrogen bonds also, electrostatic, van der Waals and dispersion interactions exist, which contribute to the overall stability of studied systems, concluding that the polymer enhances the adsorption of styrene from the environment.

4. Conclusions

The abundant natural clay Ca-montmorillonite forms a stable structure with styrene, which enables its immobilization and trapping from the environment. The studied polymer, poly(2-methyl-2-oxazoline), modifying the pristine Ca-montmorillonite raises the effectivity of the styrene immobilization twice.

DOI: https://doi.org/10.26799/cp-polymers-composites-3Bsmaterials-2025

Montmorillonite can be used as a cost-effective carrier of the polymer for efficient styrene removal from the environment. Pilot calculations showed the potential of studied hybrid structures consisting of natural clay and polymer to successfully remove styrene from the polluted air/water. However, further studies, analyses and also experiments are needed.

Acknowledgement

Funded by the EU NextGenerationEU through the Recovery and Resilience Plan for Slovakia under project No. 09I03-03-V04-00009.

References

[1] J. Matusik, *et al.*, "Induced π-complexation properties of smectites impregnated by Ni, Cu and Ag transition metals: The highly efficient styrene uptake," in *Applied Surface Science,* vol. 675, 2024.

[2] F. Bergaya and G. Lagaly, "Intercalation processes of layered minerals," in *13th Conference of the European-Mineralogical-Union (EMU) School on Layered Mineral Structures and their Application in Advanced Technologies*, Accademia Nazl Lincei, Rome, ITALY, 2011, pp. 259-284.

[3] E. S. Yanovska, *et al.*, "Sorption properties of saponite clay, in situ modified by poly(4-vinylpyridine-co-styrene), towards Cu(II), Cd(II), Pb(II), Mn(II) and Fe(III) ions," in *French-Ukrainian Journal of Chemistry,* vol. 7, pp. 145-152,2019.

[4] W. H. Yu, *et al.*, "Preparation of organo-montmorillonites and the relationship between microstructure and swellability," in *Clays Clay Miner.,* vol. 65, pp. 417-430,2017.

[5] P. F. Luckham and S. Rossi, "The colloidal and rheological properties of bentonite suspensions," in *Advances in Colloid and Interface Science,* vol. 82, pp. 43-92,1999.

[6] L. J. Wang, *et al.*, "Flocculation performance and mechanism of P (DMDAAC-AM) on clay mineral layer: Insights from DFT calculation and experiment," in *Appl. Surf. Sci.,* vol. 607, 2023.

[7] S. Bashir, *et al.*, "Mechanical properties of pristine smectite clay minerals and clay-polymer hybrids studied by density functional theory," in *Clays Clay Miner.,* vol. 72, 2024.

[8] J. Madejová, *et al.*, "Advanced materials based on montmorillonite modified with poly (ethylenimine) and poly(2-methyl-2-oxazoline): Experimental and DFT study," in *Colloids and Surfaces a-Physicochemical and Engineering Aspects,* vol. 659, 2023.

[9] S. Grimme, *et al.*, "Effect of the Damping Function in Dispersion Corrected Density Functional Theory," in *J. Comput. Chem.,* vol. 32, pp. 1456-1465,2011.

[10] G. Desiraju and T. Steiner, "The Weak Hydrogen Bond in Structural Chemistry and Biology," in *Oxford University Press, Oxford, UK.,* vol. 2nd edition, 2006.

Towards 100% circularity of plastics – a road map

.Geoffrey R Mitchell[1,2,*], Anabela P.Massano[1], Joao Matias[1], Pedro G.Martinho[1]

[1] Centre for Rapid and Sustainable Product Development, Polytechnic of Leiria, 2430-080 Marinha Grande, Portugal

[2]Visionary Equation lda, 2430-085 Marinha Grande, Portugal

Abstract:

After a century of the rapid development of plastics, attention has been redirected to the important question of sustainability. Many of the attributes of plastics, such as durability have turned out to be negative factors in the light of the poor management of plastics waste which has led to world-wide catastrophes both in the ocean and on the land [1]. Bioplastics are seen as one solution and chemical recycling is another. However, the success of plastics in the 20th Century poses many questions for the current use of materials, polyolefins and other thermoplastics have been found to be highly quality engineering plastics in terms of producing high quality parts for the safe distribution of water and electricity, lightweight materials for electric vehicles and so much more. These materials are easy to mass produce with high level of repeatability, surface finish and precision. Newer materials, including biobased materials lack one or more of these qualities. One route forward, is to increase the circularity of plastic parts [2]. In other words the granulated plastic materials at the end of the life of the part can be reused to make a new part with equivalent properties. Current practice leads to a fraction of plastic waste being recycled [2]. We explore the issues related to the practice of dealing with waste as a single stream from which materials are sorted. We contrast this with the possibilities which are available in closed loop recycling, where the product life is monitored throughout the life time of the product including its manufacturing pathway, so that the materials arriving for reuse have a well established origin, fabrication and product use cycle so that reuse becomes a much more straightforward process, than attempting to recycle a mixture of the same polymer type but with different compositions, processing pathways and product life cycles. We have set out a roadmap for such a system which we expect to explore with industrial partners in the near future. We believe that it is critical to understand all steps of the path from the feedstock pellets to the granulated plastic part to the end of life in order to understand how to design for recycling. Currently reuse and recycling is an afterthought when the end of life is reached. If we do not understand where property degradation occurs - in the manufacturing cycle? Or the product life cycle?, then how can we hope to design plastic parts which can be reused so as to achieve 100% circularity.

A key part of our road map is to explore in more detail the processing life cycle of the plastic part and we have chosen X-ray scattering as the technique with which to explore the transformations which take place in an injection moulding system We introduce this technique of operando x-ray scattering during injection moulding of plastics [3] and give examples of how we believe that it will provide much needed data on the effects of the processing life cycle and thereby help with design for recycling.

Keywords: circular economy, thermoplastics, end of life of plastic parts, property downgrading, operand X-ray scattering during injection moulding.

Introduction

Plastics were the material of the 20th Century. All of the basic concepts of polymer science were developed in the last century. A succession of Nobel Laureates from Herman Staudinger, through Karl Ziegler and Giulio Natta and Paul Flory toPierre G. de Gennes and on to Alan J. Heeger, Alan G. MacDiarmid, and Hideki Shirakawa [4], plots progress of the development of polymer science through the 20th century to the point where we can now produced tailored polymers for almost every possible application. Towards th end of the 20th Century, it began to

dawn on society that many of the advantages of polymers such durability had another negative side. In 2009 Thompson et al reviewed the many benefits of plastics to society along side the environmental concerns of plastic waste in the envvironment [5]. In 2018, the European Parliament established new rules for plastics in the EU [6] and laid out a challenge to develop a circular economy for plastics by 2050 [7]. This ms sets out to answer two questions, the first is a circular economy possible with plastics? And secondly how to achieve it? The EU parliament document defines the circular economy as "The circular economy is a model of production and consumption, which involves sharing, leasing, reusing, repairing, refurbishing and recycling existing materials and products as long as possible. In this way, the life cycle of products is extended" [7]**.** The document also states "In practice, it implies reducing waste to a minimum. When a product reaches the end of its life, its materials are kept within the economy wherever possible thanks to recycling. These can be productively used again and again, thereby creating further value.
This is a departure from the traditional, *linear* economic model, which is based on a take-make-consume-throw away pattern. This model relies on large quantities of cheap, easily accessible materials and energy." A first step in the elimination of "planned obsolescence", "when a product has been designed to have a limited lifespan to encourage consumers to buy it again" [7]. A bizarre system of waste collection which groups all waste together has become common practise, thereby developing an industrial scale problem of sorting plastic products in the plastic types. Such an approach loses the connection between the plastic product, its manufacturing process and its lifecycle. We propose an alternative closed loop approach.

Methodology

In Figure 1, we show the basic stages of manufacturing a plastic part, after the plastic feed stock has been synthesised. The first stage is fabricating the part, here we show the use of injection moulding technology the most common rocess used for shaping plastics. The injection moulding involves the injection at high pressure of a metered volume of molten plastic in to a metal mould, the plastic cools, solidifies and is ejected from the mould retaining the shape of the part imposed by the mould. This moulding cycle takes tens of seconds and the plastic is subjected to high temperature and harsh flow conditions. We can reasonably assume that during the processing cycle the polymeric materials is degraded, for example, breaking the chains. This means that the part at end of life when granulated to make feedstock to reuse the plastic to make a new part, the properties will be lower than of the virgin materials. Other than the sorting, this downgrading of the properties in the recycled materials is one of the major problems in the circular economy. leads to a down rating of the value of the reused material and its use in less demanding products and applications. We are evaluating the consequences of repeated reprocessing of the same polymer using operando X-ray scattering measurements. We exploit the intense X-ray intensities available at beamlines of synchrotron facilities. IN particular we make use of the NCD-SWEET beamline at the ALBA Synchrotron Light Source in Barcelona,

Spain [8]. Figure 2 shows a schematic of the ALBA Facility.

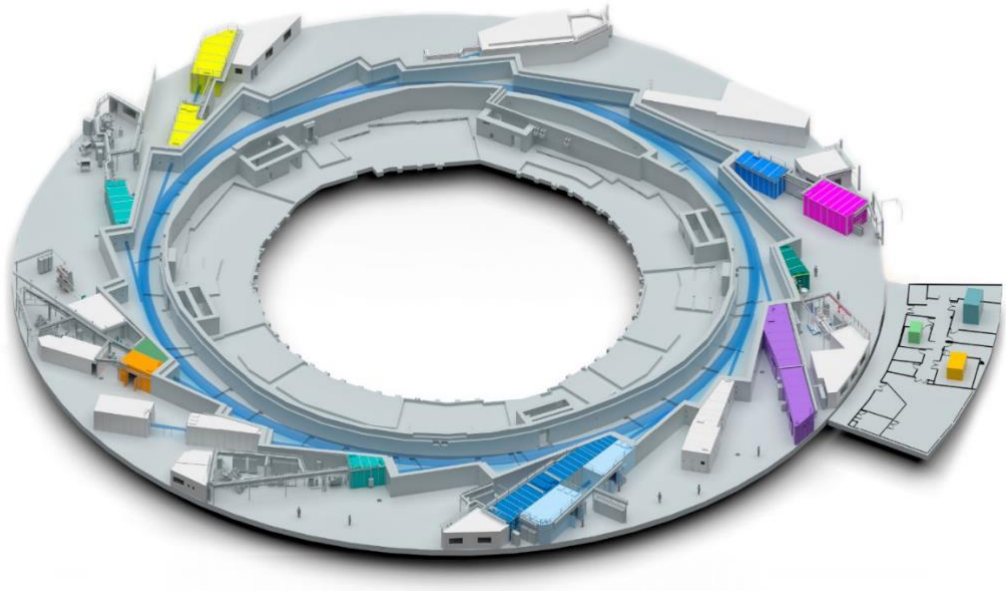

Figure 2 A schematic of the ALBA Synchrotron Light Source in Barcelona. The block in purple is the NCD-SWEET Beamline used in this work. Reproduced from [8]

The ALBA facility is a system of electron accelerators which accelerate electrons to close to the speed of light. They appear to circulate in a rings (shpwn in blue in Figure 2) but which in reality is polygon structure in which the electrons travel in straight lines at the vertices of the polygon, a bending magnet changes the direction of travel. The facility houses a number of different beam lines all focuses on studying the structure of materials. Currently it has 14 beamlines, one of which is currently under construction.

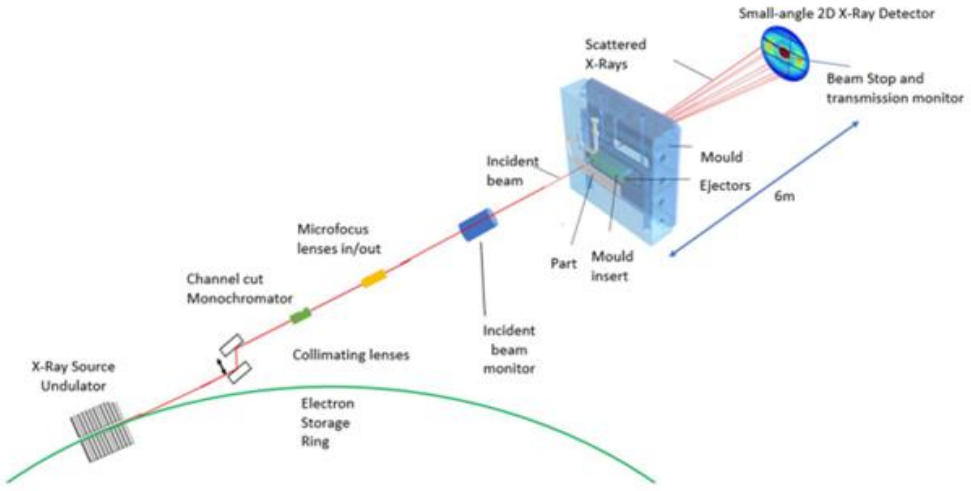

Figure 3 A schematic of the NCD-SWEET beamline from source to detector Reproduced from Reference [9] Under the terms of CC BY 4.0 licence.

The source of X-rays for the NCD_SWEET beamline is a vacuum undulator, which is a period array of permanent magnets. Th electron current circulating around the main "ring" at sppeds close to the speed of light passes through the undulator and the magnetic fields cause each electron to deviate from its path, thereby accelerating the electrons which then radiate x-rays and the periodic pattern of magnets results in interference of the X-rays resulting in a coherent source both in terms of energy and space. As the undulator is a periodic devices it emits a series of harmonics and the beam line selects one of these harmonics, in the experiments performed here, we used the 7th Harmonic with an energy of 12.4keV and a wavelength of 1Å. The intensity of the beam is a billion times brighter than a laboratory based source. We have

designed and developed an injection moulding system of industrial relevance which can be mounted on the NCD-Beamline (Figure 4) [3,9].
This system is able to measure the small-angle X-ray scattering in real-time during the injection moulding cycle and allows us to evaluate the transformation of the molten plastic to solid material and the measurement of the transmission signal through the mould enables the extent of mould filling to be quantitatively evaluated [3,9]. How does this relate to the circularity of the process and of the material? When the molten polymer is injected in to the metal mould it experiences high forces related to the flow and rapid temperature changes, this appears to us to be an area of prime concern for the breakage of polymer chains due to the high stresses [10]. Typically polymer scientists used gel permeation chromotograph techniques calibrated with narrow molecular weight fractions. It is fair to state that this is not a highly sensitive technique and not an ideal systems for detecting relatively small changes in the molecular weight distribution. A number of researchers have used optical measurements coupled to a flour roll mill geometry to evaluate relaxation after strong elongational flow. This work showed that for chains in dilute solution chain scission occurred in the centre of the chains. Recent work using molecular dynamic simulations shows that in the melt, the situations is more complex and chain scission is less likely when the chain is fully extended [10]. We know from previous work that the long chains which are extended in flow will also act as row nuclei [11] and template a high level of preferred orientation of chain folded lamellar crystals nucleated by the row nuclei as shown schematically in Figure 6.

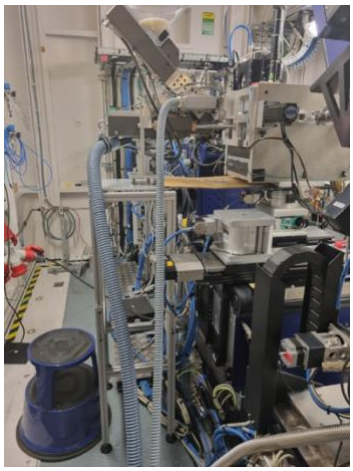

Figure 5 The operando X-ray scattering during injection moulding mountedon the NCD-SWEET beamline. [9]

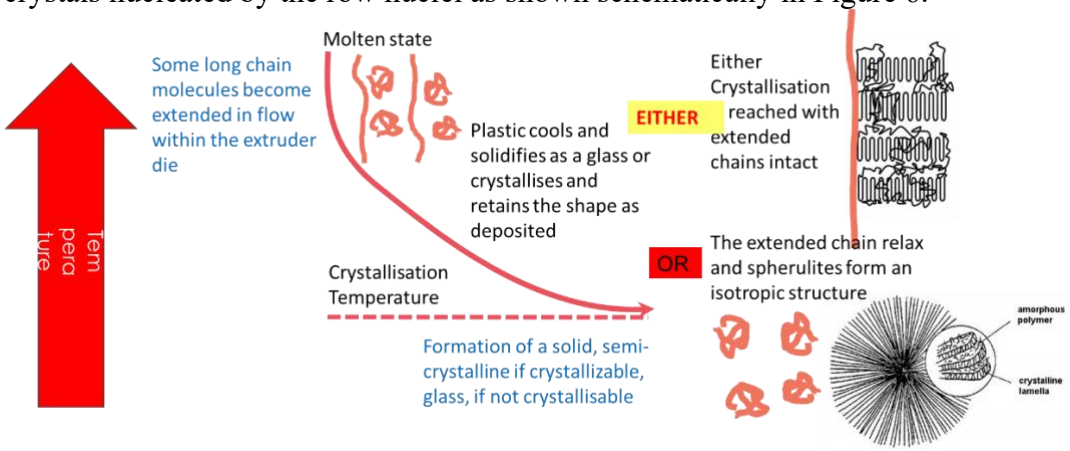

Figure 6 A schematic of how long chain may become extended in flow and consequently nucleated chain folded crystals which grow out normal to the extended chains.
Figure 7 shows time-resolved small-angle X-ray scattering measured using the equipment shown in Figure 5 revealing for the first time the crystallisation process taking place in the first couple of second after the molten plastic enters the mould in the case of polypropylene (6A) and the different behaviour recorded for a polyethylene material [9]. We will use these data to develop a quantitative model of the mechanical degradation which takes place during the injection moulding cycle and which leads to property degradation in repeated recycling.

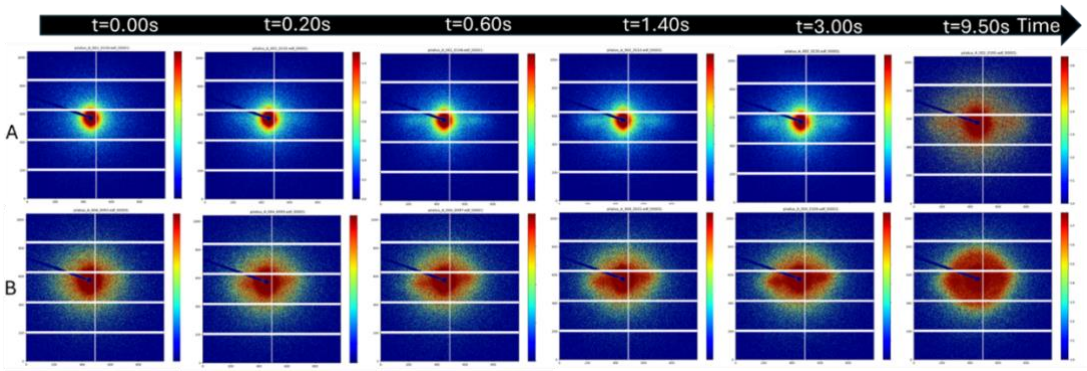

Figure 6 Time-resolved small-angle X-ray scattering patterns recorded during the first few seconds of an injection moulding cycle for (A) isotactic polypropylene and (B) Polyethylene [9] Reproduced from Reference [9] under therms of CC BY 4.0 license

Summary

We have laid out a road map of research to develop an understanding of the degradation of properties in the successive reuse of material obtained from end of use products. We have already developed the operando X-ray scattering equipment to record quantitatively X-ray scattering during injection mould. In the next 12 months we will be using these data to develop a model which enables us to identify the critical points in the fabrication cycle and in the life cycle of the product to lead to a fully circular process.

Acknowledgements

This work is supported by the Fundação para a Ciência e Tecnologia(FCT) through the Project references: MIT EXPL/TDI/0044/2021, UIB/04044/2023, PRR 2375 500 ioshoes4All and PRR INOVAM and by Visionary Equation lda.

References:

1. Fonseca AR, Batista R, Mateus A, Faria PP, Mitchell GR* (2022) Circular Seas - The Next Challenge for Plastics Polymer Science: Peer Review Journal 3 (1), 3 Open Access
2. https://research-and-innovation.ec.europa.eu/research-area/environment/circular-economy/plastics-circular-economy_en#:~:text=Latest-,The%20Commission%27s%20plan%20for%20plastics,plastics%20as%20a%20priority%20area. Online access 16.03.2025
3. Costa, A.A., Gameiro, F., Massano, A.P. *et al.* Industrially relevant injection moulding apparatus for in situ time-resolving small-angle X-ray scattering measurements. *Int J Adv Manuf Technol* **132**, 4737–4752 (2024). https://doi.org/10.1007/s00170-024-13651-3
4. Joseph, T.M.; Hasanin, M.S.; Unni, A.B.; Kar Mahapatra, D.; Haponiuk, J.; Thomas, S. Macromolecules: Contemporary Futurist Thoughts on Progressive Journey. Eng 2023, 4, 678-702. https://doi.org/10.3390/eng4010041
5. Thompson Richard C., Moore Charles J., vom Saal Frederick S. and Swan Shanna H. 2009Plastics, the environment and human health: current consensus and future trendsPhil. Trans. R. Soc. B3642153–2166
6. Plastic pellet losses online https://www.consilium.europa.eu/en/press/press-releases/2025/04/08/plastic-pellet-losses-council-and-parliament-agree-on-new-rules-to-reduce-microplastic-pollution/ accessed 12th April 2025
7. New circular economy action plan online https://www.europarl.europa.eu/legislative-train/theme-a-european-green-deal/file-new-circular-economy-action-plan accesed 12th April 2025

8. ALBA Synchrotron Light Source online https://www.cells.es/en/ accessed 12th April 2025
9. Massano AP, Vargas P, Carreira P, Matias J, Malfois M, Novo PJ, Martinho P, Pontes A and Mitchell GR (2024) Towards dynamic multiscale feedback during the injection moulding cycle of plastics. Front. Mater. 11:1466753. doi: 10.3389/fmats.2024.1466753
10. Chongvimansin, Nattavipa, O'Connor, Thomas C. "The Work of Mechanical Degradation in Elongating Polymer Melts" Macromolecules (2025) 58 1787-1794 10.1021/acs.macromol.4c02063
11. Daniel P. da Silva, James J Holt, Supatra Pratumshat, Paula Pascoal-Faria, Artur Mateus, and Geoffrey Robert Mitchell* "Crystallisation from Anisotropic Polymer Melts" Chapter 10 in "Polymer crystallization: Methods, Characterization, and Applications", editors Dr. Jyotishkumar Parameswaranpillai, Dr. Jenny Jacob, Dr. Senthilkumar Krishnasamy, Dr. Aswathy Jayakumar, and Dr. Nishar Hameed Wiley-VCH 2023 pp 255-283 ISBN: 978-3-527-35081-0

Proceedings of the Polymers, Composites, 3BsMaterials 2025 Joint International Conferences
AlBufeira, Portugal – April 16 – 18, 2025
DOI: https://doi.org/10.26799/cp-polymers-composites-3Bsmaterials-2025

Defect Analysis and Microstructural Characterization of 3D-Printed Sintered Parts of Ceramic Matrix Composites (Cordierite-Graphene)

A. García-Juarez[2], I. Esguerra-Arce[1*], Juan García-Martínez[1], J. Hidalgo García[2], L. Illán Andrés[1], R Giménez[2], Ana Pastor Muro[1], C. Berges[2], G. Herranz[2], María García-Martínez[1]

[1]National Institute of Aerospace Technology (INTA),
Ctra. Ajalvir km 4,4, 28850 Torrejón de Ardoz, Madrid, Spain. garciamam@inta.es
[2]Castilla La Mancha University (UCLM), DYPAM Research Group,
ETSII-INEI, Avda. Camilo José Cela s/n, 13071 Ciudad Real, Spain. alvaro.garcia@uclm.es

Abstract
The design and manufacture of aerospace parts still face significant challenges, particularly due to the inherent brittleness and hardness of ceramics, which make them difficult, or even impossible, to machine for improved surface finish or intricate geometric shapes. The advancement of 3D printing technologies provides a promising, precise, and efficient approach for producing parts with these characteristics. Aerospace materials must possess exceptional performance, strength, durability, and heat resistance. Traditional technical ceramics such as cordierite exhibit high chemical and thermal stability, very low thermal expansion coefficient, high thermal shock resistance, low dielectric constant, and high resistivity. These properties make cordierite an excellent candidate for aerospace applications. In this study, the effect of reduced graphene oxide (rGO) on the microstructure and properties of cordierite-based composites was investigated. Composites with different rGO concentrations were fabricated by 3D printing, followed by sintering. Elemental characterization of raw materials was performed using energy-dispersive X-ray spectroscopy (EDS), and Fourier-transform infrared (FTIR) spectroscopy. Crystalline phases were analyzed using X-ray diffraction (XRD) and optical microscopy. Defect analysis of the 3D-printed parts was conducted using optical microscopy, and measurements were performed using ImageJ software. Microstructural analysis was carried out using optical microscopy, SEM-EDX, and XRD. In conclusion, the addition of rGO in cordierite composites offers new opportunities for designing advanced aerospace materials, where thermal and mechanical properties are critical. The defects observed in 3D-printed parts impact material strength but also provide opportunities to optimize manufacturing processes.

Keywords: Additive manufacturing-AM, Cordierite, Reduced Graphene Oxide, rGO, Nanocomposite

1. Introduction

Ceramic components are increasingly considered for aerospace applications due to their excellent thermal and chemical stability, low density, and mechanical resilience. However, their intrinsic brittleness and hardness present substantial limitations for conventional shaping and machining. These constraints have motivated the exploration of advanced manufacturing techniques such as additive manufacturing (AM), which enables direct fabrication of geometrically complex parts with tailored architectures. Among ceramic materials, cordierite ($2MgO \cdot 2Al_2O_3 \cdot 5SiO_2$) stands out due to its extremely low thermal expansion coefficient, high thermal shock resistance, low dielectric constant, and high resistivity [1], making it ideal for aerospace and electronic applications. Ceramic matrix composites (CMCs) are considered a key technology in aerospace due to their theoretical properties and their potential to replace metals in high-temperature structural applications [2]. Graphene and its derivatives (rGO and GO) are two dimensional planar reinforcements with high surface area and are frequently used as nanofillers due to their ability to produce significant effects on certain properties even at very low concentration [3]. AM refers to the layer-by-layer construction of aerospace and defense parts using a 3D digital model and offering on-demand fabrication of complex structures without the limitations of traditional methods [4]. Pellet Material-Extrusion (Pellet-MEX) involves shaping parts from pellets composed of ceramic precursor powders (60%

DOI: https://doi.org/10.26799/cp-polymers-composites-3Bsmaterials-2025

vol.) and organic binder system. The binder is removed in subsequent steps through chemical solvents and/or thermal treatments, followed by a final sintering process to achieve the desired geometric characteristics and properties according to design specifications. AM-related defects can be assessed by image analysis, which has proven to be reliable and comparable to conventional methods [5]. This study investigates the effect of rGO (0, 0.25 and 0.5% wt.) on the microstructure and porosity of cordierite-based composites shaped by pellet-MEX and sintered.

2. Materials and Methods

Preliminary studies were carried out to select raw materials, and optimize rheological and thermal parameters [6]. Cordierite precursor powders (CPP) were provided from VICAR (wt. %: 48.7SiO_2, 44.3Al_2O_3, 2.9MgO, 0.8Fe_2O_3, 0.3CaO, 0.4Na_2O, 1.2K_2O, 0.8TiO_2, 0.6 others). rGO powder from Layer One was used as reinforcement.
Preparation involves sonication of rGO in a binder (paraffin wax, polyethylene and stearic acid), followed by mixing with CPP, extrusion into filaments, and cutting into pellets 2.5 cm long. Shaping was performed via 3D printing process with 100% infill, double wall, and ±45º deposition pattern. Parts underwent solvent debinding, thermal treatment, and sintering.
Material characterization included SEM-EDX (Thermo Scientific Apreo + Oxford EDX), F-TIR (iS50, Thermo Fisher) and XRD (PANalytical X´Pert Pro, analyzed with Xpert HighScore). Density was measured using Archimedes' method at room temperature. Optical micrographs were acquired using a Leica MEF4M/DMC2900 microscope. Image analysis was performed in imageJ V1.54g (NIH), and conditional formatting in Excel was used to classify porosity ranges following L. Čelko et al.[8].
Manufacturing defects observed included poor contact between filaments and interfilament porosity. 2D image analysis was performed using micrographs from XY (frontal), ZX (longitudinal) and ZY (transverse) planes (see bar chart headers in Fig. 3). Terrys et al [7] methodology was followed to define the analysis parameters. For pores ≥ 1000 μm^2 (3D printing defects), optical magnification was selected based on the phase and porosity morphology. At 5x magnification (pixel size 0.98 µm), pores > 0.96 μm^2 could be resolved. Mosaic micrographs (24x25 tiles, 2048x1536 px), were stitched using a motorized stage and assembled using LAS X (Leica).
For pores ≤ 1000 μm^2, 20x magnification (pixel size 0.18µm) enabled resolution of pores > 0.03 μm^2 and enhanced contour resolution and phase contrast between the amorphous region and the pores.
To assess pores ≥ 1000 μm^2, the representative elemental area (REA) was calculated following Martin y Putman method [5] for cross-sample comparison. For pores ≤ 1000 μm^2, ten micrographs per sample were analyzed to stabilized porosity percentages and standard deviations.

3. Results and discussion

The starting materials (CPP and rGO) were characterized to disclose the structural and morphological characteristics. Fig. 3a-d show SEM micrograph, EDX confirmation, XRD pattern and FTIR spectrum of CPP, revealing a white and inhomogeneous morphology. Fig. 3b shows the EDX analysis, confirming the presence of the elements indicated by VICAR. Fig. 3c presents the XRD pattern, confirming the presence of the main precursors of CPP: MgO, Al_2O_3 and SiO_2. Fig. 3d displays the FTIR-ATR spectrum, confirming the absence of bands O-H (~3460 cm^{-1}) and the presence of signature bands of MgO (~650 cm^{-1}), Al_2O_3 (Al-O: ~561 cm^{-1}, ~685 cm^{-1} and ~1165 cm^{-1}) and SiO_2 (Si-O-Si: ~450 cm^{-1}, and ~1057 cm^{-1} and Si-O: ~482 cm^{-1},605 cm^{-1} and 1084 cm^{-1}).
Regarding the rGO, Fig. 3e-e1 show the SEM image of the rGO sample and the morphology of the original precursor powder. The presence the oxygen is confirmed by EDX (Fig. 3f). Fig 3g presents the XRD pattern, which exhibit broad peak characteristic of the nanoplatelet structure of rGO precursor (prior to the sonication process). Fig. 3h displays the FTIR-DRIFT spectrum, confirming the presence of characteristics rGO bands: -CH_2 (~2918 cm^{-1} and ~2848 cm^{-1}), C=C (~1593 cm^{-1} and ~1261 cm^{-1}), O-H stretching (~3400 cm^{-1}), -C=O stretching (~1743 cm^{-1}).
The SEM-EDX micrographs (Fig. 2a-c) show the sintered ceramics microstructure, consist of a multiphase material that contained crystallized and vitreous phases. A matrix consists of cordierite and acicular crystals of crystallized mullite, with alumina and silica small particles, consistent with EDS mapping and peaks indexed in XRD pattern.

DOI: https://doi.org/10.26799/cp-polymers-composites-3Bsmaterials-2025

In addition, the XRD pattern shows a broad peak between 2θ = 15°–30°, which corresponds to the presence of a residual vitreous phase in the composite.

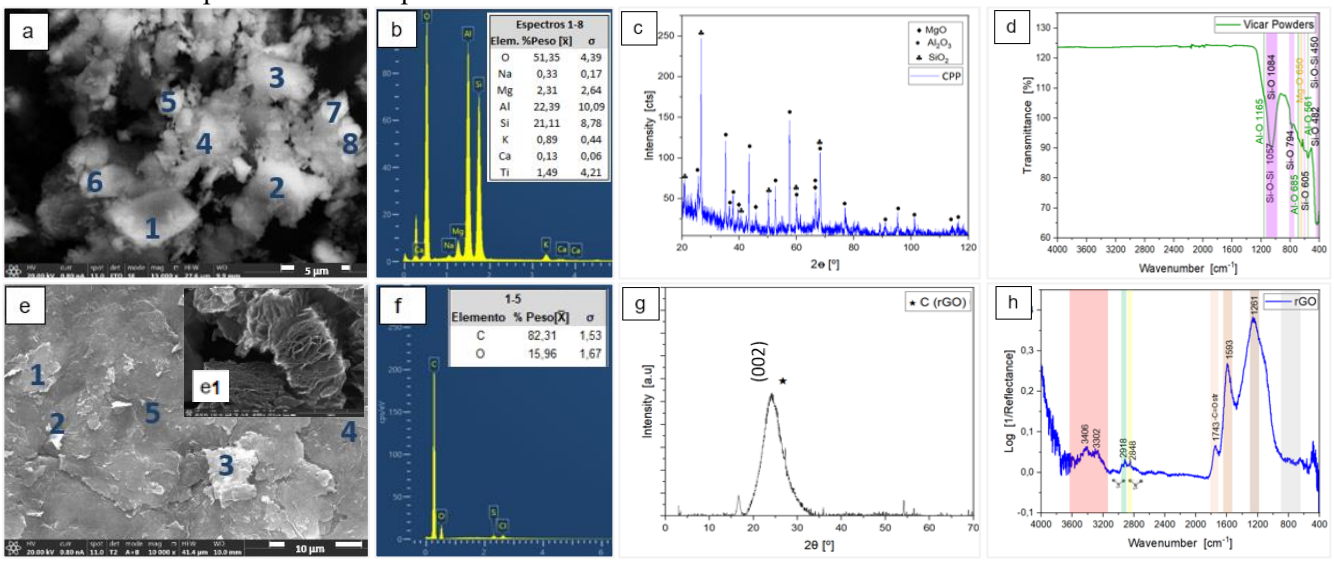

Fig. 1.Raw material characterization. CPP: a. SEM image (15,000x), b. EDX results, c. XRD pattern and d. FTIR-ATR. rGO: e. SEM image (10,000x) e1. (15,000x), f. EDX results, g. XRD pattern and h. FTIR-DRIFT spectrum.

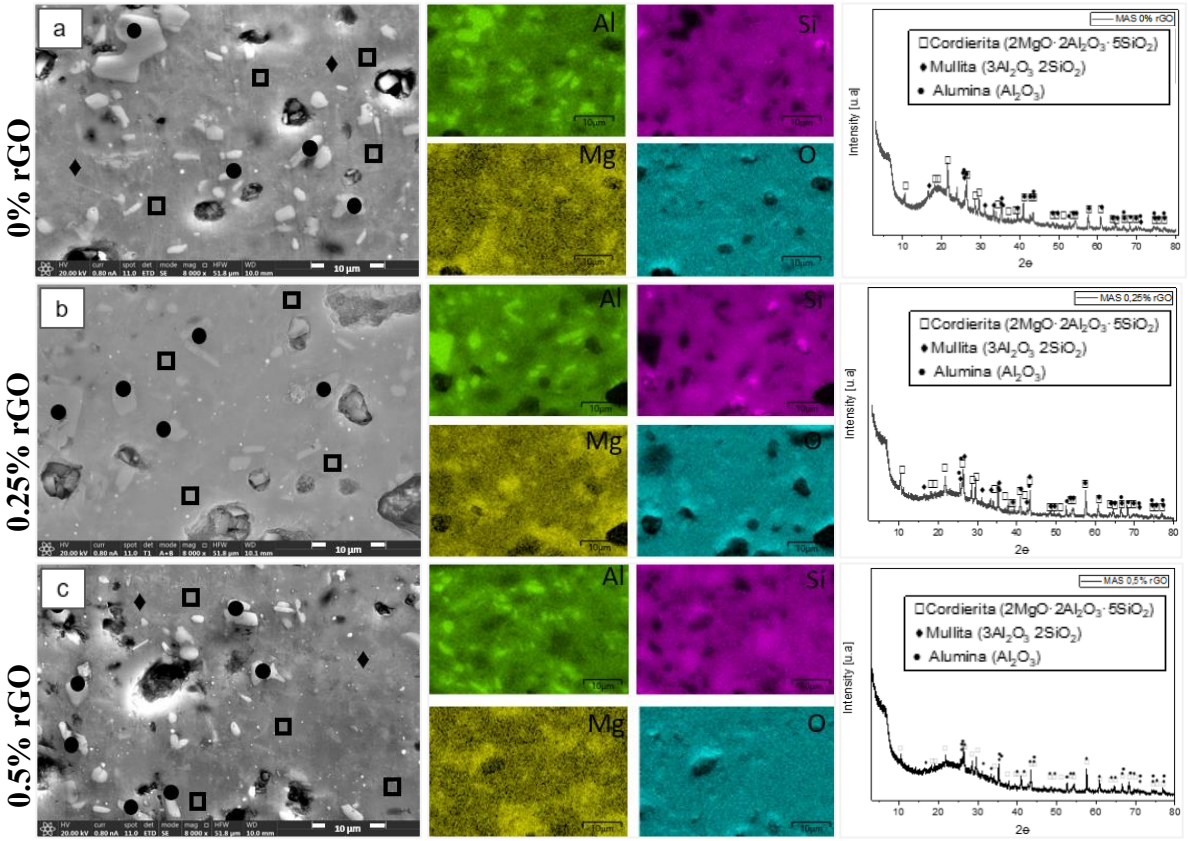

Fig. 2. SEM images (8000X), EDX mapping and XRD of sintered samples with: a. 0% rGO, b. 0.25% rGO and c. 0.5% rGO

The density results for sintered samples with 0%, 0.25% and 0.5 %rGO were: 2.46 ± 0.01 g/cm^3, 2.38±0.01 g/cm^3, 2.56 ±0.01 g/cm^3 respectively.

DOI: https://doi.org/10.26799/cp-polymers-composites-3Bsmaterials-2025

Fig. 3 shows the porosity percentages obtained from image analysis in the frontal, transverse and longitudinal planes for both pore size ranges. For pores ≥ 1000 μm² (Fig. 3a), total porosity values were 3.7%, 3.5% and 0.7% for CPP samples with 0%, 0.25% and 0.5 %rGO, respectively. Fig 3b shows the porosity for pores ≤ 1000 μm²: 19.6%, 16.9% and 4.7% for same rGO contents. The similarity between 0% rGO and 0.25% rGO aligns with their comparable density values. The 0.5% rGO sample exhibited the lowest porosity and the highest density.

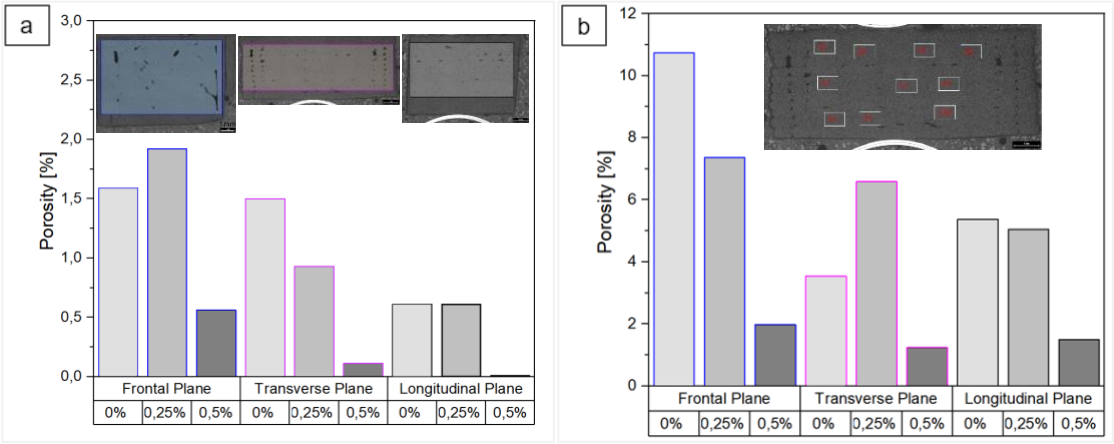

Fig. 3. Comparison of porosity measurements for 3D printed related pores: a. area ≥ 1000μm² b. area ≤ 1000μm²

4. Conclusion and future works

This study demonstrates the feasibility of analyzing 3D-printing-related porosity using 2D optical image analysis. The analysis of pores with areas ≥ 1000 μm² correlated well with the density values measured for each formulation. Future work will focus on evaluating the influence of porosity and microstructure on mechanical properties such as flexural and compressive strength.

Acknowledgements

Grant AERORECORD-3D Project (PID2021-125612OA-C22 and PID2021-125612OB-C21), funded by MICIU/AEI/10.13039/501100011033, by ERDF A way of making Europe.

References

1. Y.-M. Sung, *et al.*, «The effect of additives on the crystallization and sintering of 2MgO-2Al2O3-5SiO2 glass-ceramics», *J Mater Sci*, vol. 31, n.º 20, pp. 5421-5427, oct. 1996.
2. X. Wang, *et al.*, «Advances in modifications and high-temperature applications of silicon carbide ceramic matrix composites in aerospace: A focused review», *Journal of the European Ceramic Society*, vol. 41, n.º 9, pp. 4671-4688, ago. 2021.
3. A. Smirnov, *et al.*, «Processing and mechanical properties of new hierarchical metal-graphene flakes reinforced ceramic matrix composites», *Journal of the European Ceramic Society*, vol. 39, n.º 12, pp. 3491-3497, sep. 2019.
4. R. P. Chaudhary *et al.*, «Additive manufacturing of polymer-derived ceramics: Materials, technologies, properties and potential applications», *Progress in Materials Science*, vol. 128, p. 100969, jul. 2022.
5. W. D. Martin, B. J. Putman, y N. B. Kaye, «Using image analysis to measure the porosity distribution of a porous pavement», *Construction and Building Materials*, vol. 48, pp. 210-217, nov. 2013.
6. J. Hidalgo, *et al.*, «Ceramic injection moulding adequacy in the fabrication of graphene reinforced cordierite–mullite for high-temperature applications», *Boletín de la Sociedad Española de Cerámica y Vidrio*, vol. 64, n.º 2, pp. 122-137, mar. 2025.
7. T. de Terris *et al.*, «Optimization and comparison of porosity rate measurement methods of Selective Laser Melted metallic parts», *Additive Manufacturing*, vol. 28, pp. 802-813, ago. 2019.
8. L. Čelko *et al.*, «Characterization of porosity and hollow defects in ceramic objects built by extrusion additive manufacturing», *Additive Manufacturing*, vol. 47, p. 102272, nov. 2021.

Proceedings of the Polymers, Composites, 3BsMaterials 2025 Joint International Conferences
AlBufeira, Portugal – April 16 – 18, 2025
DOI: https://doi.org/10.26799/cp-polymers-composites-3Bsmaterials-2025

Predictive Modeling of Porosity Characteristics in High-Pressure Hydrogen Tanks using Augmented Fuzzy Cognitive AI

Lina ACHOUR[1,2], Zyed ZALILA[3,4], Zoheir ABOURA[1], Benjamin LORENTZ[4], David RUGGI[2], Kamel KHELLIL[1]

1: Roberval, Université de Technologie de Compiègne. Royallieu Research Center, CS 60319-60203, Compiègne
lina.achour@utc.fr, zoheir.aboura@utc.fr and kamel.khellil@utc.fr
2: H2-Power, OPmobility. ZAC du Bois de Plaisance, 214 Avenue de la Mare Gessart, 60280 Venette
david.ruggi@opmobility.com
3: Costech, Université de Technologie de Compiègne. 60200 Compiègne
4: IDAGRAI LABS (Intellitech). 60200 Compiègne
zyed.zalila@intellitech.fr and benjamin.lorentz@intellitech.fr

Abstract
High-pressure type IV hydrogen storage vessels made from carbon fiber reinforced polymer composites are critical for mobile and stationary hydrogen applications. Despite their high strength to weight ratio, these vessels remain prone to internal porosities that can compromise structural performance and long-term reliability. This study focuses on predicting the porosity count based on manufacturing process parameters using XTRACTIS, a General Reasoning Artificial Intelligence (GRAI) tool. From 58 collected variables, XTRACTIS automatically selected 15 relevant predictors and induced 54 fuzzy IF…THEN rules organized into 26 disjunctive rules. The resulting regression model achieved strong generalization on an external test dataset with a correlation coefficient of 0.824 and a Root Mean Squared Error (RMSE) of 7.94%, using only 4.8 predictors per rule on average. The intelligibility of the obtained Xtractis unitary model was rated 3.52/5, enabling the identification of key process parameters such as bobbin-specific fiber tension, mandrel rotation speed, and winding angle as critical factors affecting porosity. Rule analysis revealed that low or heterogeneous tension, slow mandrel speed, and non-optimal winding angles significantly increased void formation. This study demonstrates the potential of augmented fuzzy cognitive AI not only to efficiently predict porosity count, but more importantly to automatically discover interpretable rules that support defect prevention, process optimization, and expert-guided continuous improvement in composite vessel manufacturing.

Keywords: Porosity, high-pressure hydrogen vessels (HPV), X-ray tomography, General Reasoning AI, Xtractis / Fuzzy Cognitive AI

1. Introduction

High-pressure type IV hydrogen vessels (HPV) play a vital role in hydrogen storage and distribution, especially in industrial systems and fuel cell vehicles. These vessels combine a polymer liner with carbon fiber-reinforced composites, offering both strength and light weight [1]. Their structural design provides high fatigue tolerance and durability [2], while minimizing weight and maximizing storage efficiency.

However, internal defects such as porosities remain a critical concern [3] [4]. Even though certification allows for a certain level of porosity, excessive or poorly distributed voids can weaken mechanical integrity and lead to failure [5] [6]. These porosities are closely linked to numerous parameters in the manufacturing process, particularly during the filament winding step [7].

Given the complexity of these interactions and the number of variables involved, 58 in total, purely physical modeling approaches, carried out by a human scientist, lead to erroneous or suboptimal models. Consequently, a data-driven methodology appears more suitable to build predictive models that relate manufacturing settings to porosity formation, aiming to optimize the process and reduce defect occurrence.

In this study, we focus on the prediction of porosity count using the XTRACTIS General Reasoning AI (GRAI), invented and developed by Dr. Zyed Zalila (IDAGRAI LABS / Intellitech). XTRACTIS extends the three modes

DOI: https://doi.org/10.26799/cp-polymers-composites-3Bsmaterials-2025

of human reasoning (induction, deduction and abduction) to an infinite dimensionality and to the infinity of continuous logics. Particularly, this GRAI is capable of automatically discovering, from data, robust and transparent models in the form of fuzzy IF…THEN rules [8]. Unlike opaque black-box models, GRAI offers intelligibility, supporting root cause analysis and process improvement by modeling weak signals and nonlinear interactions often missed by conventional approaches [9].

2. Methodology

This study utilized 58 process and design variables related to filament winding manufacturing of Type IV hydrogen vessels such as fiber tension, deposition speed, and winding type that influence porosity formation and vessel quality. Sensor readings sometimes returned zeros when measurements failed; these were treated as missing values and handled flexibly by XTRACTIS to maintain data integrity.

The dataset included 12 vessels with 15 winding layers each, totaling 180 reference cases. This limited size posed challenges for robust model training and generalization [10] [11] [12]. Additionally, only summary statistics (minimum, maximum, average) per winding layer were available from the original time-series data, restricting feature richness. To address these constraints, the dataset was split into 153 training (TrD)/validation (VD) cases and 27 external test (ETD) cases. The modeling process used a rigorous cross-validation involving 100 cycles (20 × 5-fold splits, 80% for training, 20% for validation) to ensure robust assessment of descriptive and predictive performances and reliable predictive rules on unseen data in a realistic external scenario.

Each induction strategy (IS) induces, from TrD ∪ VD, a College of Virtual Experts (CVE2) composed of 100 XTRACTIS unitary models (Individual Virtual Experts - IVE). The decisions of the IVEs are aggregated through 3 different aggregations operators.

2,000 induction strategies (IS) are competitively and evolutionarily explored, generating a total of 6,000 CVE2. The top-performing CVE2 was selected, the one maximizing the predictive performance (measured on VD) and remaining close to the descriptive performance (measured on TrD).

This top-CVE2 was then used to generate ~20,000 synthetic data points based on predictions around, but distinct from, the 153 original training points. The goal is to achieve transparent reverse-engineering of the top-CVE2 through single-split cross validation, thanks to the large number of synthetic cases: 67% for TrD and 33% for VD.

From this extended dataset, 2,000 IS were explored to induce 2,000 IVEs that reproduces the robust decision strategy of the top-CVE2. The top-IVE was selected: the one maximizing the predictive performance (on VD), remaining close to the descriptive performance (on TrD), and being the most intelligible.

The top-IVE's real performance is finally assessed using the ETD.

This robust and transparent modeling approach enables clear insights into how manufacturing parameters influence porosity formation, supporting quality control and process optimization.

3. Results

Given the distribution of the target variable, XTRACTIS was employed to develop a regression model predicting the log10-transformed number of porosities. After the reverse engineering process, the best IVE was selected based on RMSE, and compared to random prediction (see Table 1).

Table 1: *Performance of the XTRACTIS IVE: log10(Number of Porosities)*.

log10 (number of porosities)	**Correlation**	**MAE**	**RMSE**	**Refusal**
Descriptive Performance / Training (2,000is. 67%)	0.997	0.02 (0.53%)	0.02 (0.78%)	0 (0.00%)
Predictive Performance / Validation (2,000is. 33%)	0.997	0.02 (0.55%)	0.03 (0.86%)	0 (0.00%)
Quality of CVE2 Copy / 153 Original Points	0.898	0.17 (5.65%)	0.24 (7.88%)	0 (0.00%)
Real Performance / External Test	0.824	0.20 (6.45%)	**0.25 (7.94%)**	0 (0.00%)

DOI: https://doi.org/10.26799/cp-polymers-composites-3Bsmaterials-2025

Performance against chance to beat / External Test P-Value = 0.001 (among 100,000 random permutations)	*0.585*	*0.28 (8.93%)*	*0.37 (11.89%)*	

The real performance on ETD is good: an RMSE of 7.94% and a correlation of 0.824. The intelligibility of the model is good, with a score of 3.52/5: the IVE retained only 15 truly useful predictors and uses 54 conjunctive rules, aggregated into 26 disjunctive rules, with an average of 4.8 predictors per rule. The intelligibility score of a predictive model, regardless of the generation technique used, is presented, for example, in Annex 1 of [13].

For benchmarking, a Boosted Tree CVE2 and then a Boosted Tree IVE were also developed following the same process and from exactly the same splits of data. BT IVE achieved slightly improved real performance on the ETD: RMSE of 7.02% and correlation of 0.872. However, this model was totally opaque due to its complexity (Intelligibility Score = 0.00/5), encompassing 2,289 rules (chain of 116 trees) and keeping the 58 predictors, unable to achieve both goals simultaneously: predictive accuracy and model transparency.

One of XTRACTIS' major strengths lies in the intelligibility of the induced rules. For example, the following rules illustrate how the model predicts the number of porosities with great clarity and simplicity (the values are bounded by the minimum and maximum of the variation range of each variable).

Expression of rule **R9** (3rd most contributory rule, with -32.49% relative change in model performance on TrD ∪ VD if removed):

If the max value of **Bobbin 'a' Tension** is less than approximately 73 N
And the average value of **Liner rotation speed** is less than approximately 540 tr/m
And **Winding layer volume** is approximately between 750,000 and 766,000 mm^3
And the average value of "**Doctor blade" angle** is approximately 19.71°
Then the number of porosities in the reservoir layer is **low** ($10^{2.36} = 229$).

Expression of Rule **R52** (14th most contributory rule, with -11.67% relative change on performance if removed):

If the maximum value of the **Liner rotation speed** is less than approximately 61 tr/m
And the minimum value of **Bobbin 'b' Tension** is less than approximately 5.5 N
And the **Winding angle** is less than approximately 18.1°
Then the number of porosities in the reservoir layer is **high** ($10^{3.69} = 4{,}898$).

Expression of Rule **R21** (18th most contributory rule, with -9.46% relative change on performance if removed):

If the minimum value of **Bobbin 'b' Tension** is higher than approximately 8 N
And the minimum value of **Bobbin 'c' Tension** is approximately between 0 and 0.2 N
And the **Layer volume** is higher than approximately 1.24 10^6 mm^3
Then the number of porosities in the reservoir layer is **medium** ($10^{3.04} = 1{,}096$ porosities).

Here, Bobbin 'a', 'b', and 'c' represent distinct carbon fiber bobbins, each corresponding to a different source of fibers. This differentiation allows the model to capture specific effects and variations in tension linked to individual bobbins, which influence porosity formation in the vessel layer.

4. Discussion and conclusion

XTRACTIS effectively balances predictive accuracy and model interpretability when analyzing porosity formation process, despite a limited dataset. The regression model predicting log-transformed porosity counts demonstrated strong generalization capacity (correlation 0.824, RMSE 7.94% on ETD), using only 15 selected predictors (process parameters) and composed of concise rules set, achieving an intelligibility score of 3.52/5.

DOI: https://doi.org/10.26799/cp-polymers-composites-3Bsmaterials-2025

The fuzzy IF…THE rules automatically extracted from the learning dataset support our hypothesis that porosity is mainly governed by interactions between fiber tension (across different bobbins), mandrel rotation speed, winding angle, and resin volume control. The importance of some of these aspects has been highlighted in certain studies, notably, the importance of tension in achieving densification and mechanical properties of the composite [14], uniform and controlled tension improves compaction that can reduce voids. Mandrel speed and winding angle affect fiber arrangement, with low values promoting defects [15]. Precise resin volume control by the doctor blade ensures consistent and homogeneous impregnation, preventing both dry zones and resin-rich areas that can trap air bubbles [16] [17].

This study confirms the great value of robust and transparent AI methods such as XTRACTIS General Reasoning AI (GRAI) in complex industrial contexts where accuracy, process understanding, and explainability of decisions are essential. Beyond prediction, the rule-based approach makes it possible to identify process inconsistencies and guide data and sensor improvements (corrective induction). It also provides explicit numerical thresholds for key process variables, allowing direct translation into actionable setpoints for production. Since our decision process is classified as high risk by the European AI Act (risk of explosion following a hydrogen leak), starting in 2026, it will be necessary to use a robust and intelligible predictive model as proposed by GRAI. Future work will focus on enriching the dataset, extracting more informative features, and confirming missing data to further improve the model's robustness.

Acknowledgements

This project is carried out in cooperation with OPmobility.

References

[1] M. Ravichandran et al, *Recent developments in Polymer Matrix Composites – A review*. IOP Conference Series: Materials Science and Engineering, 988(1), 012096, 2020.

[2] B. Patamaprohm, *Conception et durabilité de réservoirs en composites destinés au stockage de l'hydrogène,* Ecole Nationale Supérieure des Mines de Paris, 2014.

[3] M. Azeem et al, *Application of Filament Winding Technology in Composite Pressure Vessels and Challenges: A Review*, Journal of Energy Storage, 2022.

[4] S. Srebrenkoska et al, *Effect of Process Parameters on Thermal and Mechanical Properties of Filament Wound Polymer-Based Composite Pipes*, 2023.

[5] B. Meemary, *etudes expérimentales et analyse numérique de l'endommagement de composites thermoplastiques fabriqués par enroulement filamentaire et intégrant des fibres optiques,* 2024.

[6] W. Qi et al, *Prediction of void growth and fiber volume fraction based on filament winding process mechanics*, 2020.

[7] K. Lasn et M. Mulelid, *The effect of processing on the microstructure of hoop-wound composite cylinders*. Journal of Composite Materials, 54(26), 3981-3997, 2020.

[8] Z. Zalila, *Contribution à une théorie des Relations Floues d'ordre N.* Thèse de Doctorat en Contrôle des Systèmes/Mathématiques, D 573, Université de Technologie de Compiègne, Compiègne, France, 474 p, Mars 1993.

[9] Z. Zalila, *Essay | Your Artificial Intelligence, Connectionism or Augmented Fuzzy Cognitivism?*, INTELLITECH [intelligent technologies], v1.4, Compiègne, France, 26p, https://xtractis.ai/white-papers/, September 2017.

[10] A. Kumar et al, *A review on unbalanced data classification*. In Proceedings of International Joint Conference on Advances in Computational Intelligence: IJCACI 2021,pp. 197–208. Springer, 2022.

[11] H. Haibo et E. A. Garcia, *Learning from imbalanced data*. IEEE Transactions on knowledge and engineering 21(9), 1263–1284, 2009.

[12] L. Wang et al, *Review of classification methods on unbalanced data sets*. Ieee Access 9, 64606–64628, 2021.

[13] Z. Zalila, Intellitech & Xtractis, *XTRACTIS® the General Reasoning AI for Trusted Decisions. Use Case #29 | Naval Security: Identification of Underwater Sounds (Virtual Golden Ear) – Benchmark vs. Logistic Regression, Random Forest, Boosted Tree & Neural Network*. INTELLITECH [intelligent technologies], v1.1, 6p. https://xtractis.ai/use-cases/, Compiegne, France, November 2024.

[14] A. Blachut et al, *Influence of fiber tension during filament winding on the mechanical properties of composite pressure vessels*. Composite structures, vol. 304, p. 116337, 2023.

[15] S. Guclu et al, *A process for shape optimization of filament wound pressure vessels*. In : 11th AIAA/ISSMO Multidisciplinary Analysis and Optimization Conference. 2006. p. 6931.

[16] A. Agah-Tehrani et T. Hong, *A Model for Wet Filament Winding of Composite Cylinders with Arbitrary Thickness*, 1991.

[17] J. Alms et al, *Qualification of the Vitrimeric Matrices in Industrial-Scale Wet Filament Winding Processes for Type-4 Pressure Vessels*. Polymers, 2025, vol. 17, no 9, p. 1146.

Proceedings of the Polymers, Composites, 3BsMaterials 2025 Joint International Conferences
AlBufeira, Portugal – April 16 – 18, 2025
DOI: https://doi.org/10.26799/cp-polymers-composites-3Bsmaterials-2025

Optimizing Recycling: Fragmentation and Sorting of GFRP Components in Battery Housings - Impact on Recyclate Properties

Julius Eik Grimmenstein[1], Laura Hunger[1], Paul Schulz[2], Thomas Krampitz[1], Holger Lieberwirth[1]

[1]Technische Universität Bergakademie Freiberg, Institute for Processing Machines and Recycling Systems Technology, Lampadiusstraße 4, Freiberg, Germany, julius-eik.grimmenstein@iart.tu-freiberg.de
[2]Technische Universität Dresden, Institute of Lightweight Engineering and Polymer Technology, Holbeinstraße 3 Dresden, Germany, paul.schulz@tu-dresden.de

Abstract
The transition to e-mobility and renewable energy sources has significantly increased the demand for batteries in electric vehicles, which in turn has created a growing need for durable and lightweight battery housings. This has driven the demand for (glass) fibre-reinforced plastic components. Manufacturing virgin plastics and glass fibres is an energy-intensive process, contributing to high CO2 emissions, which can be mitigated by integrating recycled plastics to align with the goals of the European Green Deal for climate neutrality by 2050. This study investigates the efficacy of physical and mechanical recycling strategies for glass fibre-reinforced plastic (PP-GF, PA-GF), focusing on the direct shredding of a whole battery housing. The impact of these processes on the mechanical properties of recycled materials was also assessed. Findings reveal that direct shredding efficiently breaks down composite materials, facilitating high-purity separation of metal and polymer fractions with minimal waste, thus optimizing resource recovery. However, the separation of varying glass fibre contents remains a technical challenge requiring further research. Mechanical degradation caused by shredding was found to be within acceptable limits, ensuring the recycled polymers retain sufficient integrity for reuse in battery housings. These results underscore the potential of recycled polymers to reduce primary raw material consumption and energy use, advancing sustainable manufacturing practices in e-mobility and supporting a resource-efficient circular economy.
Keywords: glass fibres, recycling, polymers, composites, GFRP

1. Introduction

The global transition toward sustainable mobility is accelerating as nations strive to meet ambitious climate targets [1]. Against this backdrop, e-mobility has emerged as a cornerstone of decarbonization efforts, driven by both regulatory mandates and growing consumer demand. Between 2014 and 2023, the adoption of electric vehicles (EVs) has surged dramatically, reflecting a paradigm shift in transportation systems [2]. This trend is particularly evident in China, where policymakers have set a clear trajectory: by 2035, over half of all new passenger vehicles are projected to be fully battery-electric, with an additional 45% operating as plug-in hybrids [2]. Such ambitions underscore the critical role of e-mobility in achieving global sustainability goals.

Parallel to these advancements, national markets worldwide are witnessing a steady rise in the share of electric vehicles on roads, further cementing their position as a mainstream transportation solution [3]. However, this rapid growth also presents new challenges, particularly in the manufacturing and lifecycle management of EV components. One such component is the battery housing, a critical structural element that must balance performance, weight, and safety. Glass-fibre-reinforced thermoplastics (GFRP) have gained prominence in this context due to their exceptional mechanical properties, including high strength-to-weight ratios and corrosion resistance, making them ideal for battery enclosures [4,5].

As the demand for EVs continues to climb, the production of GFRP-based battery housings is expected to expand exponentially. Projections indicate that by 2030, approximately 30 million EV batteries will be in circulation in the EU [6]. This surge in deployment inevitably leads to a corresponding increase in GFRP materials entering the waste stream, raising urgent questions about their end-of-life management. The imperative to recycle these materials—while preserving their technical and environmental benefits—has thus become a focal point for researchers and

DOI: https://doi.org/10.26799/cp-polymers-composites-3Bsmaterials-2025

industry stakeholders alike. This study addresses these challenges by examining innovative recycling strategies for GFRP in battery housings, aiming to bridge the gap between technological progress and sustainable resource management.

This study examines the complete first life cycle and the beginning of a second life cycle of battery housings from Kautex Textron made from glass fibre-reinforced polypropylene (PP-GF) and polyamide 6 (PA6-GF). Components and test specimens were produced using injection moulding (IM) and compression moulding (CM). To simulate the utilisation phase, the materials underwent artificial aging according to the PV1200 cyclic climate change test.

Within the framework of the project, two recycling approaches were investigated: mechanical recycling and solvent-based (physical) recycling, with a focus on PP-GF. The process flow, shown in Figure 1, includes manufacturing, aging, recycling, and reprocessing using the same technologies, representing a closed-loop system. Mechanical recycling was performed by Vecoplan AG, while physical recycling of compression-moulded PP-GF was carried out by the Fraunhofer IVV to recover the polymer by separating it from the glass fibres.

The CM test specimens were recycled by means of physical recycling and the IM test specimens by means of mechanical recycling. The recycled material was reprocessed with varying recyclate contents (60–100%) and compared to virgin material. The primary aim is to evaluate how different recyclate proportions affect the mechanical properties and potential reusability of PP-GF in battery housing applications.

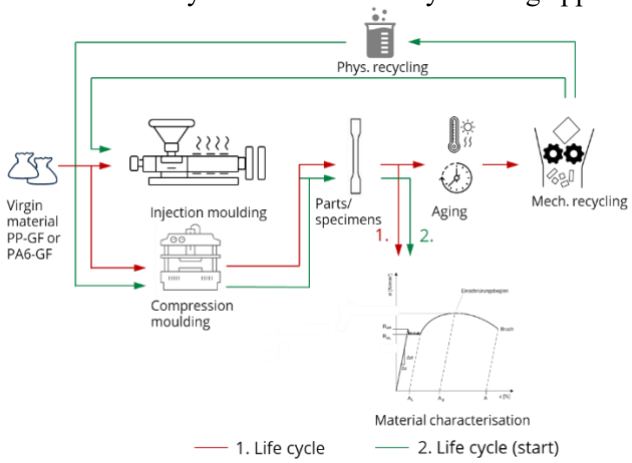

Fig 1.: Schematic illustration of the process routes and recycling paths in the project Gabriela

2. Experimental materials and setup

2.1. Test materials for shredding/sorting and testing mechaniscal properties

The experimental material investigated in this study consists of a completely shredded new battery housing from Kautex Textron GmbH & Co. KG measuring approximately 1430 x 1430 mm (Fig. 1). The battery housing, weighing roughly 95 kg in total, was composed of multiple material groups. It featured an aluminium cladding with a wall thickness of 5 mm and had a total height of 140 mm. For structural reinforcement and mounting, the housing incorporated steel inlets with a diameter of 40 mm and a length of up to 120 mm.

Fig. 2: Battery housing from Kautex Textron GmbH & Co. KG examined in the present study

DOI: https://doi.org/10.26799/cp-polymers-composites-3Bsmaterials-2025

Due to confidentiality constraints, precise weight distributions of individual materials cannot be disclosed. However, the primary material categories were identified as metals and polymers. The metallic components primarily included aluminium, which formed the outer casing of the battery pack (as shown in Fig. 1) and internal shielding parts, while steel was limited to fasteners such as screws, spacers, nuts, and connecting elements. The polymer components comprised polypropylene (PP) and polyamide (PA), with varying glass fiber contents ranging from 15% to 60%. Additionally, the assembly incorporated organic sheets, plastic connectors, and Elastomer adhesive for bonding components. This complex material composition underscores the challenges associated with recycling and material recovery in post-shredding battery waste management.

For testing the mechanical properties of the virgin PP-GF (PP-virgin) and the recycled PP-GF (rPP) plates in the dimension of 420 x 420 x 3 mm (IM) with a fiber volume content of 40 % (long GF) and 400 mm x 800 x 4 mm (CM) with a fiber volume content of 50 % (short GF) were manufactured by Kautex Textron GmbH & Co. KG using virgin material and recycled material. The test specimens were prepared by milling and removed from the test plates. The tensile tests were performed using multipurpose test specimens type A, for the other mechanical tests strip specimens with a dimension of 80 x 10 mm were used. All specimens were conditioned to the standard climate for at least 24 hours.

2.2 Experimental setup for shredding/sorting and tests of mechanical properties

Shredding and Sorting

The battery casings underwent a two-stage shredding process, each followed by a separate sorting step. The initial shredding was carried out using a single-shaft shredder from Vecoplan AG. This shredder was equipped with a torque drive rated at 180 kW, featuring a vibration damper and a covered discharge chute. The rotor was fitted with V-shaped cutting crowns, with cutting elements measuring 60 mm. The machine operated with a screen opening of 50 mm.

In the first sorting step, a sample was manually sorted to analyse the particle size distribution of individual material components. This step aimed to assess the suitability of separation through screening classification. Subsequently, a second sample was processed by a specialized service provider using a drum magnetic separator and an eddy current separator, both from Trennso-Technik. This two-stage separation targeted fractions greater than 16 mm and those between 4–16 mm, successfully isolating ferrous metals, aluminium, and polymer fractions. Particles smaller than 4 mm were deemed unsuitable for the recycling process and were therefore considered residue, destined for downcycling applications.

Following this step, the polymer fractions were further processed using near-infrared (NIR) and mid-infrared (MIR) spectroscopy to enable the separation of individual polymer types. This spectroscopic identification supports the effective downstream recycling of sorted polymer groups.

Due to the presence of composite materials with firmly bonded plastics and metals, and based on the initial results, a second shredding stage was conducted. This was performed using the same shredding machine, but with a reduced screen size of 16 mm. The same sorting procedures were applied afterward to further enhance material separation and recovery efficiency.

Tests of mechanical properties

Tensile tests, impact bending tests and bending tests were carried out to analyze the mechanical properties of the virgin material and the recycled material. Tensile tests were performed in accordance to the DIN EN ISO 527-2 (IM) and 527-4 (CM) standard, on a Z50 universal testing machine from the manufacturer Zwick-Roell. The test speed was set to 60 mm/min. The strain was recorded using a video extensometer. The bending tests were performed on a Zwick-Roell Z2.5 in accordance with the DIN EN ISO 178 standard. The test speed of 60 mm/min was the same as for the tensile test. The strain was recorded using a video extensometer. Impact bending tests were

DOI: https://doi.org/10.26799/cp-polymers-composites-3Bsmaterials-2025

performed in accordance with the DIN EN ISO standard 179-1. An impact pendulum maschine Zwick-Roell 5113 was used for the tests with non-instrumented measurement.

3. Results

3.1 Shredding and sorting tests

As previously mentioned, the sample was initially separated at 16 mm for technical reasons and to assess whether particle size influences the degree of material liberation. This classification resulted in two main fractions: the coarse fraction (>16 mm), amounting to 46.8 kg, and the fine fraction (4–16 mm), totaling 48.3 kg—thus, approximately equal in mass.

Material below 4 mm was discarded from further analysis, as it was deemed too fine for subsequent processing in injection moulding. This fraction amounted to 2.7 kg and is considered process-related loss.

Following the initial separation, both the coarse and fine fractions were manually sorted. This allowed for the creation of a particle size distribution profile for each individual component, including battery housing components, aluminium (Al), iron (Fe), glass-fibre reinforced plastic (GFRP), and other composite materials. The aim was to assess the feasibility of mechanical separation via screen classification (see Fig. 3).

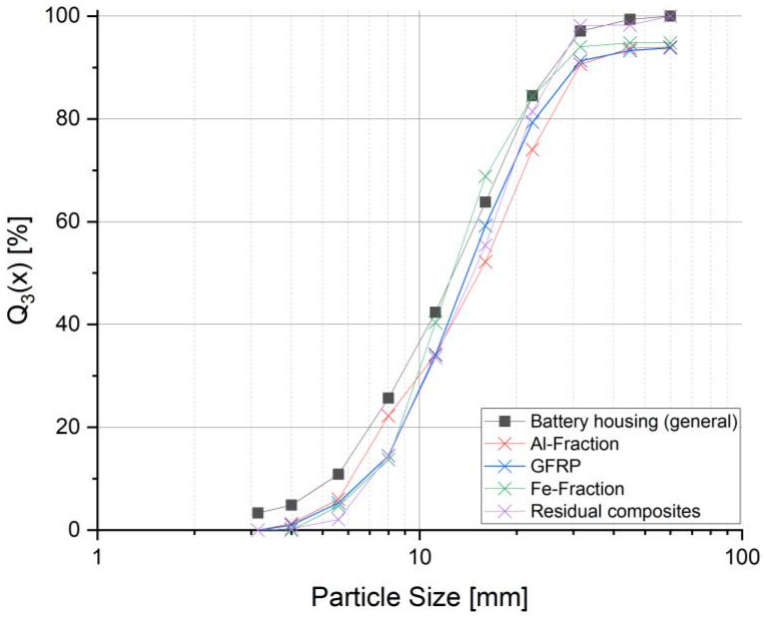

Fig. 3: Particle size distribution of the shredded battery housing and its components

The resulting particle size distribution revealed significant overlap between the particle size classes of the different material groups. This indicates that a separation based solely on screening would be ineffective, as the constituents are too similar in size.

Consequently, both the coarse (>16 mm) and fine (4–16 mm) fractions were subjected to further separation using a magnetic drum separator (for ferrous metal separation) and an eddy current separator (for non-ferrous metals such as Al). This was intended to improve the degree of separation of the metallic fractions.

The separation results for the coarse fraction showed that 68.7% of the aluminium content could be successfully separated, while 19.5% of the remaining fraction still consisted of non-liberated composite materials. Furthermore, 43% of the ferrous metal was extracted, with 56.7% residual composites remaining (see Fig. 4 top).

DOI: https://doi.org/10.26799/cp-polymers-composites-3Bsmaterials-2025

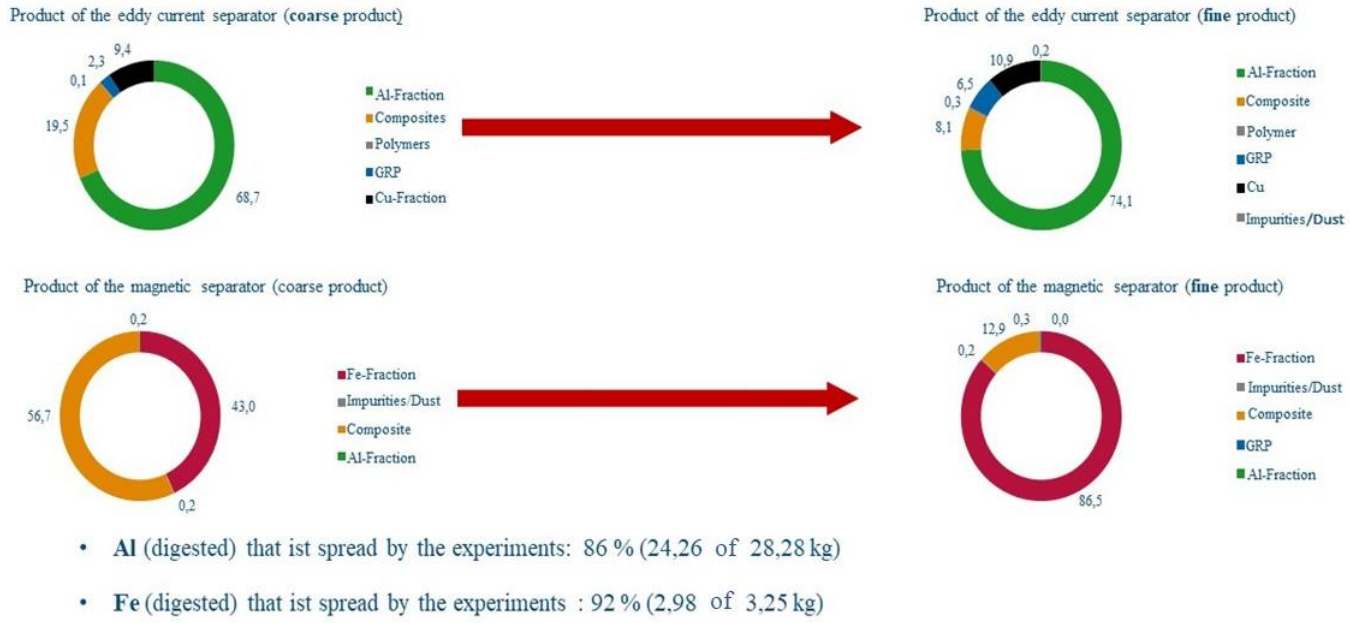

Fig. 4: Results of eddy current and magnetic separation in the size classes > 16 mm (top) and 4–16 mm (bottom)

Subsequently, the fine fraction (4–16 mm) was processed in the same manner. In this case, the eddy current separator showed an even higher efficiency. The residual content of composites was reduced to 8.6%, while the aluminium recovery rate increased to 74.1%. In addition, the copper recovery improved from 9.4% to 10.9% (see Fig. 4, bottom).
A similar pattern was observed for magnetic separation. The residual composite content dropped significantly from 56.7% to 12.9%, indicating an improved degree of liberation through particle size reduction.
Fig. 5 presents a material composition analysis across the different particle size classes. The analysis clearly shows that the proportion of composite residues decreases with decreasing particle size. This trend confirms that the mechanical liberation of materials improves as particle sizes are reduced.

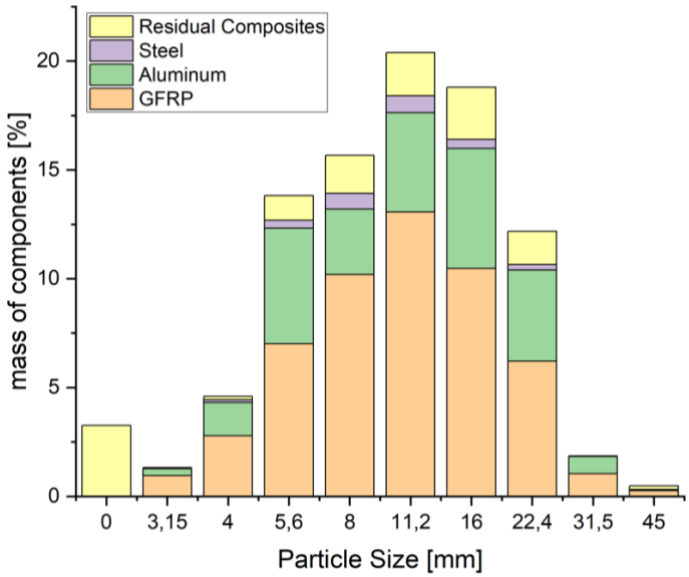

Fig. 5: Mass distribution of the individual components in the various particle size classes

DOI: https://doi.org/10.26799/cp-polymers-composites-3Bsmaterials-2025

As a result of the separation processes, 2.98 kg of the initially present 3.25 kg of iron were successfully recovered—representing a separation efficiency of approximately 92%. Similarly, 86% of the total aluminium content was separated from the mixed material stream (Fig 4).

3.2 Mechanical properties

In Fig. 6 are shown selected properties of the results of the material characterization. The virgin material is the reference for the comparison. The properties of the mixtures are shown in relation to the virgin material. Für the PP-LGF40 manufactured by IM a uniform decrease in properties can be recognised. Basically, it can be stated that the material degradation for the rPP with a proportion of 60 % recycled material is between 5-10 %. In comparison to that, the degradation for the rPP, which is made entirely from recycled material, is of 10-15 %. The situation is different for PP-GF50, which was processed by CM. No uniform trend can be recognised there. In some cases, the material properties have even improved compared to rPP (e.g., for the impact strength or the bending stiffness). Overall, it can be stated for the PP-GF50 processed by IM that no significant degradation can be detected at a recyclate content of 70 %. For the same material with a recyclate content of 100 % a limited degradation can be detected mainly in the single-digit range.

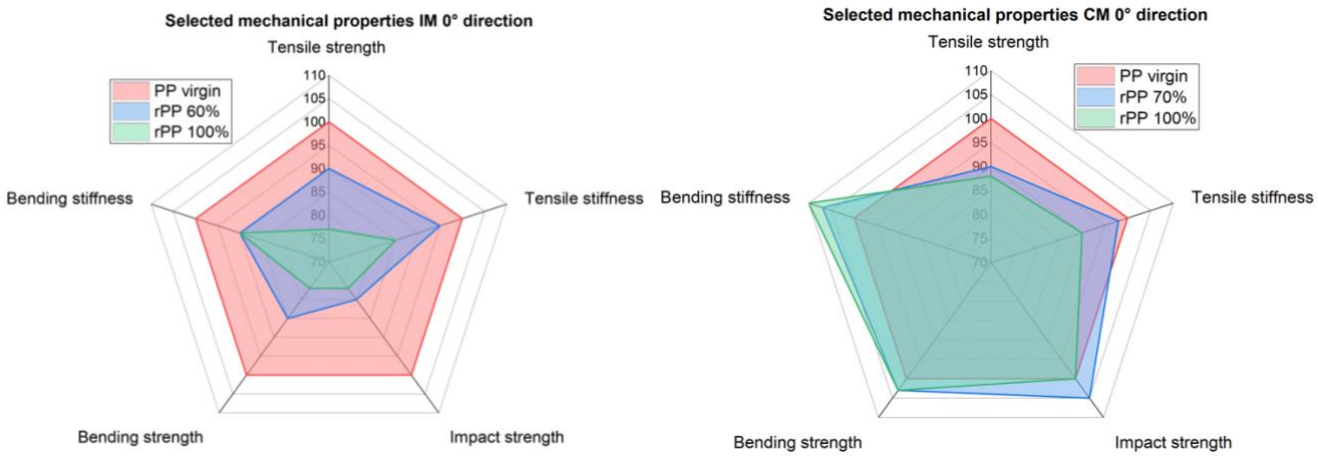

Fig. 6: Results of the mechanical tests compared to the virgin material for injection moulding (IM) and compression moulding (CM) for the 0° direction

4. Conclusion

The objective of this study was to assess whether mechanical size reduction is sufficient to enable the effective separation of battery housings into distinct metal and plastic fractions, and whether these fractions can in turn be separated into pure material streams.

The findings show that screening alone is not a viable method for component separation, as the particle size distributions of the various materials exhibit significant overlap. However, the combination of magnetic and eddy current separation delivered promising results. Across all samples, up to 90% of the total metal content could be successfully recovered. Specifically, the two-stage magnetic separation process enabled a recovery of 92% of the iron fraction, while the eddy current separator achieved 88% recovery of aluminium. In addition, a highly pure plastic fraction could be obtained.

As a next step, near-infrared (NIR) and mid-infrared (MIR) spectroscopy methods are being investigated in order to further sort the plastic fraction by polymer type. This would allow for improved recyclate purity and suitability for reprocessing.

Regarding the mechanical properties, it can be summarised that a degradation of the properties is to be expected with injection-moulded PP-GF recycle material. This degradation is likely due to fibre shortening and alterations

DOI: https://doi.org/10.26799/cp-polymers-composites-3Bsmaterials-2025

in the polymer structure, such as chain scission. Additionally, it cannot be excluded that changes in fibre orientation due to modified flow conditions contribute to the reduction in mechanical performance.
In contrast, PP-GF processed via compression moulding and subjected to physical recycling shows no clear trend of mechanical property loss. The addition of fresh glass fibres during reprocessing seems to help maintain performance levels, and the polymer structure of PP seems to remain largely intact through this method. However, to draw conclusive statements, further investigation is needed—particularly with respect to fibre length distribution, fibre-matrix adhesion, and polymer chain integrity.

Acknowledgements
The authors would like to thank the Federal Ministry for Economic Affairs and Climate Action (BMWK) and the Projektträger Jülich (PtJ) for the funding and support of the project. Special thanks also go to all project partners for their valuable cooperation and contributions throughout the course of the work.

References
[1] STATISTA, "Pkw-Neuzulassungen - nach Antrieb in der EU 2021," Statista [online], Sep. 8, 2022. [Accessed: May 22, 2025]. Available: https://de.statista.com/statistik/daten/studie/1251950/umfrage/pkw-neuzulassungen-in-der-eu-nach-antrieb/
[2] STATISTA, "Anteil der Antriebsarten beim Pkw-Absatz in China bis 2035," Statista [online], Sep. 9, 2022. [Accessed: May 22, 2025]. Available: https://de.statista.com/statistik/daten/studie/820984/umfrage/prognose-der-antriebsverteilung-in-der-chinesischen-automobilproduktion/
[3] STATISTA, "Elektromobilität – Statistiken und Daten," Statista [online]. [Accessed: May 21, 2025]. Available: https://de.statista.com/themen/608/elektromobilitaet/#topicOverview
[4] European Commission, "Communication from the Commission to the European Parliament, the European Council, the Council, the European Economic and Social Committee and the Committee of the Regions: The European Green Deal," 2019.
[5] T. Ghosh, H. C. Kim, R. De Kleine, T. J. Wallington, and B. R. Bakshi, "Life cycle energy and greenhouse gas emissions implications of using carbon fiber reinforced polymers in automotive components: Front subframe case study," Sustainable Materials and Technologies, vol. 28, e00263, 2021, doi: 10.1016/j.susmat.2021.e00263.
[6] Reuters, "EU's 2050 net zero goals at risk as EV rollout faces setbacks," *Reuters*, May 22, 2024. [Online]. Available: https://www.reuters.com/business/autos-transportation/eus-2050-net-zero-goals-risk-ev-rollout-faces-setbacks-2024-04-22/

Proceedings of the Polymers, Composites, 3BsMaterials 2025 Joint International Conferences
AlBufeira, Portugal – April 16 – 18, 2025
DOI: https://doi.org/10.26799/cp-polymers-composites-3Bsmaterials-2025

Driving Sustainability in the Automotive Industry: Hybrid Yarns for Thermoplastic Biocomposites

C. Oliveira[1], I. Costa[1], S. Silva[2], M. Silva[2], F. Oliveira[1]
[1]Department of Technology and Engineering, CITEVE (Technology Centre for Textile and Clothing Industry of Portugal), Vila Nova de Famalicão, Portugal.
[2]Functional Fibers Department, CeNTI (Centre for Nanotechnology and Smart Materials), Vila Nova de Famalicão, Portugal.

Abstract

Sustainability is boosting the research and development of new raw materials from renewable sources, and processes with a lower environmental impact for different industrial sectors, revealing the growing paradigm shift towards "more environmentally friendly" products. Following this strategy, have been growing interest on the concept of combining natural and bio-polymeric fiber materials in hybrid yarns, using a wide range of technologies such as conventional spinning, core-spinning, wrap-spinning, commingling process, twisting yarns, amongst others. Every technique allows for a different structural organization of the fibers in the cross section of the yarn, allowing the development of solutions that can be tailored to meet specific needs in terms of fiber distribution or reinforcement content. Fabric structures produced with hybrid yarns provide also numerous advantages in the production process, allowing for an easier impregnation of the reinforcement fibers, as well as more potential to obtain parts with complex 3D geometries. Hybrid yarns represent intermediate solutions for thermoplastic biocomposites. These can be woven or arranged into fabrics or UD structures for further utilization in thermoforming processes and production of biocomposites after a detailed characterization of the structural and functional properties of the biocomposites. In this work, two different yarn production methods are used to obtain hybrid yarns based on a cellulosic reinforcement fiber (lyocell) and three biopolymeric fibers (Bio-PE, Bio-PA and PLA). Detail will be given on the different arrangements of reinforcement and matrix fibers in the inner structure of the yarn as well as some mechanical characterization of the yarns and their potential to be used as solutions in the biocomposites and automotive industry.

Keywords: hybrid yarns, biocomposites, biopolymers, natural fibers

1. Introduction

The shift towards the use of more sustainable materials and the adoption of more sustainable practices has been increasing across a large range of areas such as the automotive field or the composite and biocomposite industries. Adopting natural and biobased materials for fiber based composite components in the automotive area has been increasingly seen as a viable alternative to several applications as it reduces the reliance on synthetic materials and lessens the environmental impact of the final products. Combining the use of these materials with the concept of hybrid yarns, one can achieve natural and bio-based hybrid structures for use in composite applications. Hybrid yarns, and the textile structures that originate from them can effectively be tailored to improve polymer impregnation, reduce production costs, and improve properties of composite parts [1].
The development of hybrid yarns involves the blending of fibers with dissimilar properties and can be obtained by a wide range of techniques, such as commingling [2], ring-spinning [3], core-spinning [4], Friction (DREF) spinning [5], wrap-spinning6] , amongst others. In literature, the combination of natural and synthetic fibers for production of natural based hybrid yarns generally focuses on techniques such as DREF spinning or core spinning [1], however conventional ring-spinning is a technique that has not been reported for this purpose and has the potential to promote a good dispersion and distribution of both fibers in the yarn, with positive implications in the impregnation potential of thermoplastic processing techniques.

DOI: https://doi.org/10.26799/cp-polymers-composites-3Bsmaterials-2025

The properties of hybrid yarns are influenced by the production process, the combination of different fibers and filaments, and their organization within the yarn. Ring spinning, due to its versatility and cost-effectiveness, is commonly used for producing both monomaterial and hybrid yarns. In this method, raw fibers are stretched, twisted, and wound continuously to create yarns from short staple fibers, applying different levels of stretch and twist to create the desired linear density and mechanical properties. On the other hand, hybrid yarns produced using a core-spun system, use a core filament, typically a thermoplastic polymer, around which the staple fibers will be spun. This process involves adding an additional creel to support the core filament and precise guiding devices to ensure proper positioning.

This work aims at presenting new possibilities for natural based hybrid yarn production destined for applications in biocomposite industry.

2. Materials and Methods

2.1 Materials

The core spun yarns were manufactured using continuous filaments of the biopolymers PLA (570 dtex), Bio-PA (255 dtex), and Bio-PE (250 dtex), supplied by POLISILK, Sofila SAS, and Braskem, respectively. Biopolymeric materials were chosen due to their bio-based origin and common use in automotive applications. As reinforcement, lyocell fibres with a nominal length of 38 mm and a fineness of 1.3 dtex, were used as a natural fiber reinforcement due to their mechanical properties and durability provided to the yarns and fabrics. For the spun yarns, the same lyocell fibres were blended with PLA, Bio-PA and Bio-PE short fibres with lengths between 35 and 45 mm.

2.2. Methods

2.2.1. Manufacture of hybrid yarns

In this study, two types of yarn structures were produced to compare the influence of fibre composition and spinning technique on processability and mechanical performance of hybrid yarns. Conventional ring-spun yarns were prepared using a 50:50 weight ratio of lyocell and biopolymer fibres, specifically Lyocell/PLA, Lyocell/Bio-PA, and Lyocell/Bio-PE blends. All ring-spun yarns were produced with a nominal linear density of Ne 6 (approximately 100 tex) on a laboratory-scale ring spinning line. Additionally, hybrid yarns were produced using a core-spun configuration, in which lyocell fibres formed the sheath around continuous filaments of PLA, Bio-PA, or Bio-PE. These yarns were also manufactured using a ring spinning system adapted for core-spinning, maintaining the same lyocell/biopolymer combinations as the conventional yarns. This approach aimed to evaluate the suitability of different biopolymer materials and spinning methods in terms of both process efficiency and mechanical performance. The consistent use of lyocell as the reinforcing fibre across all yarn types enabled a focused comparison of the behaviour of the matrix materials (PLA, Bio-PA, Bio-PE) under varying structural configurations.

2.2.3. Characterisation and Testing

The tenacity, elongation at break, and breaking force of the yarns were measured using a Textechno Statimat M automatic tensile testing system. A pretension of 0.5 cN/tex was applied, with a test speed of 100 mm/min. All measurements were carried out in accordance with NP EN ISO 2062:2009. Prior to testing, all specimens were conditioned for 24 hours under standard atmospheric conditions (20 °C and 65% relative humidity) and tested under the same conditions.

To conduct a preliminary morphological evaluation of the hybrid yarns, a Leica Emspira 3 stereoscopic magnifier was employed at 100× and 200x magnification. This method allowed for the visual assessment of fibre distribution, alignment, and surface characteristics within the yarn cross-section. These initial observations are essential for supporting the optimisation of spinning parameters and serve as a foundation for more detailed structural analyses by optical and electron microscopy, which will enable a deeper understanding of the yarn morphology and material composition.

3. Results and discussion

The conventional spinning process was used for the production of several hybrid yarns based in cellulosic reinforcement fibers (lyocell) and biopolymeric fibers (Bio-PE, Bio-PA and PLA). Spinning process requires the fibers to comply with parameters like length, elongation, crimping, etc. Bio-PE fibers presented high elongation and variation in fibre diameter, while PA fibers were excessively long and presented electrostatic properties that

DOI: https://doi.org/10.26799/cp-polymers-composites-3Bsmaterials-2025

hindered the processability throughout the spinning process. PLA and lyocell fibers presented an optimal behaviour for application in spinning processes.

Cross section images of the spun and core-spun hybrid yarns are depicted in Fig. 1, while Table 1 indicates the average linear density of the produced yarns.

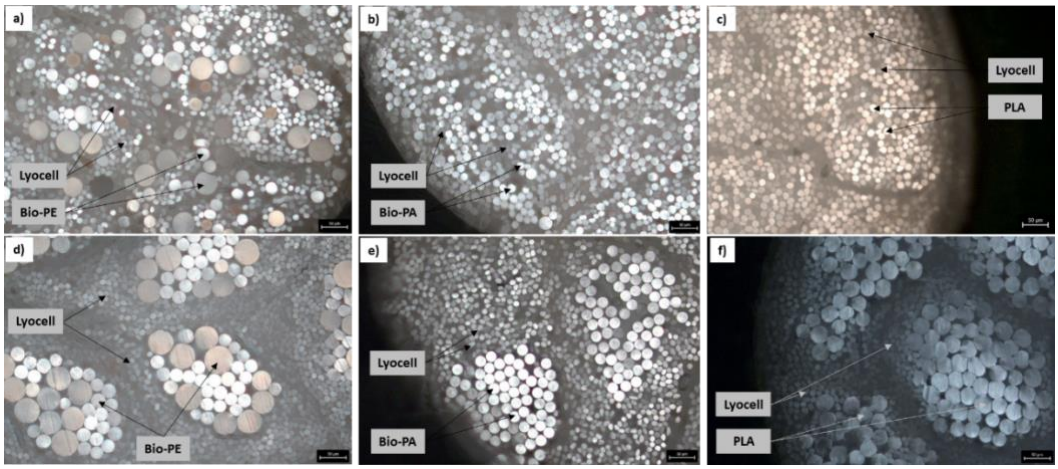

Fig. 1 – Cross section images of hybrid yarns: a)Lyocell/Bio-PE spun yarn; b)Lyocell/Bio-PA spun yarn; c)Lyocell/PLA spun yarn; d)Lyocell/Bio-PE core-spun yarn; e)Lyocell/Bio-PA core-spun yarn; f)Lyocell/PLA core-spun yarn. (scalebar on the figures represents a length of 50µm)

Table 1 - Linear density of spun and core-spun hybrid yarns developed

Spun Yarns			Core-Spun Yarns		
Lyocell/Bio-PE	Lyocell/Bio-PA	Lyocell/PLA	Lyocell/Bio-PE	Lyocell/Bio-PA	Lyocell/PLA
11,1 tex	12,1 tex	9,1 tex	10,8 tex	8,3 tex	9,8 tex

Spun yarns show a homogeneous distribution of reinforcement and matrix fibers in the cross section of the yarn (figure 1 a), b) and c)), which is characteristic of the spinning process, given the fibers are mixed in the first stage of the process, before the carding step, which promotes a good dispersion and distribution across the yarn. For the case of core-spun yarns, the biopolymeric fibers were used as the core material, while the spinning of the reinforcement fibers occurred around the matrix yarn. As seen in figures 1d), 1e) and 1f), the core material was completely covered with the spun reinforcement fibers.

Since the hybrid yarns produced in this work will be used in the production of textile structures for direct application in composite processing techniques, as they integrate both reinforcement and matrix materials, their different yarn structures may give rise to different kinds of impregnation of the textile structure during the composite processing method. Just like commingled yarns spun yarns present a good fiber distribution throughout the whole cross section of the yarn, therefore, the melting and impregnation of reinforcement fibers can be more homogeneous, as it is widely reported in literature for commingled yarns. [7] As for core-spun yarns, the melting of the biopolymers tend to happen in the core of the yarn with some impregnation of the reinforcement fibers in its surface.

As seen from the analysis of the mechanical properties of the hybrid yarns, present in figure 2, Bio-PE based yarns show the highest values of elongation, due to the elastic nature of the raw fibers used in the spinning process, combined with the applied drawing conditions. Lyocell/Bio-PA core-spun yarn presented the better mechanical properties amongst the several yarns tested.

DOI: https://doi.org/10.26799/cp-polymers-composites-3Bsmaterials-2025

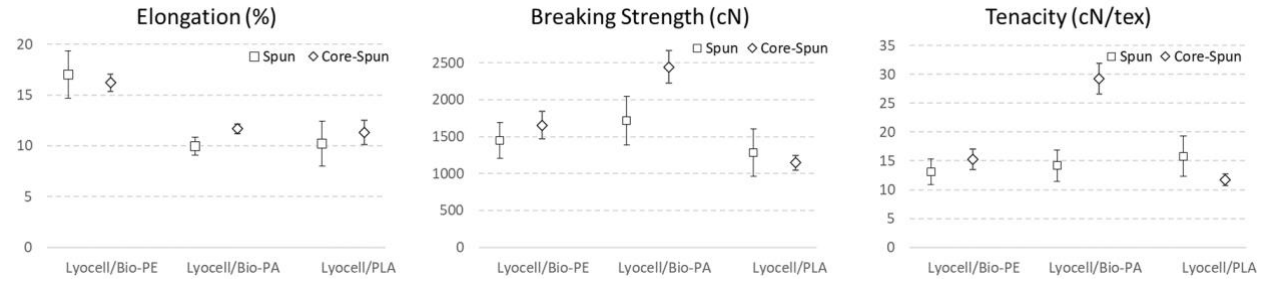

Fig. 2 – Elongation, Breaking Strength and Tenacity of hybrid yarns

As may be concluded from the results, different yarn structures and biopolymeric fibers offer different advantages and drawbacks in terms of processability, mechanical properties and ecological profile, as all biopolymeric fibers show sustainable credentials to be used in the biocomposites field.

4. Conclusion

In summation, while some may provide better processability in conventional spinning process (PLA), the mechanical properties shall be analysed knowing that dry yarns may present different properties than those of composite materials after processing. Although some variations may arise from the use of different matrix fibers or yarn structures, hybrid yarns obtained by conventional spinning processes represent a promising approach for application in biocomposite materials, as an efficient method to promote an intimate mixture between matrix and reinforcement fibers, combining both materials at the yarn level, and allowing the possibility to produce pre-impregnated structures by weaving the hybrid yarns into a textile structure for further processing by thermoforming or other composite production methods.

Acknowledgements

This work was supported by the integrated project be@t – Textile Bioeconomy (TC-C12-i01, Sustainable Bioeconomy No. 02/C12-i01.01/2022), promoted by the Recovery and Resilience Plan (RRP), Next Generation EU, for the period 2021 – 2026.

References

1. Ferreira N, Rodrigues L, Silva S, et al. Hybrid yarn structures as a promising approach for thermoplastic biocomposites. Journal of Composite Materials. 2024;58(30):3171-3196.
2. Hussain M, Abbas A, Asghar MA. Commingling technique for thermoplastic composites. In: Natural fibers to composites: process, properties, structures. Cham: Springer International Publishing, 2022, pp. 79–93.
3. Yin R, Ling Y, Fisher R, et al. Viable approaches to increase the throughput of ring spinning: a critical review. J Clean Prod 2021; 323: 129116.
4. Uddin MB, Nath AD, Sowrov K, et al. Fabrication and characterization of jute-covered core-spun yarn produced on flyer-spinning frame. Text Leather Rev 2022; 5: 414–429.
5. Bar M, Das A, Alagirusamy R. Effect of interface on composites made from DREF spun hybrid yarn with low twisted core flax yarn. Compos Appl Sci Manuf 2018; 107: 260–270.
6. Suryavanshi V. Comparative analysis of winding of multiple yarns on automated winding machine. J Phys Conf 2024; 2763(1).
7. Bernet, N., Michaud, V., Bourban, P. E., & Månson, J. A. Commingled yarn composites for rapid processing of complex shapes. Composites Part A: Applied Science and Manufacturing, 2001; 32(11): 1613-1626.

Proceedings of the Polymers, Composites, 3BsMaterials 2025 Joint International Conferences
AlBufeira, Portugal – April 16 – 18, 2025
DOI: https://doi.org/10.26799/cp-polymers-composites-3Bsmaterials-2025

Segmentation Aware Attention Mechanism for Defect Classification of both Virgin and Recycled Carbon Fiber Fabric

Abhiram Kolli, Denis Krajnc, Christian Eitzinger
Profactor GmbH
Im Stadtgut D1, Steyr-Gleink, Austria, {akolli, dkrajn, ceitzi}@profactor.at

Abstract

Using neural networks for photometric stereo based surface inspection is fast emerging, especially for carbon fiber matrix (before binding with resins) / fabric. However, the non-rigid nature and high reflectivity of the carbon fiber material makes them very difficult to perform robust digital image-based quality inspection. To overcome this issue, 1). a dataset was collected with photometric stereo feature modalities and open sourced, 2). studied the classification performance on the dataset and 3). propose a segmentation supervised multi-head defect classification model. Several standard vision classifier models are retrained on the created dataset to benchmark the performance of our model. This paper demonstrates that a segmentation supervised multi-head neural network outperforms the benchmark. The realized classifier model achieves over 30% higher accuracy compared to standard CNNs and transformer models. The dataset for classification and its parser is available at https://zenodo.org/records/11203952.

Keywords: Carbon fiber**,** quality inspection, defect classification, defect segmentation, photometric stereo

1. Introduction and Related Work

Traditional models struggle to classify carbon fiber defects due to their non-rigid nature, requiring extensive resources and failing to achieve high accuracy. This study introduces a more efficient neural network with fewer parameters, optimizing real-time feature extraction and improving defect classification for industrial applications.

Several works have explored both supervised and unsupervised carbon fiber defect identification, as discussed in paper [1]. Supervised approaches train neural networks with diverse defect samples, often using augmentation to improve classification accuracy. Common methods include direct classification and image segmentation, with models like ResNet, U-Net, and DenseNet121 applied for feature extraction. Synthetic data generation and explainable AI techniques combining CNNs with support vector machines have been explored, along with object detection methods like YOLOv5. However, these techniques require extensive training samples and continuous retraining to accommodate new defect patterns.

In contrast, unsupervised defect identification eliminates the need for predefined defect samples, addressing challenges in defect modeling, generalization, and sample collection. Various methods have been proposed, including vision transformers with normalizing flow models, Siamese networks for segmentation, and autoencoder-based anomaly detection. While these models achieve higher accuracy with fewer training samples, they also tend to generate more false positives compared to supervised approaches.

2. Methodology

2.1. Dataset

The dataset was created using an in-house photometric stereo sensor [2] with a resolution of 40–60 µm and a 50×50 mm field of view. The onboard computer extracts key feature modalities—azimuthal, diffuse, fiber refractivity, polar, and specular (see Fig. 1) from raw images to analyze carbon fiber orientation and defects. The dataset consists of carbon fibers materials such as non-crimp fabric (NCF) from virgin, recycled, and woven fabric.

DOI: https://doi.org/10.26799/cp-polymers-composites-3Bsmaterials-2025

Industry experts identified defects such as gaps, missing stitches, and fuzzballs, resulting in a dataset of 190 samples: 99 gaps, 37 missing stitches, and 54 fuzzballs. Each image measures 1080×1200×5 in dimension.

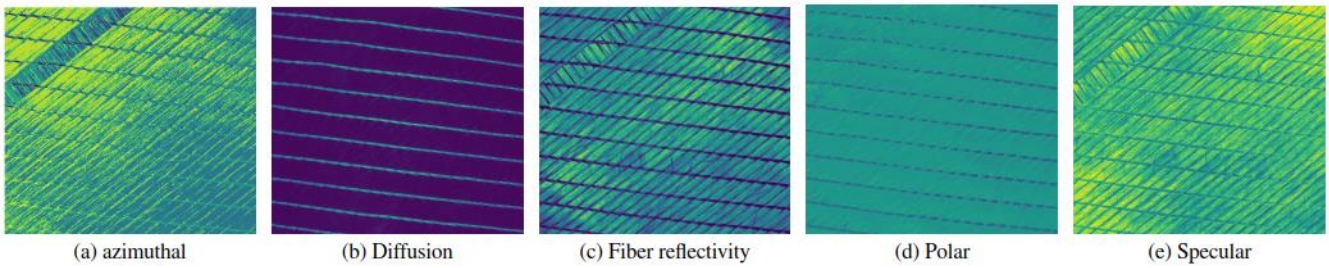

Fig. 1: Illustration of all the 5 input feature modalities pre-computed using photometric stereo.

Both classification and segmentation datasets were developed from the above collected dataset. Classification assigns a single defect label per image, potentially biasing the network toward dominant defect classes. To mitigate this, a manually segmented binary mask was created, marking defect regions as 1 and clean areas as 0. These annotated datasets validate the designed neural network's performance.

To optimize performance, the model employs a hybrid loss function combining cross-entropy, SSIM, and IoU losses to enhance segmentation accuracy. The classification dataset was evaluated using K-fold cross-validation, while segmentation performance was measured using mean square error. Training was conducted with TensorFlow and Keras, utilizing an Nvidia V100 GPU for efficient processing.

2.2. Architecture

The network follows a single-input, multi-head architecture with an input batch of 32×512×512×5, where 5 feature modalities are processed (see Fig. 2). Two convolutional branches handle the input—one processes it into patches, reshaping it to 32×64×64×320, while the other maintains the original dimensions. The segmentation output is obtained through alpha blending between classifier embeddings and segmentation masks, with α=0.5.

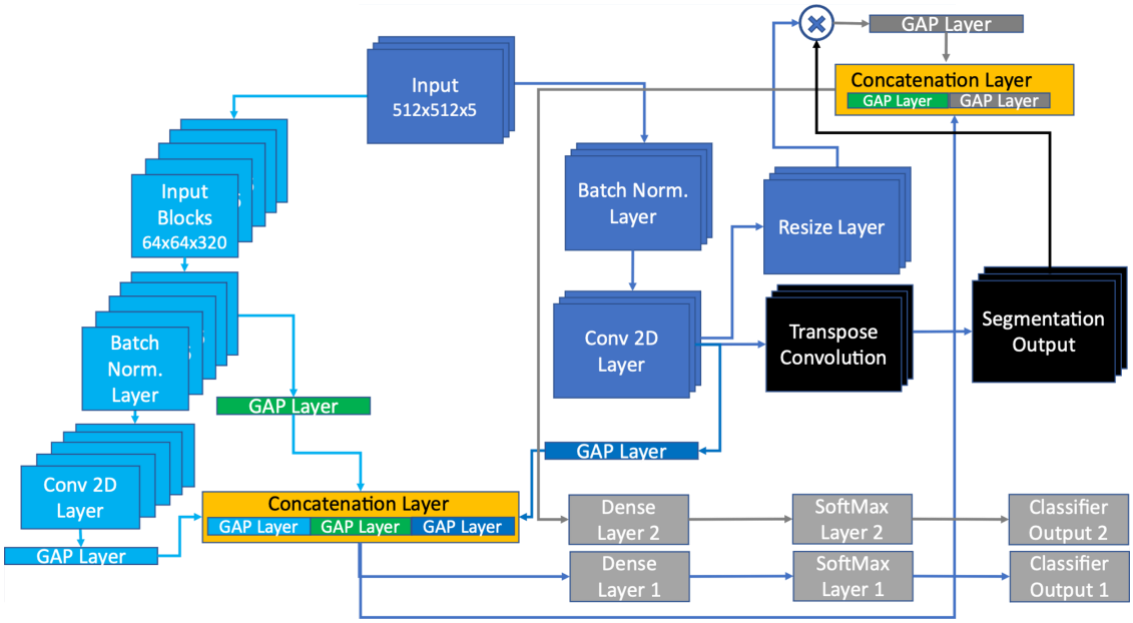

Fig. 2: Proposed neural network architecture where the light blue blocks are the patch-based convolution blocks, dark blue blocks are the full convolutional filter, and the black blocks are segmentation related blocks. Each convolutional block's output is given to global average pooling, and the yellow blocks are the concatenation layers. This enables the feature diversity. The gray blocks are fully connected neural layers that belong to 2 classifier heads.

DOI: https://doi.org/10.26799/cp-polymers-composites-3Bsmaterials-2025

2.3. Loss functions

The model consists of two classification heads and one segmentation head, using cross-entropy loss for classification. Segmentation is trained with a hybrid loss combining BCE, SSIM, and IoU losses to improve boundary precision. BCE loss measures pixel-wise classification accuracy, SSIM loss integrates structural similarities, and IoU loss enhances correspondence between predicted and ground truth segmentation. Numerical stability is maintained using predefined constants.

2.4. Performance evaluations

To perform ML classification analysis with a limited sample count, the dataset was split into an 80-20% training-validation ratio. The study utilized a 100-fold (K-fold) cross-validation scheme, calculating mean accuracy across all folds. To assess classifier performance, the top-K accuracy metric was applied, evaluating whether the true class fell within the K highest probabilities of the model's output, thereby determining true positives.
Segmentation performance was measured using mean square error. All experiments were conducted using TensorFlow 2.15 and Keras libraries, running on an Nvidia V100 GPU (16GB VRAM). The training process employed Adam optimization with a learning rate of 0.001, a batch size of 16, and 200 training epochs, incorporating early stopping with a patience value of 20.

3. Results and Analysis

The evaluation of the designed networks were preformed through benchmarking with standard models such as the Xception, Inception, MobileNet-V2 and compact convolutional transformers (CCT). These networks were trained with the same data and through transfer learning.

Table 1. Performance benchmark of defect classification task.

Model	*Size*	*Parameters*	*Accuracy (%)*
Xception	88MB	22.9M	40.00
InceptionV3	92MB	23.9M	60.00
MobileNet V2	14MB	3.5M	40.00
Compact Convolutional Transformers†	2.68 MB	0.7M	42.00
CompactConvNet (ours)	143.64 KB	36,771	77.59

† one input channel used during training to avoid out of memory issues

Despite having a 5-channel input capability, models were trained with only 3 channels, limiting performance. The classifier-only model outperformed standard models, achieving 77.59% accuracy. However, its lower-than-expected performance was attributed to non-discriminative features, suboptimal hyperparameters, or noisy labels. Ablation studies tested various scenarios, including utilizing all 5 feature channels, modifying activation functions, altering block sizes and dilation rates, adjusting neuron counts, and applying label smoothing. None of these experiments improved accuracy beyond 82%, indicating the model's inherent constraints. To overcome the performance deficiency segmentation task was used as attention mechanism to the classifier as shown in Fig. 2.

Table 2. Mean accuracy for 100-fold cross-validation across different scenarios. "Seg." stands for segmentation included. "w/o ab" refers to results without alpha blending, whereas "w ab" denotes those with alpha blending applied.

Scenario	*Accuracy*
top-K Classifier Only	96.31
No top-K Classifier Only	82.19
Seg. + Classifier	92.36
Seg. + Classifier 2 w/o ab	95.02
Seg. + Classifier 2 w ab	95.52

Three segmentation and classification training scenarios were tested using the same architecture. The first trained segmentation and classification models jointly as a multi-task self-supervised network,

DOI: https://doi.org/10.26799/cp-polymers-composites-3Bsmaterials-2025

achieving 92.36% accuracy. The second used the segmented output mask as the classifier's region of interest, while the third combined segmentation masks with network embeddings via weighted summation.

While top-K classification was useful for analysis, it was impractical for defect identification. The segmentation task had a mean square error of 0.098. Refining alpha blending between raw input and binary masks improved visualization, aiding defect localization, performance validation, and correspondence between detected defects and input images.

This work has trained lite weight neural networks that are able to classify the defects without relying on data augmentation techniques. This is due to the varying range of values per channel obtained from the in house developed sensor. An optimized network architecture is developed to balance the higher performance and improved speed and lack of data. Such approach improved the performance of our network compared to standard network architectures (CNNs and transformer) by 37%. Ablation studies improved the understanding of the data distribution and labeling errors that are common in the real-world scenarios. Nevertheless, by additionally including the segmentation task, the model's accuracy improved from 77.79% to 92.36% (see Fig. 4, Classifier Output block). Thus segmented output region alone is further classified (see Fig. 2, Classifier Output 2 block) there by achieving 95.52%.

4. Conclusion

This paper identified the inherent issues with the data labelling method and data mislabelling on this open-sourced dataset. Furthermore, these issues were solved systematically through constructive hypothesis and proved through experimentation such as benchmarking with known models (CNNs, transformer), using random search based hyper parameter tuning, label smoothing, distribution of embeddings using top-K, introducing multi-task mechanism such as segmentation and attention mechanism that classifies the segmented embedding. These efforts improved the performance of the network by 10% (82.39% vs 95.52%), emphasizing the importance of data quality and the necessary strategies.

Acknowledgements

This research was conducted within the framework of MC4 and COMPASS projects.

The work presented in this paper is related to the project "MC4" and has received funding from the European Union's Horizon Europe research and innovation program under grant agreement No 101057394. Views and opinions expressed are however those of the author(s) only and do not necessarily reflect those of the European Union. Neither the European Union nor the granting authority can be held responsible for them.

COMPASS Project is co-funded by the European Commission within the Horizon Europe Programme Views, grant number 101136940, and opinions expressed are however those of the author(s) only and do not necessarily reflect those of the European Union. Neither the European Union nor the granting authority can be held responsible for them.

Co-funded by the European Union

References

1. A. Kolli, D. Krajnc and C. Eitzinger, "AI-based inspection of recycled carbon fibre fabric," in Society for the Advancement of Material and Process Engineering, Belfast, 2024.
2. Sebastian Zambal, Werner Palfinger, Matthias Stöger, and Christian Eitzinger. Accurate fibre orientation measurement for carbon fibre surfaces. Pattern Recognition, 48(11):3324–3332, 2015.

Proceedings of the Polymers, Composites, 3BsMaterials 2025 Joint International Conferences
AlBufeira, Portugal – April 16 – 18, 2025
DOI: https://doi.org/10.26799/cp-polymers-composites-3Bsmaterials-2025

Material characteristics of reused carbon fibre-reinforced polymers from wind turbine blades

Sönke Gerdes[1], Imke Möllmann[1], Christian Lauter[1]
[1]PHWT Research Institute, Department of Lightweight Design,
PHWT Private University of Applied Sciences, 49356 Diepholz, Germany, gerdes@phwt.de

Abstract

The total capacity of wind turbines has reached 250 GW in 2023. The increase during the last decade is about 13 GW per year in average. To meet the 2030 climate and energy targets these average must be raised up to 33 GW per year. Repowering wind turbines is becoming increasingly important to achieve this goal. The number of dismantled wind turbines will increase in the coming years as they reach the end of their service life (20-25 years) or are replaced by repowering wind turbines. About 8000 wind turbine blades (WTB) have been dismounted every year since 2021 in the USA and 3800 within the EU. Current solutions for disposing of WTBs is the incineration to generate thermal energy or disposal in a landfill. Industrial recycling is only possible by cut and shredd the WTBs to be used as filler material for fibre-reinforced concrete. Especially the reuse of fibre-reinforced polymers out of WTBs as construction elements is a challenging task due to the blade geometry but it enables the use of high-performance materials like carbon fibre reinforced polymers in other sectors. For many WTB, the available material data or insufficient is unknown, especially regarding the fiber-reinforced polymers used. Accordingly, statements regarding the mechanical properties of the recycled material can only be made to a limited extent. Therefore, the material characteristics of reused carbon fibre-reinforced polymers of the spar caps is focussed in this study. To evaluate the value of the used material the material properties as strength and stiffness, their has to be compared with virgin material. The material of the WTBs must be tested in accordance with applicable standards, to enable the comparison with given material data. Furthermore, the quality of manufacture must be taken into account and macroscopic and microscopic damage must be analysed especisally due to glass fibre layers which are incorporated into the laminate structure to facilitate resin flow during the vacuum infusion process. The analysis of these factors is crucial in order to demonstrate and optimise the reuse of carbon fibre reinforced polymers from wind turbine blades in new areas of application.

Keywords: Recycling, reuse, wind turbine blades, carbon fibre, material testing, life cycle

1. Introduction

Wind turbines are considered one of the driving technologies for the sustainable energy generation. In 2024, almost 40% of the total energy consumption in Europe was covered by sustainable energy sources, about 12% only by the usage of wind energy [1]. The long-term goal is to achieve 100% coverage with sustainable energy. In Addition to the renewable energy sources, the circular economy of the materials used in the manufacturing process of power plants is an important step towards 100% sustainability. The service life of wind turbines is typically limited to 20 years. Only considering the leading European countries – Germany, Denmark, Spain and the UK – more then 2000 wind turbines will be reaching the end of their service life every year over the next decade [2]. Due to the material mix out of fibre reinforced polymers with glass or carbon firbe reinforcement, polyurethane foam and wooden parts recycling of wind turbine blades is demanding. Therefore, the material ends up eventually in landfilling or incineration with a massive impact on the environment and is lost to the circular economy [3]. Wind turbine blades mainly fail due to incidentsil like surface damages due to collisions or lightning cracks. Main causes of structural cracks are failure of adhesive bonding. The good conditions of the FRPs after its service life offers potential for recycling [4]. In general there are already three ways of recycle fibre reinforced polymers, chemical recycling, thermal recycling and mechanical recycling. Chemical and thermal recycling methods pursue the target of separation of fibre and matrix to produce new products out of reused fibres. Disadvantage of the seperations methods is the high energy consumption [3]. The common method for mechanical recycling is cutting and shredding the composites and use the as filler

material for fibre reinforced concrete [3]. Another way to recycle composites is to cut beam or plate structures out of the wind turbine blade. In the following investigations, the mechanical properties of carbon fiber-reinforced polymer structures from wind turbine blades are analyzed in order to verify the mechanical equivalence with virgin material.

2. Experimental basis and methods

The cross section of wind turbine blades can be described in three main segments skin, shear webs and spar caps. The skin and the vertical shear webs are usually made out of glass fibre reinforced plastics with a foam or balsa wood core. To provide a high bending stiffness and strength carbon reinforced polymers (CFRP) are used for the the upper and lower spar caps [5]. This investigation focused on the consideration of the more valuable spar caps material. To prove the mechanical equivalence of the used material with virgin material it is necessary to carry out standardized analyses. Therefore a part of one spar cap is removed out of the wind turbine cross section cutted into nine segments along the width of the spar cap. The segments are then sliced into thin samples along the thickness of the spar cap (figure 1).

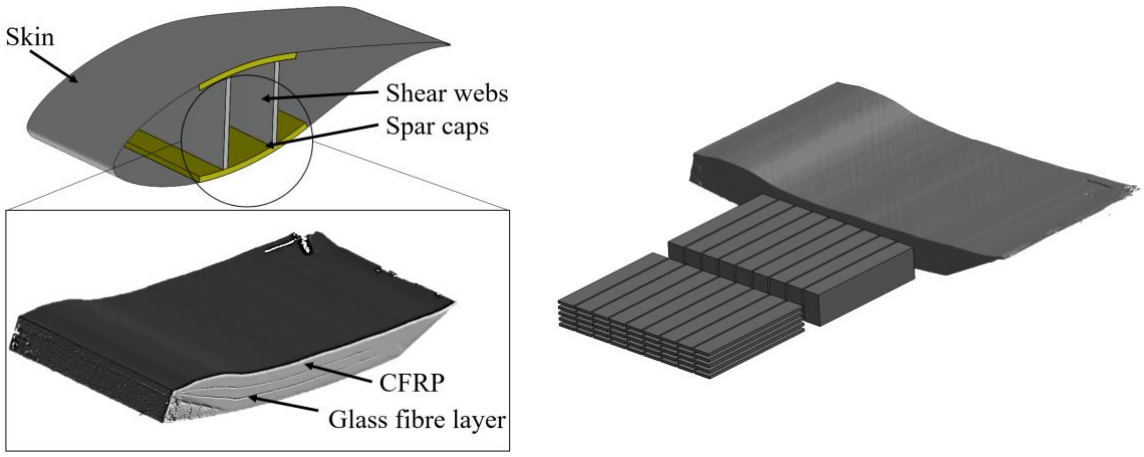

Figure 1: 3D scanned carbon spar cap and sample orientation

The segments with a length of 120 mm, a height of 20 mm and a width of 15 mm are analysed by computer tomography to consider the fibre alignment and to detect structural damages and defects. Afterwards thin samples are produced out of the segments for the mechanical testing. For the determination of the mechanical properties a four point bending test according to DIN EN ISO 14125 is chosen. This test provides the bending stiffness and the strength of the material. A sample size of 100x15x2 mm is required for testing [6]. Five samples are made out of each segment which means in total there are 45 samples along the spar cap cross section. In order to create constant surface conditions without defects or notches, the samples are adjusted to the correct thickness by milling, which could represent the actual production of semi finiched components like beams and plates by machining production.

3. Results and discussion

The computer tomography of each segment shows constant results along the width of the spar cap. The spar cap layout can be described in three recurring layers upper and lower skin, CFRP structure and flow aid (figure 2). The upper and lower skin is a glass fibre reinforced layer which was not included in the further investigations. The CFRP area is the load-carrying structure and consist of unidirectional oriented carbon fibre in direction of the length of the WTB. The flow aid is used during the production process by vacuum infusion to support the resin flow through the wind turbine blade.

DOI: https://doi.org/10.26799/cp-polymers-composites-3Bsmaterials-2025

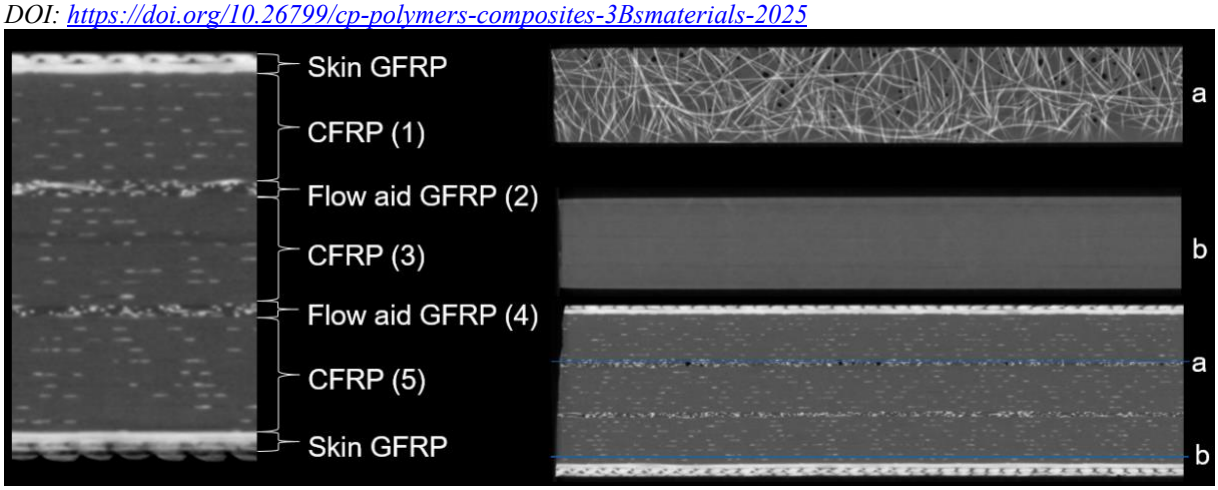

Figure 2: Computer tomography of the spar cap layout

The glass fibre fleece has a lower fibre volume content, which improves the resin flow compared to the dense carbon layer. Due to the high proportion of remaining resin, shrinkage cavities form within the flow aid as a result of volume contraction during curing. These shrinkage cavities can conly be found within both flow aids and upper and lower skin and not within the carbon structure (figure 3).

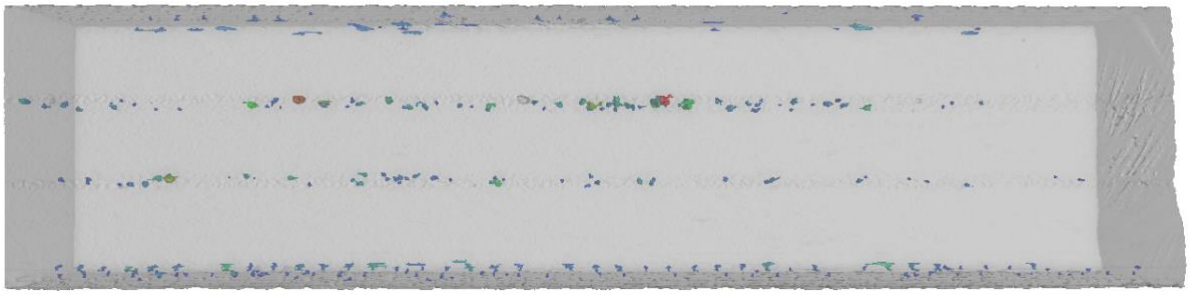

Figure 3: Cavity analysis of segment 2

This results must be taken into account for the sample preparation. Each layer, upper CFRP (1), middle CFRP (3), lower CFRP (5), upper flow aid (2) and lower flow aid (4) of each segment is tested separately. Due to the assumption that the glass fibre fleece negatively influences the mechanical properties, the flow aid with a thickness of about one millimeter is positioned in the center of the samples (2) and (4) to provide a comparable area moment of inertia for each segment and sample.

The results of the mechanical testing confirm this assumption. The tensile strength within the samples including the flow aid do not even reach half of the tensile strength of the pure carbon fibre reinforced polymere (figure 4). The Young's modulus also varies significantly between both areas.

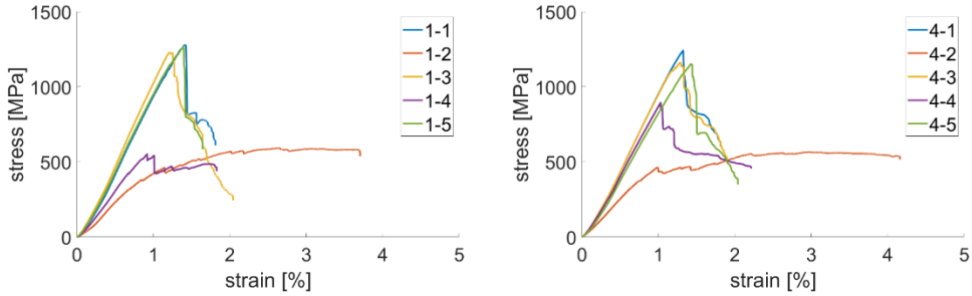

Figure 4: Stress-strain diagram of segment 1 (left) and segment 4 (right)

Considering the distribution of tensile strength over the entire cross section (figure 5). The areas above, between and below the flow aid show comparable values from 1200 to 1350 MPa. The samples within

the glass fibre fleece varies from 550 to 1000 MPa. Various reasons suspected for this large spread. On the one hand the tolerances of the centering of the flow aid while sample manufacturing, but also the amount and size of shrinkage cavities. The flow aid does not pass through the entire cross-section. This is the reason why segment 9 shows an even distribution of tensile strength.

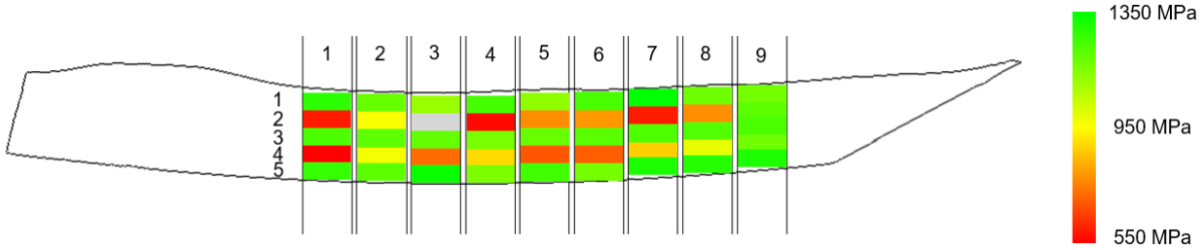

Figure 5: Tensile strength distribution over the spar cap cross section

4. Conclusion

A lot of composite material from wind tubine blades will have to be recycled in the upcoming years to creat a circular economy and further use is conceivable due to the good mechanical properties. The investigation shows that carbon fibre-reinforced polymers for wind turbine blades at the end of their service life can achieve with a young's modulus of 100 GPa and a tensile strength of more the 1200 MPa the same mechanical properties as virgin material. But a major challenge is still the given spar cap layout due to the geometry and the layer structure. New products can be separated from the spar cap by machining production but especially for thin structures as plates the position of the flow aids must be taken into account. Further investigations focusing on the influence of shrinkage cavities on the mechanical properties can contribute to the understanding of defects within the material.

Acknowledgements

This Project is supported by the Federal Ministry for Economic Affairs and Climate Action (BMWK) on the basis of a decision by the German Bundestag. The authors would like to thank the BMWK for the funding and Eurecum GmbH & Co. KG for supporting this research.

References

[1] Erneuerbare Energie - Europa, , n.d.. [Online]. Available: https://de.statista.com/outlook/io/energie/erneuerbare-energie/europa (last access 23.04.2025)

[2] Ziegler, L.; Gonzalez, E.; Rubert, T.; Smolka, U.; Melero, J.J. Lifetime extension of onshore wind turbines: A review covering Germany, Spain, Denmark, and the UK. Renew. Sustain. Energy Rev. 2018, 82, 1261–1271.

[3] Khalid, M., Arif, Z., Hossain, M., Umer, R., Recycling of wind turbine blades through modern recycling technologies: A road to zero waste, Renewable Energy Focus, 2023, 44, 373–389

[4] Mishnaevsky, L., Jr. Root Causes and Mechanisms of Failure of Wind Turbine Blades: Overview, Materials 2022, 15, 2959.

[5] Crespo, B. H., Damage Sensing Blades, MARE-WINT New Materials and Reliabity in Offshore Wind Turbine Technology, Springer Open, 2016, p. 26 - 52

[6] DIN EN ISO 14125. Fibre-reinforced plastic composites - Determination of flexural properties

Proceedings of the Polymers, Composites, 3BsMaterials 2025 Joint International Conferences
AlBufeira, Portugal – April 16 – 18, 2025
DOI: https://doi.org/10.26799/cp-polymers-composites-3Bsmaterials-2025

Determinaton of the Ageing State of Resin Systems in Wind Turbine Blades at the End of Lifetime with IR-Spectroscopy

Imke Möllmann[1], Sönke Gerdes[1], Alexander Brunnner[1], Christian Lauter[1]
[1] PHWT Research Institute, Department for Lightweight Design
PHWT Private University of Applied Sciences, Am Campus 2, 49356 Diepholz, Germany, moellmann@phwt.de

Abstract
The global expansion of renewable energy has led to a significant increase in installed wind turbine capacity, growing from 24 GW in 2001 to over 1,021 GW by 2023. As a result, the dismantling and recycling of end-of-life wind turbine blades has become an increasingly important topic. Given the complexity of these composite structures, and the limited knowledge about their exact composition, innovative approaches are needed to enable sustainable recycling. This paper presents a method to characterize the ageing state of resin systems used in wind turbine blades via infrared spectroscopy (IR). Blades from different turbines were analysed and compared to reference resin systems to identify ageing-related spectral shifts.

Keywords: fibre reinforced plastics, wind turbine rotorblades, recycling, IR-spectroscopy, ageing

1. Introduction

The rapid development and deployment of wind energy technology in recent decades has led to a significant increase in the number and scale of wind turbines worldwide. The installed power capacity has risen from 24 GW in 2001 to 1,021 GW in 2023. As turbine technology advances, older installations reach the end of their operational lifespan—typically around 20 to 25 years in Germany. This results in an increasing volume of wind turbine waste, particularly rotor blades, with estimates of up to 75,000 tons annually in Germany alone. Driven by climate policy and technical innovation, this expansion is accompanied by the growing challenge of sustainably managing wind turbine components at the end of their operational life cycle. Rotor blades, which are primarily made of fibre-reinforced polymer composites, represent a particular recycling challenge due to their size, material composition, and lack of standardized documentation on their manufacturing. [1, 2]
Current recycling methods for rotor blades include mechanical shredding, Figure 1, pyrolysis, chemical solvolysis, and thermal oxidation. While these approaches enable the partial recovery of materials such as glass or carbon fibres, they are often energy-intensive or yield products of relatively low economic value, such as filler material or fuels for the cement industry. Furthermore, direct reuse or high-value upcycling is hindered by a general lack of information on the material structure and its ageing condition. [2, 3]

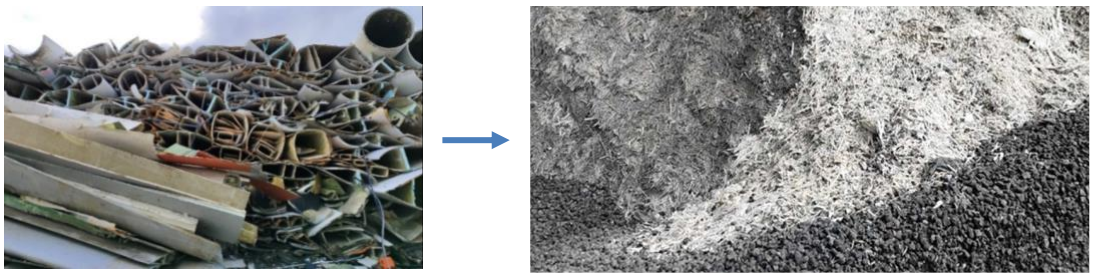

Fig. 1: Current recycling method mechanical shredding

Thus, characterising the ageing state of resin systems in wind turbine blades is essential for evaluating their reuse potential. The aim of the presented research is to develop a non-destructive and cost-effective methodology to characterise the resin systems used in rotor blades and to determine their ageing condition. This would support more intelligent recycling strategies, facilitate the reuse of composite elements, and ultimately contribute to a circular economy in wind energy.

DOI: https://doi.org/10.26799/cp-polymers-composites-3Bsmaterials-2025

2. Materials and Methods

To determine the ageing state of wind turbine blades after their service life, Attenuated Total Reflectance Fourier-Transform Infrared Spectroscopy (ATR-FTIR) was selected for the chemical analysis of used resin systems in the blade materials. ATR-IR spectroscopy is a surface-sensitive, non-destructive technique that allows rapid identification of polymeric materials with minimal preparation.

The objectives of the method were to determine the type of resin used in various blades, evaluate the ageing condition based on deviations from virgin reference spectra, build a comparative database for future materials assessment in comparison to fresh cured resin systems and define a standardised process to support reuse and recycling decisions. [4]

For the measurements, five samples each were taken from the root, shear web and tip, as shown in Figure 2, of the wind turbine blade and measured at four different surfaces using a Bruker Lumos spectroscopy system. To build up a database, additional spectra of cured and uncured reference resin systems were recorded. The spectral data were collected using an ATR accessory under controlled conditions and the recorded IR spectra were analysed, and similarities/differences to the database were assessed.

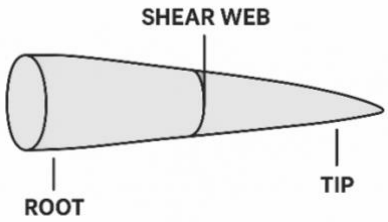

Fig. 2: Withdrawal positions

The process is part of a broader research strategy involving mechanical, chemical, and physical property analysis. For instance, mechanical testing includes interlaminar shear strength (DIN EN ISO 14130), fibre content (DIN 16459), and bending behaviour (DIN EN ISO 14125). [5, 6, 7]

3. Results and Discussion

For the determination of the used resin in the wind turbine blades first the three different sections were measured and analysed with the ATR-IR spectroscopy as shown in Figure 3. With this analysis, it was shown that the used resin system was based on epoxy resin in according to typical chemical groups, such as the epoxy unit at 900 cm^{-1} or the aldehyde groups at 2800 cm^{-1}.

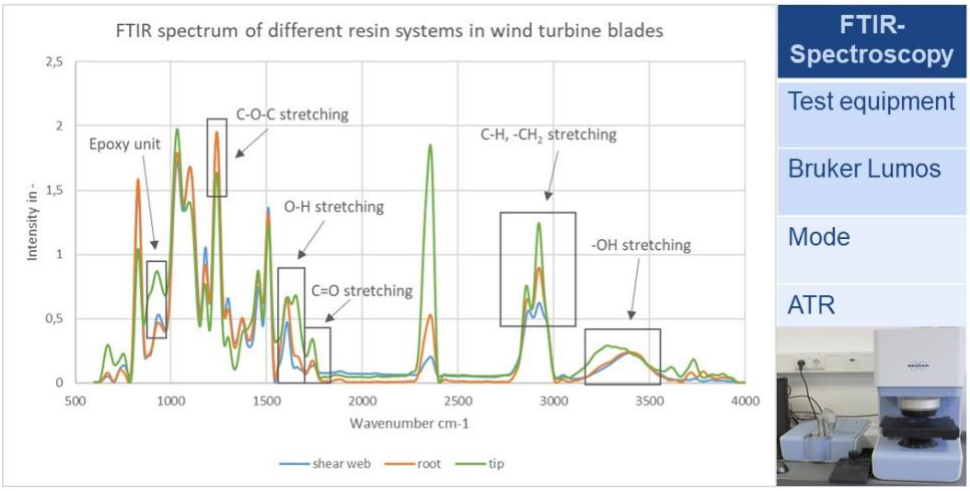

Fig. 3: Mean value of ATR-IR-spectra from resin system used in wind turbine blades at the shear web, root and tip assigned to chemical groups

DOI: https://doi.org/10.26799/cp-polymers-composites-3Bsmaterials-2025

The ATR-FTIR analysis provided comprehensive insights into the chemical composition and degradation behaviour of the resin systems, as illustrated in Figure 4. A direct spectral comparison between aged wind turbine blade materials and freshly cured epoxy reference samples revealed the presence of identical characteristic absorption peaks. Most notably, bands corresponding to the C–O–C ether stretching vibration at approximately 1115 cm^{-1} and C–H deformation vibrations near 1460 cm^{-1} were consistently observed across both sample types. These findings strongly support the conclusion that epoxy-based resin systems are employed as the primary matrix material in the rotor blades.
However, a closer inspection of the spectra indicated distinct variations in peak intensity and, in some cases, subtle shifts in band shape and width. These differences are attributed to alterations in the chemical environment caused by long-term exposure to environmental stressors. Such stressors include ultraviolet (UV) radiation, moisture ingress, oxygen diffusion, and thermal cycling — all of which are known to induce photooxidative degradation, hydrolysis, and chain scission processes within polymer matrices. The observed decrease in peak intensity, particularly for functional groups susceptible to oxidation or hydrolysis, points to molecular changes such as reduced crosslink density, loss of low-molecular-weight fragments, or the formation of oxidized species.
The sensitivity of the ATR-IR technique to these surface-level phenomena underscores its value as a diagnostic tool for evaluating material ageing and weathering effects in composite structures. Given that ATR-IR primarily probes the outer microns of the sample, it is especially well-suited to detecting degradation gradients that originate at the surface and propagate inward over time.
To enable broader applicability, the measurements were integrated into a central database of resin spectra, which supports identification and categorisation of resin types across different blade models and manufacturers.

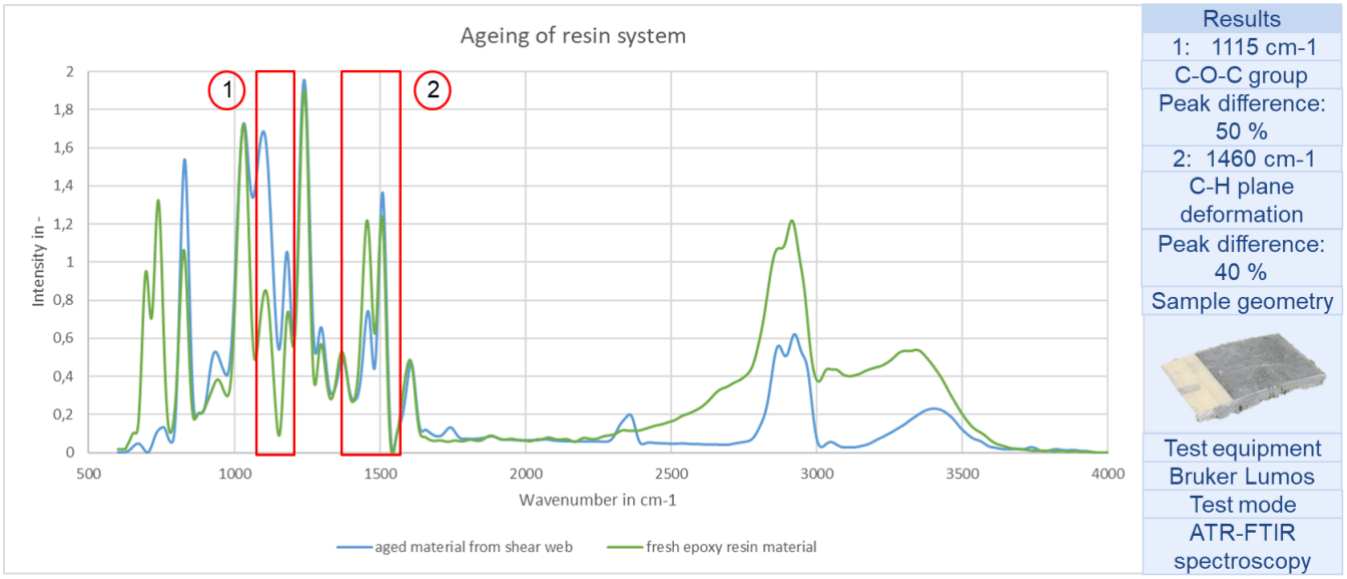

Fig. 4: Selection of IR-spectral-measurements of different resin systems for determining the aging state of wind turbine blade material

4. Conclusion

This study successfully demonstrates the suitability of ATR-IR spectroscopy for determining the ageing state of resin systems in wind turbine blades. The method's low sample preparation requirements and rapid execution of changes make it highly effective for post-service life analyses of large composite structures. However, the sensitivity of the measurement to the surfaces of the specimens must be taken into account when carrying out the measurement. The key results of the measurements are the reliable identification of resin types by spectral comparison, the detection of ageing effects such as oxidation and bond degradation in relation to the chemical

DOI: https://doi.org/10.26799/cp-polymers-composites-3Bsmaterials-2025

reactive groups in the resin systems, and the creation of a materials database to support recycling strategies and second-life assessments.

Further research will expand this methodology by correlating the spectroscopic findings with mechanical and environmental performance tests, such as interlaminar shear strength and climate resistance evaluations. This integrated approach will strengthen efforts to enable circular material use in the wind energy sector.

Acknowledgements

This Project is supported by the Federal Ministry for Economic Affairs and Climate Action (BMWK) on the basis of a decision by the German Bundestag. The authors would like to thank the BMWK for the funding and Eurecum GmbH & Co. KG for supporting this research.

References

1. M.Y. Khalid, Z.U. Arif, M. Hossain, R. Umer, “Recycling of wind turbine blades through modern recycling technologies: A road to zero waste”, in *Renewable Energy Focus*, 44, 2023, pp. 373-389.
2. L. Fernández, “Cumulative installed wind power capacity worldwide from 2001 to 2023 (in gigawatts)”, in: *GEWC – Global Wind Report 2024,* p. 148.
3. J. Chen, J. Wang, A. Ni, “Recycling and reuse of composite materials for wind turbine blades: An overview”, in: *Journal of Reinforced Plastics and Composites*, 38 (12), 2019, pp. 567 - 577.
4. G.M. Odegard, A. Bandyopadhyay, “Physical aging of epoxy polymers and their composites”, in: *Polymer Physics*, 49 (24), 2011, pp. 1695 - 1716.
5. DIN EN ISO 14130. Fibre reinforced plastic composites - Determination of apparent interlaminar shear strength by short beam-method
6. DIN 16459. Determination of the fiber volume content of fiber-reinforced plastics by thermogravimetric analysis (TGA)
7. DIN EN ISO 14125. Fibre-reinforced plastic composites - Determination of flexural properties

Proceedings of the Polymers, Composites, 3BsMaterials 2025 Joint International Conferences
AlBufeira, Portugal – April 16 – 18, 2025
DOI: https://doi.org/10.26799/cp-polymers-composites-3Bsmaterials-2025

Human Robot Collaborative Draping of Carbon Fibre Composite Parts: Results of Three Case Studies

D. Zielinski[1], C. Eitzinger[1], C. Frommel[2]
[1]Profactor GmbH
Im Stadtgut D1, 4407 Steyr-Gleink, Austria, dominik.zielinski@profactor.at, christian.eitzinger@profactor.at
[2]Deutsches Zentrum für Luft- und Raumfahrt e.V. (DLR)
Am Technologiezentrum 4, Augsburg, Germany, christoph.frommel@dlr.de

Abstract

Draping is a process where carbon or glass fibre fabric is placed in a 3D mould. This process requires high precision in terms of placement accuracy and quality. About 30% of all fibre-reinforced composites parts are made through draping and the vast majority is draped manually.

To increase the degree of automation and to use the synergies of humans and robots in this task, developments have been made to perform this task through human-robot collaboration. This will benefit from the higher precision of the robot and the high dexterity of the human operator, when draping areas with high curvature.

The developments were evaluated on three use cases coming from the aerospace, automotive and boat-building sector. A comparison is made between conventional (manual) draping and human-robot collaborative draping in terms of efficiency of the overall process. The analysis includes different modes of human-robot collaboration, ranging from co-existence in the same workspace to physical human-robot collaboration when jointly handling a piece of carbon fibre fabric. Also, different ways of user interaction with the robot through gestures and voice are analysed and the need for feedback to the user is highlighted.

Results indicate that human-robot collaboration has benefits for the draping of composite parts. Interaction modes need to be chosen carefully, to allow a natural interaction leading to a real improvement of efficiency. Safety certifications seem to be the most restricting aspect at the moment, as the lack of sufficiently intelligent safety devices does not allow efficient collaboration with large industrial robots.

Keywords: draping of composite parts, human-robot collaboration, human-robot interaction, productivity

1. Introduction

Carbon fibre reinforced composite parts have become increasingly critical due to their excellent mechanical properties, particularly in industries requiring lightweight and high-strength solutions. Various manufacturing technologies exist for these composite materials, among which draping plays a central role, accounting for approximately 30% of all fibre-reinforced composite parts produced today [1].

Draping involves the precise placement of two-dimensional fibre plies into three-dimensional moulds and is predominantly a manual task. Human operators remain essential due to their superior dexterity in adapting the flexible composite material precisely to complex three-dimensional shapes and influencing fibre orientation at critical features of the parts. However, purely manual draping processes often struggle with reproducibility, accuracy and the handling of large-scale fabric plies. These challenges typically lead to increased production costs and variability in the quality of the final products [2].

Human-robot collaboration (HRC) has emerged as a promising approach to address these challenges by leveraging complementary human and robotic capabilities. Within the context of draping, robotic systems can efficiently handle large fibre plies, providing consistency and precision in placement, while humans focus on complex features that remain difficult to automate.

This paper highlights practical implementations of HRC draping techniques, emphasizing results from industrially relevant case studies across multiple sectors.

DOI: https://doi.org/10.26799/cp-polymers-composites-3Bsmaterials-2025

2. Objectives and Methodology

The main objectives of these studies were to evaluate technical and economic feasibility of collaborative draping and to explore optimal modalities for human-robot interaction. Three industry-specific use cases from automotive, maritime and aerospace sectors provided diverse scenarios for testing the developed approaches. Draping tasks were performed by participants from real shop-floor environments, ensuring the evaluation was grounded in practical, real-world conditions. Each draping procedure was recorded and analysed in detail to capture insights on process efficiency, human-robot interactions and practical safety considerations.

To address certifiable safety, two distinct workcell approaches were tested. In the first, the cell and process were designed from the outset with possible safety certification. In contrast, the second approach intentionally exceeded standard safety boundaries to explore what adaptations might be possible in more flexible environments. In this case, safety was maintained by assigning an additional operator to supervise the workcell, with the authority to stop the process at any time.

3. Experimental Setup and Case Studies

Three distinct case studies were conducted, each reflecting unique industrial requirements and constraints. In the automotive sector, the draping process focused on a front hood using prepreg carbon fibre material. The primary challenge was achieving a pristine surface finish, which required precise handling and accurate placement of the material throughout the process. The maritime case study involved manufacturing of a large boat propeller using dry glass and carbon fibre fabric. The scale and flexibility of the plies introduced significant handling complexity, making human-robot collaboration essential for accurate positioning and stable draping. For the aerospace sector, the focus was on draping a structural rib composed of dry carbon fibre. The use case imposed stringent demands on fibre orientation and process documentation to ensure compliance with structural integrity demands. The long and flexible plies required careful manipulation and were transported using a synchronized robot-robot collaborative configuration.

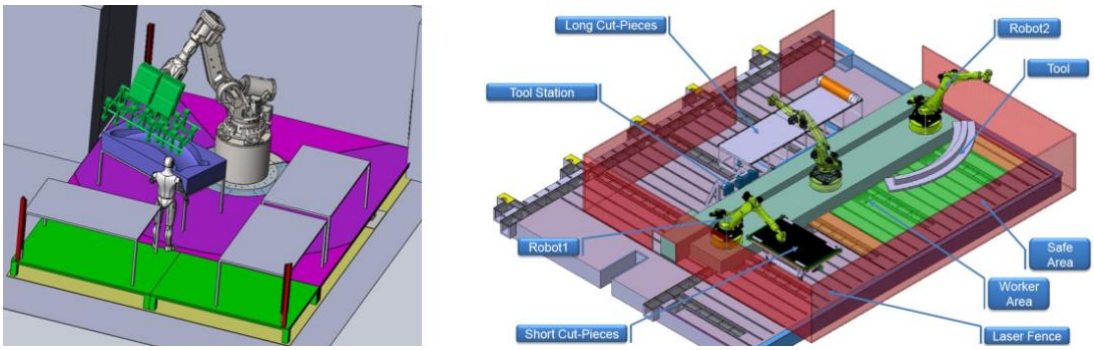

Fig. 1: Isometric views of compact workcell layout (left) and certification ready industrial workcell (right)

Across all three scenarios, industrial-scale robots were employed, each with a reach of approximately three meters and a payload capacity of 250 kg. To address different process requirements, and particularly the different approaches to certified safety, two distinct workcell designs were implemented (Figure 1). In the aerospace case, a workcell featuring two robots mounted on a shared linear axis was used, allowing coordinated motion across the entire workspace. This setup featured certified safety devices, such as light curtains and laser scanners, to monitor critical zones for human presence. If any safety boundary was breached, these systems would immediately disable robot movement in accordance with established safety protocols.

In contrast, the automotive and maritime case studies were carried out within a more compact workcell layout, featuring a single stationary robot positioned at the centre. This setup required careful arrangement of cell components to ensure accessibility and practical safety but still enabled efficient human-robot collaboration within the process requirements. Moreover, the compact design allowed for easy relocation of the workcell between the factories of the end users.

All robots were equipped with custom-built gripper systems, that consisted of interchangeable vacuum- and needle-based grasping modules mounted on a structural grid. This modular design allowed the grippers to be

DOI: https://doi.org/10.26799/cp-polymers-composites-3Bsmaterials-2025

adapted to the specific material requirements of each manufactured part. In addition, multiple optical sensors specialized in fibre angle measurement were integrated into the grippers, providing real-time feedback on fibre orientation to support precise material placement and alignment.

4. Modes of Collaboration and Interaction

Different collaboration and interaction strategies were evaluated through a structured analysis across three distinct domains: material transport, draping and Human-Robot Interaction. In the transport domain, the chosen mode of collaboration depended on both the size of the ply and the capabilities of the workcell. For smaller plies, autonomous robotic transport proved effective. In contrast, larger plies were either transported autonomously by two synchronized robots or handled collaboratively by a robot and human operator. In the collaborative case, a camera-based feedback loop adjusted the robot's motion in response to material deformations caused by the human operator. This effectively allowed the human to guide the robot through the workcell in real time.

In the draping domain, the robotic system was responsible for the initial placement and fixation of the ply. Where the target geometry of the part required more precise manipulation, the human operator completed the task by performing delicate manual adjustments to ensure proper adaptation to complex surface features (Figure 2).

Fig. 2: Human-robot collaboration during draping (left, right) and transport (centre)

Human-Robot Interaction was based on gesture and voice commands expected at key positions within the process. In the simplest form, such commands were used to continue with the process execution or to select the next step out of multiple possibilities. In more complex cases a gesture could also provide additional input for a requested task, such as the position where a fibre angle measurement must be performed for documentation purposes. In the other direction, the robotic system also provided real-time feedback and instructions to the operator through a display mounted on the gripper.

5. Results and Analysis

The collaborative approach demonstrated clear technical advantages across all three case studies. Key requirements of each application were consistently fulfilled and HRC resulted in higher accuracy and repeatability compared to purely manual draping. Economically, the implemented approach improved productivity by up to 47% in terms of process costs, highlighting its potential for industrial adoption. However, it is important to recognize that draping does not occur in isolation, but rather as part of a broader manufacturing workflow. In an industrial context upstream and downstream processes, such as material delivery and impregnation, significantly influence the overall efficiency and cost-effectiveness of the production line. Without a corresponding level of automation in these adjacent stages, the economic advantages do not scale across the entire process chain.

With respect to human-robot interaction, the effectiveness of gesture and voice commands depended strongly on context and system responsiveness. When naturally integrated into task-specific interactions, these methods improved efficiency significantly. Conversely, unnecessary or unnatural use of these interaction modes hindered rather than enhanced productivity. A representative example of an intuitive gesture is the natural movement involved in picking up a ply from a table, which aligns well with task intent (Figure 3). In contrast, a gesture such as clapping the hands overhead to signal process abortion was perceived as unnatural. Additionally, immediate and intuitive system feedback proved essential for maintaining effective two-way communication. This enabled

DOI: https://doi.org/10.26799/cp-polymers-composites-3Bsmaterials-2025

operators to understand the robot's intentions and contributed to greater trust and user acceptance of the collaborative system.

Fig. 3.: Examples of good natural gestures: pick (left) and point (centre) and bad unnatural movements: abort (right)

The studies also highlighted substantial limitations imposed by current safety regulations. Existing standards require either large protective zones or drastically reduced robot operating speed when humans are nearby, diminishing the potential benefits of close collaboration. In the experimental workcell, where standard safety boundaries were intentionally exceeded, a more natural and fluid collaboration was observed. However, reliance on an additional supervising operator to ensure safety, as was possible within the controlled context of these studies, is neither practical nor sufficiently safe for industrial applications. The lack of advanced, intelligent safety frameworks capable of dynamically adapting to collaborative scenarios emerged as a critical barrier for industrial integration.

6. Conclusions

Human-robot collaborative draping presents significant opportunities to enhance the accuracy, repeatability, and efficiency of composite manufacturing processes. However, the benefits of automation were limited when upstream and downstream processes remained manual, indicating that integrated automation beyond the draping task itself is essential for achieving economic viability.

Current safety standards posed a substantial constraint on effective collaboration, primarily by enforcing reduced robot speeds and introducing unnecessary idle times. This highlights the need for more intelligent, context aware safety certification frameworks that support dynamic human-robot interaction without compromising operator safety. Gesture and voice-based commands proved effective only when embedded naturally within the task flow, enhancing collaboration without adding complexity or requiring unnatural movements. To fully realize the potential of collaborative draping in industrial settings, future efforts should focus on improving intelligent safety mechanisms, fostering greater system integration across the production chain and refining intuitive interaction strategies.

Acknowledgements

This work was co-funded by the federal state of Upper Austria and the European Regional Development Fund (EFRE) under the grant VRoboCoop in the programme IWB 2021-2027. This project has also received funding from the European Union's Horizon 2020 research and innovation programme under grant agreement No 101006732.

References

1. S. Das, J. Warren, D. West, and S. M. Schexnayder, *Global Carbon Fiber Composites Supply Chain Competitiveness Analysis*, Golden, CO: Clean Energy Manufacturing Analysis Center (CEMAC), May 2016.
2. M. Yang *et al.*, "A cooperative mobile robot and manipulator system (Co-MRMS) for transport and lay-up of fibre plies in modern composite material manufacture," *Int. J. Adv. Manuf. Technol.*, vol. 119, pp. 1249–1265, 2022.

Proceedings of the Polymers, Composites, 3BsMaterials 2025 Joint International Conferences
AlBufeira, Portugal – April 16 – 18, 2025
DOI: https://doi.org/10.26799/cp-polymers-composites-3Bsmaterials-2025

Design and Optimization of Sandalwood Composites for Personalised 3D-printed Arm Fracture Fixation Braces Using Finite Element Analysis

Yashi Zheng[1], Cristina Vallés[2], Eddie Whitehouse[3], Chamil Abeykoon[1, *]
[1]Northwest Composites Centre and Henry Royce Institute, Department of Materials, Faculty of Science and Engineering, The University of Manchester, Oxford Road, M13 9PL, Manchester, UK (Email: chamil.abeykoon@manchester.ac.uk)
[2]Department of Materials, National Graphene Institute and Henry Royce Institute, University of Manchester, Oxford Road, M13 9PL, Manchester, UK
[3]Faculty of Science and Engineering and Henry Royce Institute, University of Manchester, Oxford Road, M13 9PL, Manchester, UK

Abstract
Personalised 3D-printed orthoses have gained significant attention in the field of biomedical engineering, offering patient-specific devices that facilitate precise alignment and efficient recovery. However, traditional materials used in orthotic fabrication often lack biocompatibility, antimicrobial properties, and sustainability. To address these limitations, this study explores the use of sandalwood-reinforced polylactic acid (PLA) filaments, leveraging sandalwood's natural antibacterial, anti-inflammatory, and bioactive properties to enhance patient comfort and healing efficiency. For arm fracture treatment, a 3D scanning process was conducted to capture the patient's limb geometry, followed by reverse engineering-based modelling to design a customised arm brace. The fabrication process involved sandalwood powder-reinforced composite synthesis, followed by filament extrusion, and FDM 3D printing of the arm brace. The mechanical performance of the brace was evaluated using finite element analysis (FEA), incorporating topology optimization to assess the effects of different thicknesses and topological shapes. The optimised design successfully achieved a balance between strength and stiffness, thereby enhancing patient comfort by minimizing unnecessary bulk and rigidity. This study highlights the potential of biocompatible and functionalised 3D-printed orthoses, paving the way for the next generation of lightweight, antimicrobial, and customized orthopedic supports.

Keywords: Sustainable 3D printing filaments, Natural Filler-Reinforced Composites, FDM 3D Printing, Finite Element Analysis, Structure Topology Optimization, Biomedical Applications.

1. Introduction

In recent years, personalised three-dimensional (3D) printing technology has garnered significant attention in biomedical engineering, providing patient-specific solutions that improve alignment, rehabilitation efficiency, and overall comfort [1]. In particular, Fused Deposition Modelling (FDM) has revolutionised rapid prototyping and the cost-effective manufacturing of medical devices, enabling the customisation of orthopedic braces, implants, tissue engineering scaffolds, drug delivery systems, and surgical tools [2-4]. By leveraging precise 3D scanning and computer-aided design (CAD) capabilities, 3D printing offers tailored solutions that significantly enhance clinical outcomes. Traditional plaster casts, commonly used for fracture treatment, are often associated with discomfort and skin irritation; in contrast, personalised 3D-printed braces provide improved breathability and comfort through optimised designs featuring ventilation holes and variable thicknesses, while also simplifying the manufacturing process and reducing costs [5]. Despite these advancements, most current 3D-printed medical devices utilise synthetic polymer filaments that may lack the desired biocompatibility, antimicrobial properties, and environmental sustainability. To address these limitations, this study focuses on developing a fully sustainable and biodegradable composite filament reinforced with natural fillers, particularly sandalwood powder. Sandalwood is known for its hardness, durability, and water resistance and inherent bioactive properties, including anti-inflammatory, antioxidant, antiviral, and antibacterial effects conferred by its α-santalol and β-santalol components [6].

DOI: https://doi.org/10.26799/cp-polymers-composites-3Bsmaterials-2025

These bioactive compounds contribute to the biocompatibility of sandalwood-reinforced composites, `making them suitable for use in contact with the human body. Moreover, its biodegradability renders it an eco-friendly alternative to conventional petroleum-based polymers. This study focuses on developing and optimizing a sandalwood-reinforced biodegradable composite filament for personalised 3D-printed orthopaedic braces. By employing FEA simulation, the research aims to refine the structural design of the brace to enhance mechanical performance, load-bearing capacity, and patient comfort while reducing material consumption and environmental impact.

2. Methodology

2.1 Materials

Polylactic acid (PLA) Luminy® LX175 (TotalEnergies Corbion, Netherlands) was selected as the polymer matrix, with a density of 1.24 kg/cm³, a tensile modulus of 3500 MPa, a tensile strength of 53 MPa, a melting temperature of 155 °C, and glass transition temperature (T_g) of 60 °C. Sandalwood powder was procured from VedaOils, UK, and was used as a natural reinforcement for the fabrication of a PLA composite material containing 10 wt.% loading of sandalwood, which was chosen based on its superior mechanical properties compared to other filler loadings, compiled in Table 1.

Table 1: Mechanical properties of 10 wt.% sandalwood-reinforced PLA composite.

Young's modulus (MPa)	Ultimate tensile strength (MPa)	Yield strength (MPa)	Poisson's ratio
14.47	46.52	10.3	0.4

2.2 Sustainable sandalwood-reinforced filament fabrication process

The 10 wt.% sandalwood-reinforced PLA composite was fabricated by melt blending in a twin-screw extruder. Following extrusion, the composite was pelletized and oven-dried and then processed into filaments with a diameter of 1.75 mm ± 0.3 mm using a filament extruder. 3D-printed samples were finally fabricated from the extruded filaments using the FDM 3D printer [7]. The composite fabrication process is shown in Fig. 1.

Fig. 1: Process followed to fabricate 10 wt.% sandalwood powder-reinforced composite filaments.

2.3 Design procedure

The design process for the arm fixation brace involved several key steps, as schematically shown in Fig. 2. First, a high-resolution 3D scanner captured the limb's data, which was then imported into CAD software for model refinement. Using reverse engineering software (Fusion 360), a customized brace was developed to match the patient-specific limb geometry. The finalized model was exported as an STL file and processed in a slicing software for 3D printing. The brace was printed using FDM technology, followed by post-processing steps such as edge smoothing and surface finishing to ensure optimal fit and functionality.

DOI: https://doi.org/10.26799/cp-polymers-composites-3Bsmaterials-2025

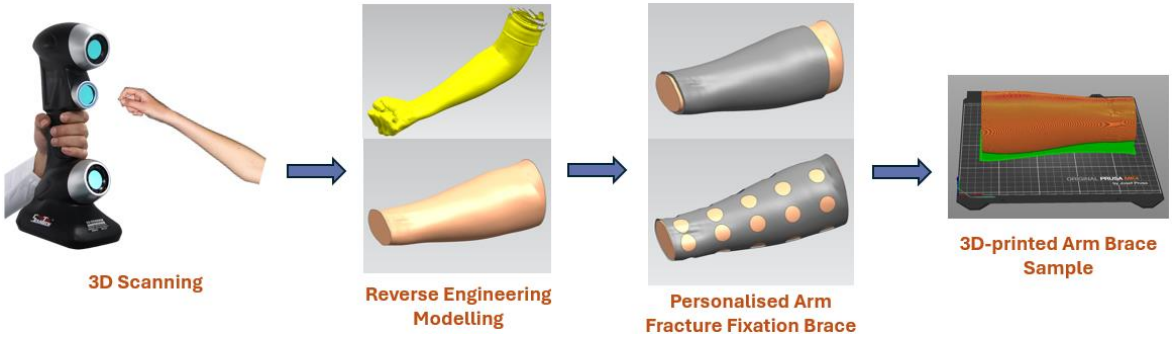

Figure 2: Process followed to design a personalized 3D-printed arm fracture brace.

2.4 Finite element analysis

To evaluate the mechanical performance of the 3D-printed fracture fixation brace, a finite element analysis (FEA) was conducted. The 3D model of the brace was first imported into the FEA software for simulation. For simplification purposes, the model was treated as a single integrated structure, without considering the assembly constraints that would be required in practical fabrication. The meshing process was performed using tetrahedral elements, which are well-suited for complex geometries and provide accurate stress distribution predictions. The next step involved simulating the load conditions experienced by the brace when worn by a patient. This was done to ensure that the brace could provide sufficient structural support while minimizing excessive deformation. To replicate real-world conditions, boundary conditions were carefully defined. This setup allowed for an accurate assessment of the brace's deformation response and stress distribution, ensuring its effectiveness in stabilizing fractures under realistic loading conditions.

3. RESULTS AND DISCUSSION

3.1 Effect of different thicknesses on the structural performance of the limb brace

The mechanical performance of the 3D-printed arm brace was evaluated for varying thickness (1 mm, 2 mm, and 3 mm) using FEA under a deformation limit of 10%-20 %. Considering that the average limb diameter is approximately 52 mm, a reasonable thickness range will be between 5.2 and 10.4 mm. As shown in Table 2, there are inverse relationships between the brace thickness and both the maximum displacement and the Von Mises stress. Specifically, increasing the thickness from 1 to 3 mm was found to reduce the displacement from 50.91 to 0.90 mm, and the stress from 1.79 to 0.22 MPa. These simulation results indicate that thinner braces exhibit higher localized stress concentrations and a greater level of deformation under identical loading conditions, whereas thicker braces seem to provide better load distribution and enhanced mechanical stability. This observation is consistent with classical beam bending theory, which states that flexural rigidity scales with the cube of the thickness [8]. However, an excessively thick brace may increase the material's weight, potentially compromising the patient's comfort. The safety factor, calculated as the ratio of material yield strength to maximum Von Mises stress, transitions from "Unsafe" at 1 mm to "Safe" for thicker designs (2 and 3 mm). This finding indicates that a 1 mm brace does not provide sufficient cross-sectional area to effectively distribute the applied load, thus exceeding the permissible stress threshold of the sandalwood-reinforced PLA composite. In contrast, the 3 mm thick design demonstrates optimal performance and stress below the material's yield strength, ensuring the patient's safety under physiological loading conditions.

Table 2: The stresses (Von Mises) and displacement obtained for the arm brace's different thicknesses.

Thickness of arm brace (mm)	Maximum displacement (mm)	Max Mises stress (MPa)	Safety factor
1	50.91	1.79	Unsafe
2	7.44	0.48	Safe
3	0.90	0.22	Safe

3.2 Effect of different topological shapes on the structural performance of the limb braces

DOI: https://doi.org/10.26799/cp-polymers-composites-3Bsmaterials-2025

Table 3 compares the mechanical responses of three topological shapes, including circular, rectangular, and hexagonal. The hexagonal brace exhibited the lowest maximum displacement (5.13 mm) and Von Mises stress (0.40 MPa), outperforming the circular (6.29 mm and 1.22 MPa) and rectangular (6.81 mm and 2.19 MPa) designs. This superiority can be attributed to the hexagonal geometry's inherent structural efficiency, characterized by a uniform stress distribution across its tessellated edges and vertices. The symmetry of the hexagon minimizes localized stress concentrations, a phenomenon observed in rectangular designs, where sharp corners act as stress risers. The circular brace, while avoiding sharp edges, still shows higher stress values compared to the hexagonal design, suggesting that curvature alone does not fully mitigate stress concentrations under asymmetric loading conditions. The hexagonal topology's performance was found to align with biomimetic principles typically observed in natural structures, such as honeycombs, which optimize the strength-to-weight ratios through tessellated geometries.

Table 3: The stresses (Von Mises) and displacement for the different shapes of arm brace.

The shape of the arm brace	Maximum displacement (mm)	Max Mises stress (MPa)	Safety factor
Circle	6.29	1.22	Safe
Rectangle	6.81	2.19	Safe
Hexagon	5.13	0.40	Safe

4. Conclusions

This study demonstrates that both the thickness and topology of 3D-printed orthopaedic braces critically influence their structural performance. Compared to traditional plaster casts, this natural filler-reinforced composite is more environmentally friendly. Also, after its service life, it can be further degraded or recycled, contributing to sustainable resource utilization. The design methodology is not limited to the upper limb, it can also be adapted for other areas such as the hand, ankle, lower leg, and knee. Potential applications include the knee joint, a region that is prone to wear and is particularly vulnerable, especially for athletes. Additionally, this material holds promise for various biomedical applications, including custom clinical devices, tissue engineering, bone replacement scaffolds, prosthetic sockets, orthotic devices, drug delivery systems, and surgical and implantable devices.

Acknowledgements

The authors gratefully acknowledge the technical support provided by Andrij Zadoroshnyj, and Nathan Bailey in conducting the experimental work.

References

[1] E.M.M. Van Lieshout, M.H.J. Verhofstad, L.M. Beens, J.J.J. Van Bekkum, F. Willemsen, H.M.J. Janzing, M.G. Van Vledder, Personalized 3D-printed forearm braces as an alternative for a traditional plaster cast or splint; A systematic review, Injury 53 Suppl 3 (2022) S47-S52.
[2] S.A.V. Dananjaya, V.S. Chevali, J.P. Dear, P. Potluri, C. Abeykoon, 3D printing of biodegradable polymers and their composites – Current state-of-the-art, properties, applications, and machine learning for potential future applications, Progress in Materials Science 146 (2024) 101336.
[3] V.K. Tiwary, A. P, A.S. Deshpande, N.J.R.P.J. Rangaswamy, Surface enhancement of FDM patterns to be used in rapid investment casting for making medical implants, 25(5) (2019) 904-914.
[4] C. Wang, W. Huang, Y. Zhou, L. He, Z. He, Z. Chen, X. He, S. Tian, J. Liao, B.J.B.m. Lu, 3D printing of bone tissue engineering scaffolds, 5(1) (2020) 82-91.
[5] S. Shaikh, 3D Printing Applications in Orthotic Braces: Upper Body and Lower Body, 3D Printing in Prosthetics and Orthotics: Innovations and Opportunities, Springer2024, pp. 91-104.
[6] S. Banerjee, S. Banerjee, S. Bose, S. Banerjee, U. Chakraborty, Healing Benefits of Indian Sandalwood (Santalum album L.), Medicinal Spices and Herbs from India, Apple Academic Press2024, pp. 375-398.
[7] C. Abeykoon, P. Sri-Amphorn, A. Fernando, Optimization of fused deposition modeling parameters for improved PLA and ABS 3D printed structures, International Journal of Lightweight Materials and Manufacture 3(3) (2020).
[8] R.R. Craig Jr, E.M. Taleff, Mechanics of materials, John Wiley & Sons, 2020.

Proceedings of the Polymers, Composites, 3BsMaterials 2025 Joint International Conferences
AlBufeira, Portugal – April 16 – 18, 2025
DOI: https://doi.org/10.26799/cp-polymers-composites-3Bsmaterials-2025

GRAM®, THE WINDING TECHNOLOGY FOR SPACE STRUCTURES

G. Pommatau [(1)], D. Macieira [(2)], B. Bonvoisin [(3)]

[(1)] Thales Alenia Space, 5 allée des Gabians, 06156 Cannes La Bocca Cedex, France, gilles.pommatau@thalesaleniaspace.com,

[(2)] GRADEL LightWeight SARL, 5 rue Bommel, L-4940 Hautcharage, LUXEMBOURG, d.macieira@gradel.lu

[(3)] ESA – ESTEC, European Space Research & Technology Centre
Postbus 299 2200 AG Noordwijk THE NETHERLANDS
benoit.bonvoisin@esa.int

KEYWORDS

Composite, Carbon fiber, Additive Manufacturing, Mechanical Performance, Finite Element Analysis, Experimental Tests, Robotic, Additive Manufacturing, GRAM®.

ABSTRACT

The well-known endless continuous fiber winding technology has now been robotized to become GRAM® technology, for Gradel Robotized Additive Manufacturing. This paper synthesizes the recent developments of this innovative technology applied to a lightweight antenna supporting structure for a satellite application. The design to manufacturing engineering methodology will be presented. Then, it will be discussed the microscale fiber/matrix physical tests, the part manufacturing process and the results of mechanical and thermo-mechanical tests obtained on the part. Finally, thanks to the experience gained on this development, the conclusion will pre-sent the different foreseen applications for space structures.

1. INTRODUCTION

1. Context

The decrease of mass, without stiffness decrease, of any part of spacecraft is one of the obsessions of space structure designer. Even if manufacturing traditional ply-by-ply lay-up technology of composite allows performing structures, which do respond to such a problematic, it is generally shape limited to relatively simple but large shapes, such as monolithic plates, flat panels, tubes, or cylinder. In parallel, the metallic additive manufacturing Laser Powder Bed Fusion processes has now reached flight, i.e. Technology Readiness Level 9, with increasing complexity in shapes, but keeping some limitations in size of parts due to powder bed machines. The here proposed GRAM® technology (for Gradel Robotized Additive Manufacturing) brings together the advantages of a very high specific stiffness, the thermo-elastic stability of unidirectional carbon fibers reinforced composites, and the ability to generate large and complex 3D shapes. GRAM® process consists in winding resins pre-impregnated carbon fiber filament around interfaces, pre-designed and positioned in space. Curing is performed afterwards. The continuous winding fiber manufacturing process has been automated by GRADEL LW. GRAM® allows the manufacturing of large size parts, including a well-controlled repeatable quality control impregnation system in the robot's head, which ensure good material health and reproducibility. Winding strategy has been optimized taking into account the industrial robot performances.

This paper mainly presents the different thermomechanical tests performed from elementary samples up to one-scale parts and ends with the space applications for which this technology would generate interesting industrial gains,

2. Background

In 2020, GRADEL SARL, under supervision of ESA (European Space Agency) & LSA (Luxembourg Space Agency), in collaboration with LIST (Luxembourg Institute for Science & Technology) & Thales Alenia Space France, led the development of GRAM® technology in order to qualify and produce space parts. Thanks to robotization efforts, GRAM® was developed and a separated entity GRADEL LW (for Light Weight) was created in March 2022. GRAM® process is a robotic additive manufacturing process developed by GRADEL LW using continuous endless fibers combined with a binder. The new made GRAM® structures for space applications are pre-calculated, optimized, modelled, and thermo-mechanically tested. Correlation between the virtual and physical results is performed. Thales Alenia Space France supplies all specifications and

DOI: https://doi.org/10.26799/cp-polymers-composites-3Bsmaterials-2025

requirements in order to be space qualified.

3. Objectives

The main objective of the study is to push up the TRL (Technology Readiness Level) and the MRL (Manufacturing Readiness Level) of the GRAM® technology up to TRL6 and MRL6, taking a classical space use-case of secondary structure, i.e. a lightweight Tele-Metry and Tele-Command (TMTC) antenna support shown on Figure1, respecting Thales Alenia Space France requirements.

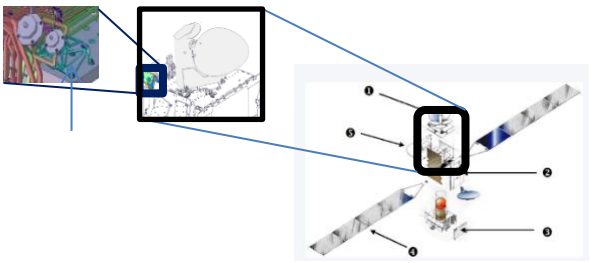

Fig.1: Location of a earth TMTC antenna support on a spacecraft structure

2. SPACE APPLICATION

1. Preliminary mass analyses

From an industrial point of view, it was necessary to assess the gains foreseen by the introduction of such an innovative technology on satellite platforms. Thus, a mass budget has been performed, assuming a stiffness being sufficient to comply with the classical requirement of a first Eigen-frequency above 140Hz on rigid interfaces. Thales Alenia Space France provides a comparison of different technologies based on its heritage, given in the Table1. The reference is the historical design for Thales Alenia Space France, not implemented for years, which consisted in assembling sandwich structures, brackets, and stiffeners. A simple evolution has consisted in a monolithic metallic machined part. The three next evolutions are results of Additive Manufacturing (AM) powder bed coupled with topological optimization. Only the one without lattice has been qualified for flight, as other additive manufactured secondary structures in Thales Alenia Space [1]. The two others were manufactured and tested in the frame of ESA studies in collaboration with Thales Alenia Space [2].

	Historical	Manually optimized + machined	Topological optimization + AM	Optimized with µlattice only in AM	Optimized structure + µlattice in AM	xFK 3D
						
Mass saving	0% (ref)	30%	40%	6%	40%	≈ 70%
Drawbacks	Cost (M&P) Difficult to adjust	Not optimized	N/A	Lattice management	Lattice management	To be qualified
Advantages	Large flight heritage	Standard low cost material	Adjustable design **Flight qualified**	Adjustable design	Adjustable design	Adjustable design

Table1: Comparison of mass savings and advantages and drawbacks of different technologies that can be implemented for a TMTC antenna support

The Table1 clearly exhibits a real mass saving interest for implementing GRAM® technology on space substructures and justify the work for increasing TRL of this technology.

2. Requirements

Thales Alenia Space France provided requirements for an example of TMTC antenna support. A design space has been delivered considering internal elements to be added during Integration (antennas, wave-guides, screws), and accessibility space for the integration of these elements.
Tolerances of interface locations, and functional interfaces (flatness and roughness), thermal range, mass and mechanical strength and stiffness are also required. With such requirement, GRADEL has developed its methodology, in association with elementary tests.

3. GRAM® METHODOLOGY

GRAM® digital approach consists in the following activities: firstly analysing the design space allocated between mechanical interfaces, then performing a topological optimization, selecting a winding pattern and plan, and finally simulating via a Finite Element Model the thermo-mechanical behaviours of the part.

DOI: https://doi.org/10.26799/cp-polymers-composites-3Bsmaterials-2025

GRAM® hardware approach is performed in parallel to digital approach, since inputs for Finite Element Model such as materials properties are extracted from GRAM® manufactured and tested specimens, Manufacturing parameters are masterized, such as material and processes applied to fiber and resin (rheology, winding, curing), metallic interface sensitivities, and health controls. Elements that must be focused on are the winding path associated with tooling and robotic programming.

1. Design of the GRAM® part

The GRAM® part's design started by considering the requirements and allowable work volume. Using the thermo-mechanical extracted GRAM® composite material properties, it enables the design of GRAM® parts, which also must consider the robotic manufacturing constrains.

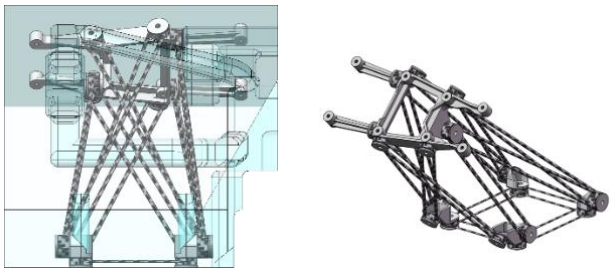

Fig.2: Overview of available design space with GRAM® structure inside

The thermomechanical material parameters were extracted from pre-designed specimens with different winding configuration to enable the Topology and Finite Element Analysis.

2. Design of the bushings

The bushings are considered as the interface parts, which will connect the fibers and unify the structure. They can be made of any materials depending on the environment requirements. Due to the compressive force induced by the torque applied to the screws at the bottom, the interfacings between the antenna support and the other parts of the satellite had to be made in metal, especially aluminium because of lightweight and large heritage. As the two antennas are close to each other and due to the given work volume restrictions, it has been decided to use a single aluminium bushing to connect the winding. The winding architecture has been centred on the 8 antenna's screws in order to avoid the imposed forbidden volumes, due to adjacent components crossings.

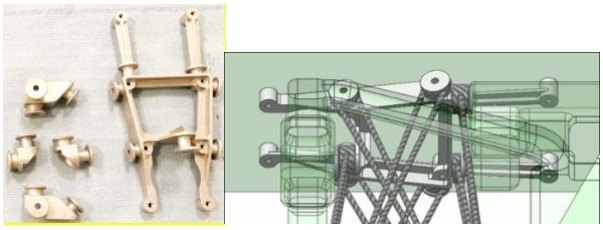

Fig.3: Overview of Anodized bushings before winding (left) & forbidden volume (right)

In total, the TMTC antenna support consists in 5 bushings and 13 fiber arms.

3. Winding syntax

The winding syntax considers and defines how many turns must be made around bushings, so that the material resistance be compliant with the requirements. In this project, the winding configuration was chosen for mass saving, with the lowest mechanical resistance and stiffness. For other applications, multiple winding syntax can be applied to optimize strength and/or stiffness and reduce additional mass. In this GRAM® TMTC antenna

DOI: https://doi.org/10.26799/cp-polymers-composites-3Bsmaterials-2025

support, winding syntax was used with three different winding cycles.

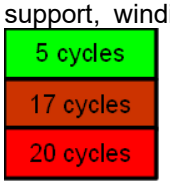

Fig.4: Overview of the Winding Syntax

GRADEL developed a "Winding Table", an in-house program, which automatically calculates the accumulation on each interface of the bushings. The inputs are the number of bushings, the number of connections of each, the coordinate, the height, and the internal diameter of each connection.

4. FABRICATION AND CONTROL

1. Materials and Robot

All the used materials are already space qualified by Thales Alenia Space and already possess flight heritage. For these space bracket materials used are aluminium 7075T7351, High resistance T300 6K carbon fibers and RTM6 epoxy resin. A specific Tartaric Sulphuric Acid anodizing (TSA) surface treatment for bonding has been applied to bushings, in addition to standard degreasing.

To enable the fabrication of parts with GRAM®, different considerations must be considered directly during engineering phase of the part. For example, a space of 15 mm must be freed around each bushing's interface in order the robot to be able to wind the part.

2. Manufacturing

GRAM® process requires the design of a tooling or mould to be adapted to the winding process so that connection between bushings can be made. Different physical parameters during the tooling design phase must be considered like the difference of Coefficient of Thermal Expansion (CTE) between the elements of the part and the tooling itself. This generally implies the use of carbon tooling, as shown in Figure5.

Specimens of 100mm for mechanical testing with the representative winding configuration were manufactured before and after the winding of the GRAM® TMTC antenna support. This approach was made to check via mechanical tests the god material health along the processing/manufacturing time of the antenna support. However, the results will not be presented here.

The following manufacturing parameters has been used for the manufacturing of GRAM® TMTC antenna support:
Process temperature: 80 °C,
Max winding speed, 100 mm/s
Min winding speed, 30 mm/s

DOI: https://doi.org/10.26799/cp-polymers-composites-3Bsmaterials-2025

Fig.5: Overview of the GRAM® TMTC antenna support wound part before curing

To wind a GRAM® TMTC antenna support, it took approximatively 20 minutes. A tool allows winding and curing three GRAM® TMTC antenna support in the same time (see Figure5). Curing of parts is performed in GRADEL LW facility, near the robot, in a large oven. Use of RTM6 requires reaching 180°C by two stages.

3. Post-Manufacturing Treatments

After winding and curing process of the GRAM® TMTC antenna support, the latter are disassembled from tooling. No special post-manufacturing treatments has been performed in a worst-case approach.

5. ENVIRONMENTAL TESTS

1. Hygro-thermal accelerated ageing

The hygro-thermal accelerated ageing test of six GRAM® TMTC antenna supports has been performed for seven days at e.g. 95% RH and 45°C in Thales Alenia Space facility in Cannes. This is representative of many years in integration class ISO8 room controlled temperature and hygrometry.

2. Thermal Cycling

After hygro-thermal accelerated ageing the GRAM® TMTC support has been subjected to thermal cycling test, i.e. 100 cycles [-70°C: +150°C]; heating ramp: +2°C/min; cooling ramp: -2°C/min, with a set point during 5min at each -60°C and 140°C. Two of the six parts were equipped with two thermocouples: one on the top and one on the bottom of the sample, see Figure6.

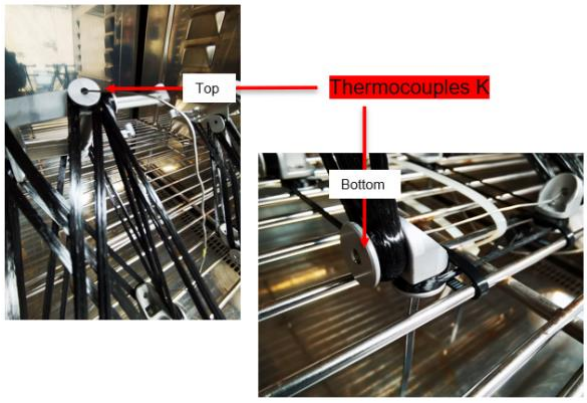

Fig.6: Thermocouple equipment of the bushing during thermal cycling

After thermal cycling, no failure neither delamination has been observed. Note that, due to thermal inertia and too short 5min dwell, hot temperature reached was only +140°C (requested +150°C) and cold temperature reached was only -60°C (requested -70°C).

DOI: https://doi.org/10.26799/cp-polymers-composites-3Bsmaterials-2025

6. STATIC UNIAXIAL TRACTION AND COMPRESSION MECHANICAL TESTS

Six GRAM® parts has been tested at Luxembourg Institute of Science & Technology (LIST) under unidirectional X, Y, & Z axial loads. The following test conditions were applied:

- Tensile machine: Instron5967
- Test speed: 1 mm/min, all screws tighten with torque wrench.

Three of the six parts were tested after ageing, three other were tested unaged.
Thales Alenia Space France requirement is to withstand the load of [-140N; 140N] in the three-coordinate direction X, Y & Z. At the load requirement level, the applied load under different direction has been subjected to loading and unloading at different, to be able to visualise if the structure recovers integrity and if no damage happened at these loads.

1. Tests along +Z and -Z axis

The GRAM® TMTC antenna support has been subjected to “tensile” (+Z) and “compressive” (-Z) loads mounted on the static mechanical tooling described in Figure7. It shows the Force vs Displacement curve for +Z and -Z until 500N, exhibiting a linear behaviour, and confirmed the integrity of the structure which is compliant with requirements.

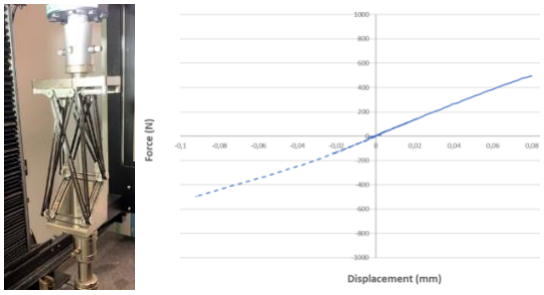

Fig.7: +Z and –Z static mechanical test (left: setup under tensile machine, right: until +500N)

When loaded until 3000N, the unaged specimen exhibits the same linear behaviour. When loaded above 3000N, many failures occurred, synonymous of delamination identified by drops in the load vs displacement curve, as presented in Figure8.

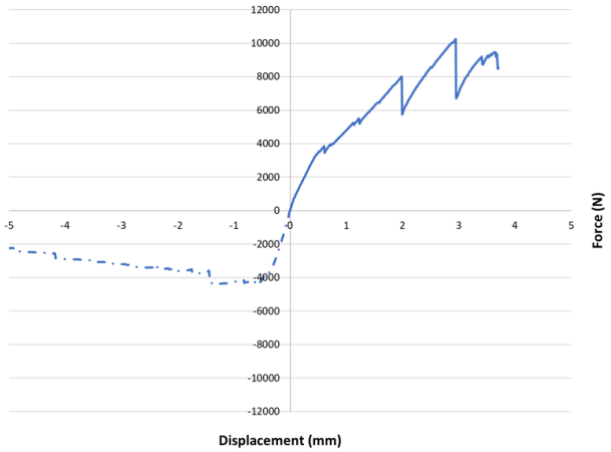

Fig.8: +Z and –Z static mechanical test until rupture of unaged specimen

Based on Figure7 and Figure8, one can conclude that the GRAM® TMTC antenna support can withstand tensile and compressive loads in Z direction without failure until 3000N.

2. Tests along +Y and -Y axis

The GRAM® TMTC antenna support has been subjected to +Y and -Y loads mounted on the tooling described in Figure9. It shows the Force vs Displacement curve for +Y and -Y until 140N, exhibiting a linear behaviour, and confirmed the integrity of the structure which is compliant with requirements.

DOI: https://doi.org/10.26799/cp-polymers-composites-3Bsmaterials-2025

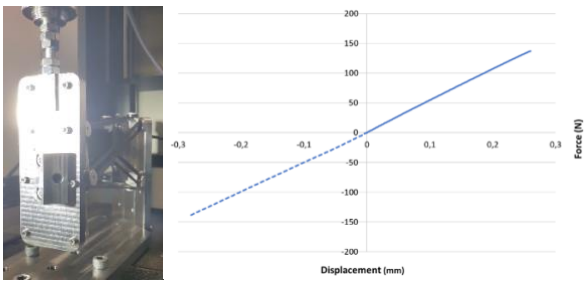

Fig.9: +Y and –Y static mechanical test (left: setup under tensile machine, right: until +140N)

When loaded until 300N in traction +Y, the unaged specimen exhibits the same linear behaviour without residual strain. When loaded above 300N until 900N, a linear behaviour is observed with a different slope. Above 900N, many failures occurred, synonymous of delamination identified by drops in the load vs displacement curve, as presented in Figure10.

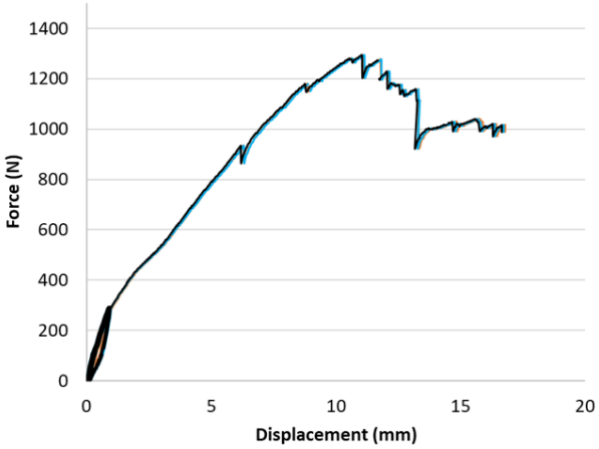

Fig.10: +Y static mechanical test until rupture of unaged specimen

Under +Y, -Y direction, the obtained results have confirmed the integrity of the structure and is compliant with requirements.

Based on Figure9 and Figure10, one can conclude that the GRAM® TMTC antenna support can withstand without failure in a linear behaviour, compressive load in –Y direction until at least 140N, and tensile loads in +Y direction until 300N.

3. Tests along +X and -X axis

The GRAM® TMTC antenna support has been subjected to +X and -X loads mounted on the tooling described in Figure11. It shows the Force vs Displacement curve for +X and -X until 140N, exhibiting a bi-linear behaviour, and confirmed the integrity of the structure which is compliant with requirements.

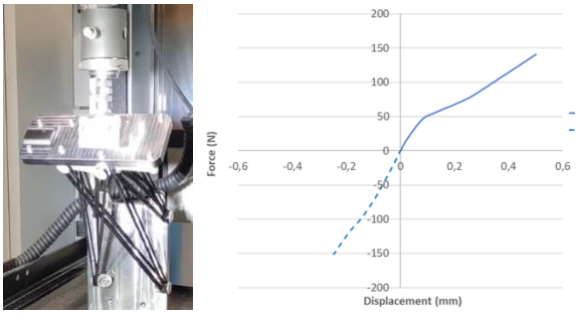

Fig.11: +X and –X static mechanical test (left: setup under tensile machine, right: until +140N)

When loaded until 900N, the unaged specimen exhibits the same bi-linear behaviour, without identified failure but inducing residual displacement, as shown in the load vs displacement curve, presented in Figure12.

DOI: https://doi.org/10.26799/cp-polymers-composites-3Bsmaterials-2025

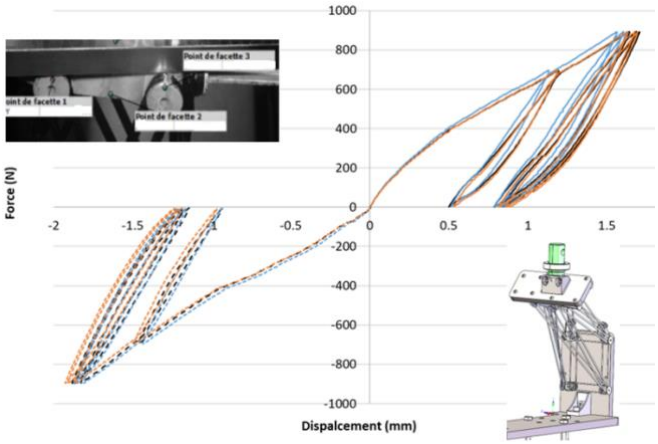

Fig.12: +X and –X static mechanical test (left: setup under tensile machine, right: until +900N unaged specimen)

Under +X, -X direction, the obtained results have confirmed the integrity of the structure above the required loads. It has been observed in Figure11 a mechanical slight change at 50N in +X direction, associated to an internal preload in the part, and a unsymmetrical stiffness behaviour of +X direction w.r.t. –X direction, which led to the introduction of two different stiffness in the FEM, one in traction, one in compression, along fiber axis.

7. DYNAMIC VIBRATION TESTS

During launch, such a support is loaded under dynamic vibrations. Thus, the dynamic behaviour of the GRAM® TMTC antenna support, ie modal analysis and acceleration level without damage has to be verified along the three axis. Thus, three GRAM® parts has been tested under unidirectional X, Y, & Z axial vibrations. The following test conditions were applied: two antenna mass dummies were screwed on the part and supported accelerometers. Part was clamped on a cube interface that allows loading in the three directions, while the shaker works only in axial mode, as presented in Figure13.

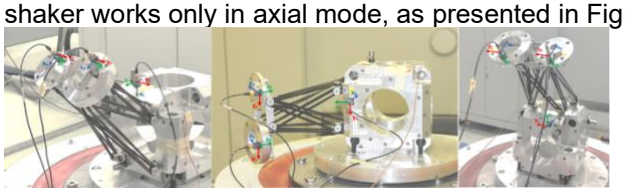

Fig.13: X, Y and Z (from left to right) vibration test set-up

Test sequence consisted in modal analysis at low acceleration level, followed by sweep at higher level for detection of first damage in the different load directions. An additional test has been performed to quantify resistance to fatigue.

1. Modal analysis

Three modal analysis have been performed based on the comparison of the 3 first modes obtained during the 3 direction low level (1g) sweep at 2octave/min in the range [5Hz,600Hz], with corresponding Finite Element modal Analysis.
Test results are presented in Figure14, FEM results are presented in Figure15, and Table2 shows that the 3 first modes are well correlated to FEM results

DOI: https://doi.org/10.26799/cp-polymers-composites-3Bsmaterials-2025

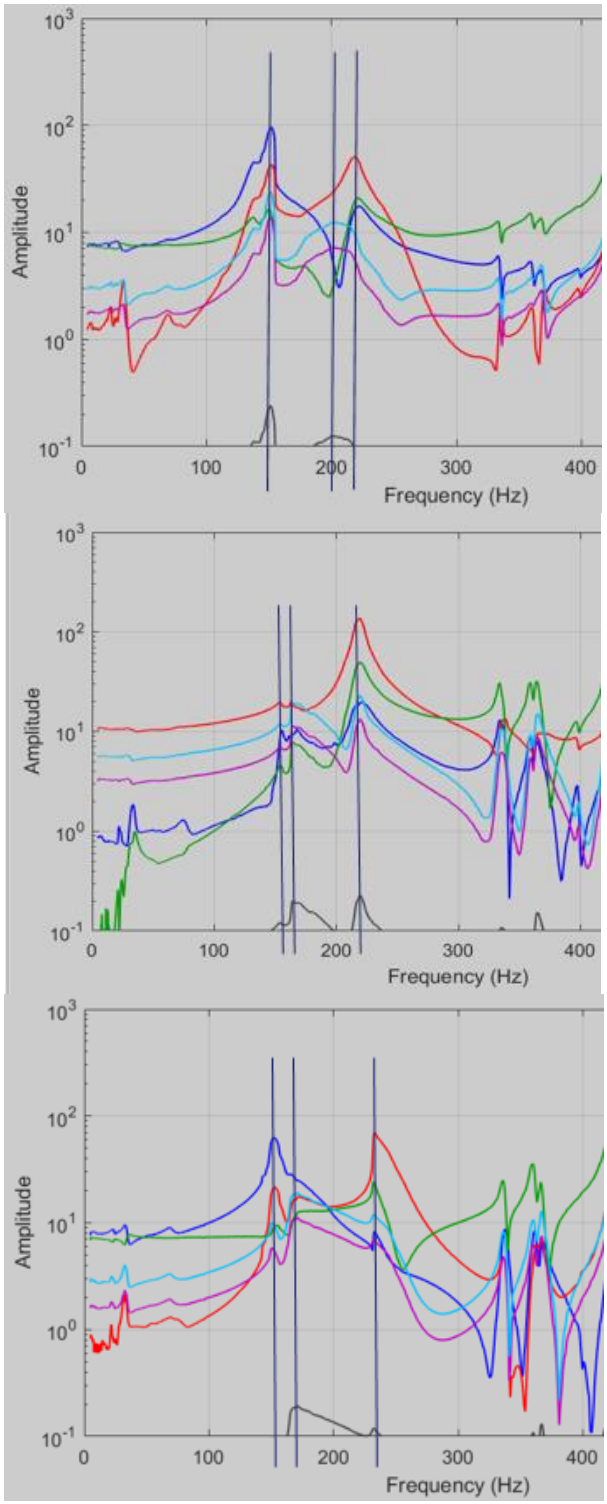

Fig.14: Accelerations measured during low-level sweep, which revealed the 3 first modes, when loaded in X, Y and Z direction (from top to bottom)

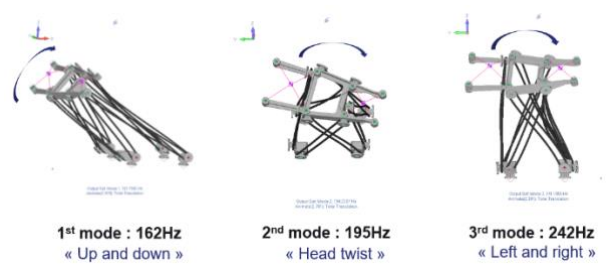

Fig.15: Three first modes shapes obtained by FEM

DOI: https://doi.org/10.26799/cp-polymers-composites-3Bsmaterials-2025

FEM		1g at basis 2oct/min		
Mode	Frequency	X vibration	Y vibration	Z vibration
Up and down	162	152	155	152
Head twist	195	201	163	171
Left and right	242	218	220	233

Table2: Comparison of mode frequencies (Hz) obtained by FEM and by sweep tests

Table2 exhibits that a slight difference do exist between FEM and test results, which can be explained by a non-linear behaviour in the shape of acceleration curves at 1g. This has been confirmed by additional sweep performed at lower level, which revealed a change in frequency modes between 0.2g and 1g, as presented in Figure16, and allows concluding that FEM is well correlated in stiffness at very low level.

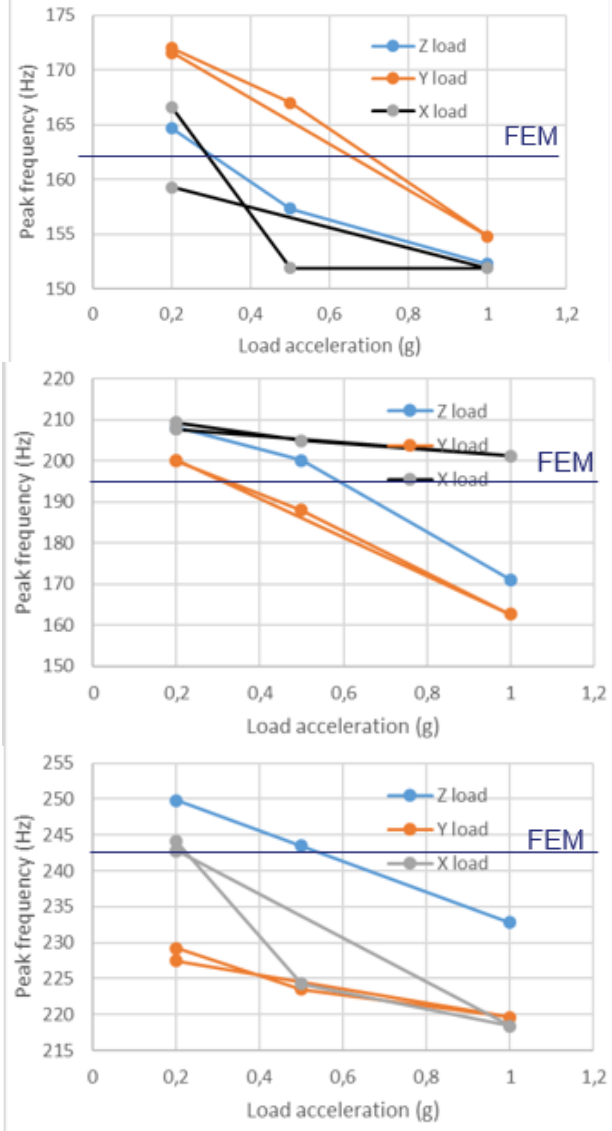

Fig.16: Nonlinearity of test results exhibited by comparison of Eigen-frequencies with FEM ones of first (top), second (middle) and third (bottom) modes.

2. Very high level sweep test on first mode along X vibration

The objective of the test was to reach, as worst case, the required 40g acceleration in quasi-static at antennas by sweeping on the modes. For that, increasing the acceleration at the base and measuring acceleration at antenna dummies on the modes gave the transfer function. For a vibration along X at 2.5g, the first mode (detected at 158Hz) allowed to reach a level of 42g at antenna dummies without damage since low-level sweeps did superimposed to initial ones.

DOI: https://doi.org/10.26799/cp-polymers-composites-3Bsmaterials-2025

3. Very high level sweep test on third mode along Y vibration

For a vibration along Y at 2.5g, the third mode (detected at 163Hz) allowed to reach a level of 47g at antenna dummies. In this case, a slight shift of the low-level frequency of -4Hz on the first and third mode (initially at 172Hz and 226Hz respectively), is detected after 2g (which corresponds to 34g at antenna dummies). Note that the second mode is surprisingly not affected. This correspond to an out-of-plane issue at interfaces (unscrewing), which are not implicated in second mode. The low amplitude of resonant peak and the necessity of re-torqueing screws at interfaces after physical check confirmed this.

4. Very high level sweep test on first mode along Z vibration

For an applied vibration at 3g along Z, the first mode (detected at 161Hz) allowed to reach a level of 50g at antenna dummies during sweep. No damage was detected because low-level sweeps performed afterwards did superimposed to initial ones.

DOI: https://doi.org/10.26799/cp-polymers-composites-3Bsmaterials-2025

5. Fatigue test at 160Hz with 3 high levels along Z vibration

Based on the previous results obtained without damage along Z at 50g, a fatigue test has been performed at a frequency of 160Hz, very near the first mode detected at 161Hz, generating 40g at antenna dummies. After 25min, 2.10^5 cycles have been reached without damage (proven by low-level control sweep). Level has then been increased up to 60g (2.10^4 cycles) and 70g (2.10^4 cycles). Too high vibrations have released sensors during test and delamination has been observed afterwards. Damage is confirmed by low-level significant frequency shift on first and third mode, respectively -13Hz and -55Hz, as shown on Figure17.

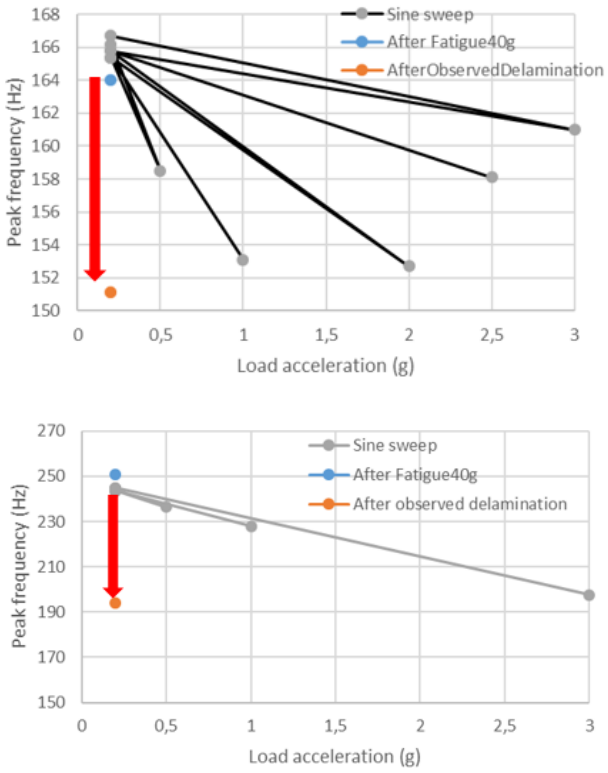

Fig.17: Low-level frequency shift of first mode (top) and third mode (bottom)

Anyway, it has been proven that the part can sustain 40g in Z direction on a “up and down” mode without fatigue after 2.10^5 cycles. This validate the strength requirement of 40g in launch quasi-static load.

8. THERMOELASTIC STABILITY TESTS

During flight, such an antenna support, external appendix of the structure, is loaded by thermal changes due to different solar lighting. Thus, the thermoelastic distortion of the GRAM® TMTC antenna support has to be verified. Because this kind of antenna is roughly omnidirectional, pointing requirement is not stringent, so that distortion of some tenth of millimetres is acceptable.

TMTC antenna support has been screwed on inserts bonded in a satellite representative aluminium structural sandwich panel. Displacement measurement has been performed with Digital Image Correlation through the window of an oven, as presented in Figure18. A low CTE sample of Zerodur® was located near for system calibration.
Unfortunately, in this oven, the measurement was not possible at negative temperature, since condensation occurs on the windows. Thus measurements have been performed on [25°C; 175°C] range.

DOI: https://doi.org/10.26799/cp-polymers-composites-3Bsmaterials-2025

Fig.18: TMTC antenna support mounted on sandwich aluminium panel and Zerodur reference sample equipped with thermocouples inside the oven.

Two runs of measurement have been performed, one for each plane facing the cameras through the window, lateral (Figure19) and axial (Figure20) configurations.

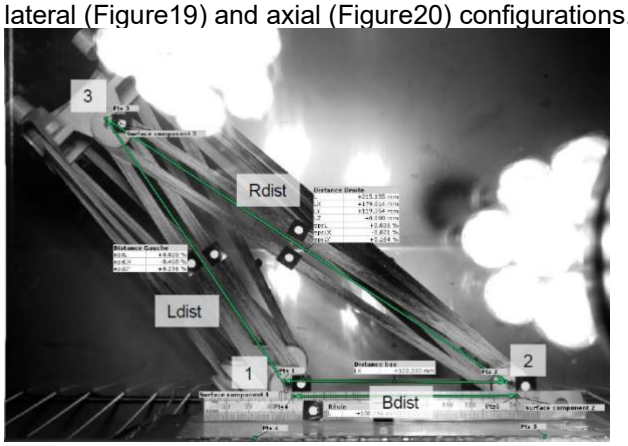

Fig.19: TMTC antenna support equipped with targets for Digital Image Correlation measurement in lateral configuration.

Thanks to the displacement of the bonded targets measured by the two cameras of the Digital Image Correlation, it is possible to deduce the expansion of the two carbon double bars branches represented as Ldist, Rdist in the Figure19, Bdist being the space between two feet of the bracket, screwed in the aluminium skin sandwich.

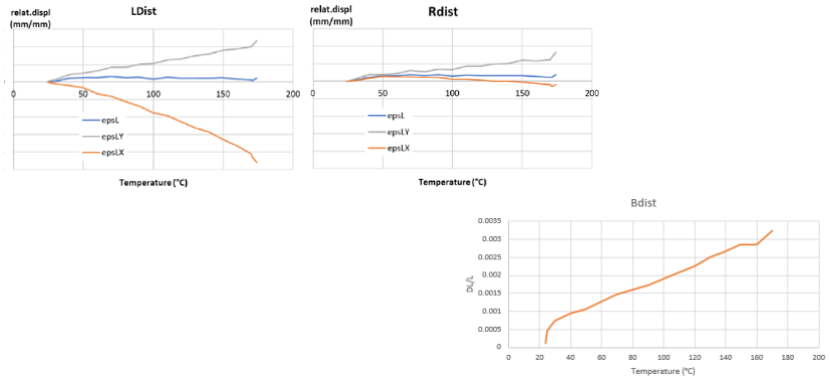

Fig.20: Expansion measurement results of the three main branches of the TMTC antenna support equipped with targets for Digital Image Correlation measurement.

The results exhibits a near-zero CTE (<2µm/m/°C) along the carbon double bars, blue curves in Figure20.

DOI: https://doi.org/10.26799/cp-polymers-composites-3Bsmaterials-2025

Calculated CTE from Bdist measurement reach the value of 22µm/m/°C, in accordance with aluminium sandwich expansion.

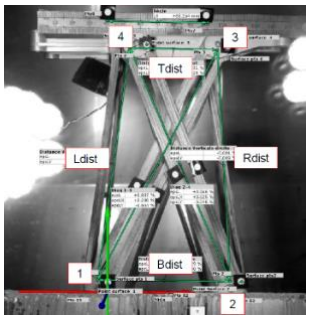

Fig.21: TMTC antenna support equipped with targets for Digital Image Correlation measurement in axial configuration.

Thanks to the displacement of the bonded targets measured by the two cameras of the Digital Image Correlation, it is possible to deduce the expansion of the different distance. The two carbon double-bar branches are represented as Ldist, Rdist, in the Figure20, Tdist and Bdist being respectively the length of metallic antenna support baseplate and the space between two feet of the bracket, screwed in the aluminium skin sandwich.

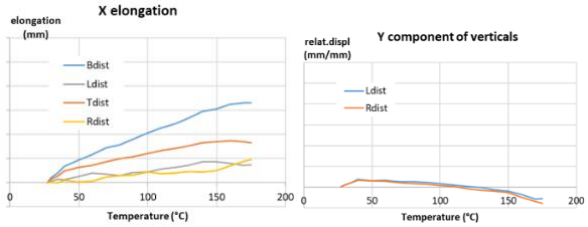

Fig.22: Expansion measurement results of the four main branches of the TMTC antenna support equipped with targets for Digital Image Correlation measurement.

The results exhibits a near-zero CTE (<2µm/m/°C) along the carbon double bars Ldist and Rdist, in Figure22, whereas Bdist and Tdist are, in accordance respectively with aluminium sandwich expansion and baseplate lowered by carbon branches expansion.

9. CONCLUSION

Based on elementary test results obtained on GRAM® composite material [1][2], GRADEL designed the GRAM® TMTC antenna support to withstand mass, frequency and stress requirements provided by Thales Alenia Space France. GRADEL managed to manufacture several lightweight TMTC antenna support of 170gr. Static mechanical tests performed after ageing and thermal cycling showed that the part could sustain at least above 500N under compression & traction in the three different axis without any physical damage. Vibration tests confirmed Finite Element Analysis, and first mode appears above 140Hz. Failure by delamination has been reached above 40g, without sensitivity to the number of cycles until 2.10^5 cycles. Thermoelastic tests was performed on [25°C; 175°C] temperature range and showed that small distortions are due to the CTE of the sandwich aluminium panel on which the TMTC antenna support is screwed.

10. EXTENSION TO OTHER SPACE APPLICATIONS

Enlighted by the good results obtained in the frame of this study, Thales Alenia Space France has identified industrial interest for this technology in three main applications. Serial secondary structures (such as the present antenna support) can gain lead-time thanks to robustness and robotization of the process. Large structures with high stiffness and reduced cost can be addressed thanks to lightweight of the product. Stable structures can be made with this technology by the high stiffness, the low CTE and CME thanks to the use of carbon fiber oriented along load path.
Additional ways of interest are the in-orbit manufacturing thanks to the high degree of robotization of carbon preform, or natural fibre products for sustainability issues.

11. ACKNOWLEDGEMENTS

The authors wish to acknowledge European Space Agency (ESA) & Luxembourg Space Agency (LSA) for

DOI: https://doi.org/10.26799/cp-polymers-composites-3Bsmaterials-2025

their support via the Luxembourg National LuxIMPULSE programme.

DOI: https://doi.org/10.26799/cp-polymers-composites-3Bsmaterials-2025

12. REFERENCES

1. Pommatau, G., Macieira, D., Perrin, H. (2022) Sustainable Robotic Manufacturing of Lightweight Metamaterials, *Journées Européennes des Composites,* Paris 2023.

2. Pommatau, G., Macieira, D., Perrin, H., Bonvoisin, B. (2023) GRAM® Technology, the most efficient way to optimize mass of space structures, *Proceedings of the European Conference on Spacecraft Structures Materials and Environmental Testing,* Toulouse 2023.

3. Pommatau, G. (2024), GRAM® Technology, the most efficient way to optimize mass of space structures, *Worldwide Advanced Manufacturing Symposium*, Orlando 2024.

4. Macieira, D. (2024), GRAM®, the multidimensional winding technology, *Worldwide Advanced Manufacturing Symposium*, Orlando 2024.

Proceedings of the Polymers, Composites, 3BsMaterials 2025 Joint International Conferences
AlBufeira, Portugal – April 16 – 18, 2025
DOI: https://doi.org/10.26799/cp-polymers-composites-3Bsmaterials-2025

Fabrication of Hydrogel Composite for Tissue Engineering Applications; incorporating Magnetite Nanoparticles

Anet Vadakken Gigimon, Hatim Machrafi, Patrick Hendrick, Carlo S. Iorio
Centre for Research and Engineering in Space Technologies (CREST), ATM, Université Libre de Bruxelles (ULB), Brussels, Belgium, anet.vadakken.gigimon@ulb.be

Abstract

Tissue engineering is an interdisciplinary field that utilises three main components: cells, scaffold or support structure and growth factors for tissue regeneration. In physiological conditions, the support structure that enables cell growth and promote cellular functions is known as the extracellular matrix (ECM). Among the biomaterials used to mimic the ECM, hydrogels are one of the promising scaffolds in use. Natural hydrogels are particularly noted for their biocompatibility, versatility in fabrication, and their capacity to encapsulate cells but they have weak mechanical properties. Here we report the fabrication of self-healing hydrogel composites using non-toxic components like gelatin (Gel) and sodium alginate (SA) as the primary materials. This work also demonstrates the influence of magnetite (Fe_3O_4) nanoparticle incorporation in the stiffness and thermal stability of Gel-SA hydrogel composites. A selected Gel-SA hydrogel concentration was used to obtain multifunctional hydrogel composites (Gel-SA- Fe_3O_4) by incorporating magnetite nanoparticles. The stiffness data and self-healing ability of the Gel-SA and Gel-SA- Fe_3O_4 hydrogels were analysed. The Gel-SA- Fe_3O_4 hydrogel showed a dominant elastic character with enhanced temperature tolerance. This was further utilised to achieve self-healing. The resulting hydrogel composite can be tuned to mimic mechanical properties closer to that of soft tissue ECM.

Keywords: Hydrogels, ECM, composites, self-healing, nanomaterials, mechanical properties, stiffness, temperature tolerance.

1.Introduction

Hydrogels are one of the most promising scaffold materials used in tissue engineering due to their similarities to the extracellular matrix (ECM) of native tissue [1] [2]. Hydrogels mimic the three-dimensional (3D) network structure and moist environment of ECM. Hydrogel scaffolds based on gelatin and alginate for ECM regeneration have gained attention in the recent years due to their excellent properties [3] [4]. These properties include biocompatibility, biodegradability, versatility in fabrication, and their capacity to encapsulate cells and bioactive factors. Moreover, these mixtures enhance the functionalities of the single biopolymer system by combining polymers with different characteristics. Gelatin is derived from hydrolysis collagen, which is a major structural protein [4]. Therefore, gelatin has similar bioactivity of collagen, and it is easily biodegradable under physiological conditions. The sol-gel transition of gelatin and reversible bonds involved can be utilised to achieve self-healing [5]. Alginate is bio-inert and forms a gel in the presence of multivalent cations. However, developing a highly stable and mechanically stiff hydrogel just by utilising solely natural materials is a challenge. Hence, additives or fillers are incorporated in hydrogels to enhance their structural and functional properties [6]. Magnetite nanoparticles are primarily noticed for their magnetic feature and applications in improving the mechanical strength of polymers [7]. In this work, magnetite nanoparticles are incorporated in the Gel-SA hydrogel precursor solution to obtain a multifunctional gel. The effect of nanoparticles on the stiffness, thermal stability and self-healing ability was studied.

2. Materials and Method

2.1. Materials

For this work, sodium alginate, magnetite (Fe_3O_4) nanoparticles and calcium chloride dihydrate were purchased from Sigma – Aldrich (USA). Gelatin was purchased from VWR Life Science (USA).

2.2. Hydrogel Synthesis

DOI: https://doi.org/10.26799/cp-polymers-composites-3Bsmaterials-2025

1. A gelatin-sodium alginate (Gel-SA) was prepared with a 2:1 ratio. For this, 10% (w/v) Gel was mixed with 5% (w/v) SA and dissolved in distilled water. The solution was mixed until homogeneous mixture was obtained. This solution was transferred into a Teflon mold with dog bone shaped sections. Then a 2.5% (w/v) aqueous calcium chloride solution was added, and the samples remained immersed in the solution, for 30 min to crosslink. Finally, the hydrogels were washed 3 times with distilled water to remove any unreacted ions.
2. The gelatin-sodium alginate-magnetite hydrogel (Gel-SA-Fe_3O_4) was prepared by addition of 0.1 % (w/v) Fe_3O_4 nanoparticles to the 2:1 Gel-SA solution, before crosslinking. The solution was stirred until uniform dissolution and then transferred to a mold. Then crosslinked for 30 min using calcium chloride. The hydrogels were washed with distilled water to remove unreacted ions.

2.3. Hydrogel Characterisation

2.3.1. Stiffness test

The stiffness of the hydrogels was analysed using the universal tensile testing machine. Stress (σ) and strain (ε) values were calculated from the force (F) and stroke data ($l - l_0$) obtained from the machine using equations (1) and (2), respectively. Here l_0 denotes the initial length and l indicates the final length.

$$\sigma = \frac{F}{A} \tag{1}$$

$$\varepsilon = \frac{(l - l_0)}{l} \tag{2}$$

Then stress-strain graphs of Gel-SA and Gel-SA- Fe_3O_4 hydrogels were compared to understand the effects of nanoparticle addition on the stiffness. The heating cycle parameters set for stiffness characterisation are the following:

- No heat
- Cycle 1 – Heated at 40 ± 1° C for 10 min
- Cycle 2 – Heated at 40 ± 1° C for 10 min

2.3.2. Healing Test

The healing test was performed to confirm the self-healing property of Gel-SA and Gel-SA- Fe_3O_4 hydrogels. The healing efficiency of Gel-SA hydrogel was discussed in a previous work [5]. Here we followed similar steps, where the hydrogel samples were cut into two parts, whereafter the parts were kept in close contact, followed by heating at 40°C for 10 min.

3. Result

3.1. Stiffness Test

The stress-strain plot below (Fig. 1) indicates that Gel-SA is brittle, and Gel-SA- Fe_3O_4 hydrogel has a dominant elastic behavior. In the case of magnetite incorporated hydrogels, the stress-strain curve of heated samples shows less deviation from the control sample compared to the Gel-SA sample. The Gel-SA hydrogel gets stiffer and more brittle after undergoing the heating cycles. These fluctuations are an indicator of gelatin leakage and hence the hydrogel loses elastic property. However, the Gel-SA- Fe_3O_4 hydrogel maintains the elastic and rigid nature throughout the heating process. The results in figure 1 imply that the magnetite nanoparticles stabilize the Gel-SA system by interacting with the components and avoiding gelatin leakage during heating. Therefore, the addition of magnetite improves the temperature tolerance of Gel-SA hydrogel.

DOI: https://doi.org/10.26799/cp-polymers-composites-3Bsmaterials-2025

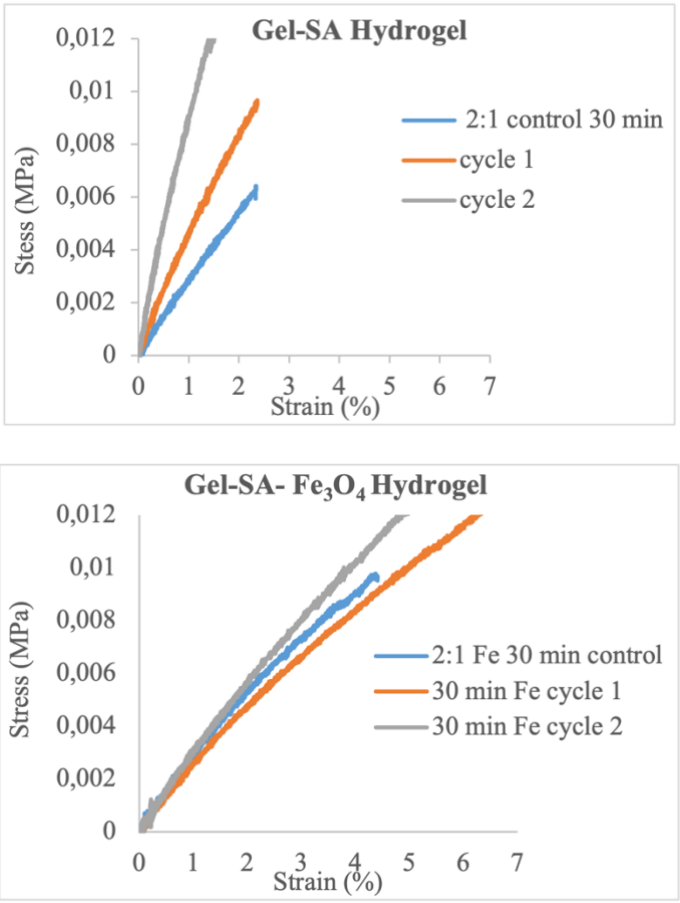

Figure 1. Stress-strain plot of control samples and samples heated for two cycles of Gel-SA (top) and Gel-SA-Fe_3O_4 hydrogels (bottom).

3.2. Healing Test

As observed in Gel-SA hydrogel, the Gel-SA- Fe_3O_4 hydrogel fragments healed themselves and behaved as a single gel when kept in contact after heating (Fig. 2).

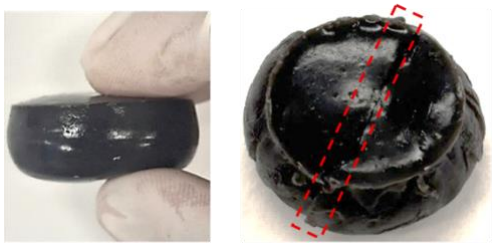

Figure 2. Gel-SA-Fe_3O_4 hydrogel and self-healed fragments in contact to each other at the centre.

When a sample is cut and heated the reversible bonds break and reform. In addition, gelatin undergoes sol-gel transition on heating and then cooling. However, the Gel-SA gel was relatively less stable; the gelatin leakage was observed in a few samples. On the contrary, the Gel-SA- Fe_3O_4 hydrogel fragments were thermally stable as heating did not melt or disrupt the stability of the gel and further improved the self-healing property.

4. Conclusion

Hydrogels with gelatin and sodium alginate (Gel-SA) as major components are promising scaffold materials with similarities to the ECM of native tissue. However, only using natural materials is a challenge when it comes to developing highly stable hydrogels. In this work, magnetite nanoparticles

DOI: https://doi.org/10.26799/cp-polymers-composites-3Bsmaterials-2025

are incorporated as fillers in the Gel-SA hydrogel precursor solution to develop a multifunctional hydrogel composite (Gel-SA- Fe_3O_4). It indeed appeared that the magnetite nanoparticles enhanced the elastic behaviour and temperature tolerance of the hydrogels. Moreover, Gel-SA- Fe_3O_4 hydrogel has a higher thermal stability induced by nanoparticles as hydrogel underwent sol-gel transition during healing test without melting.

Acknowledgements

AVG would like to extend gratitude to FNRS and FWB for their funding support. AVG also like to acknowledge fellow researchers for sharing resources, workspace and referring to relevant resources to facilitate the research.

References

[1] A. Mandal, J. R. Clegg, A. C. Anselmo, and S. Mitragotri, "Hydrogels in the clinic," *Bioengineering & Translational Medicine,* vol. 5, no. 2, 2020.

[2] T. J. McKee, G. Perlman, M. Morris, and S. V. Komarova, "Extracellular matrix composition of connective tissues: a systematic review and meta-analysis," *Scientific Reports,* vol. 9, no. 1, p. 10542, 2019.

[3] X. T. Le, L.-E. Rioux, and S. L. Turgeon, "Formation and functional properties of protein–polysaccharide electrostatic hydrogels in comparison to protein or polysaccharide hydrogels," *Advances in Colloid and Interface Science,* vol. 239, pp. 127-135, 2017.

[4] J. Alipal, N. A. S. Mohd Pu'ad, T. C. Lee, N. H. M. Nayan, N. Sahari, H. Basri, M. I. Idris, and H. Z. Abdullah, " A review of gelatin: Properties, sources, process, applications, and commercialisation.," *Materials Today: Proceedings,* vol. 42, p. 240–250, 2021.

[5] I. Greco, A. V. Gigimon, C. Varon, A. M. Bogdanova, and C. S. Iorio, "Temperature induced self-healing properties of alginate gelatin hydrogels," *Materials Letters,* vol. 363, p. 136315, 2024.

[6] M. Mehrali, A. Thakur, C. P. Pennisi, S. Talebian, A. Arpanaei, M. Nikkhah, and A. Dolatshahi-Pirouz, "Nanoreinforced Hydrogels for Tissue Engineering: Biomaterials that are Compatible with Load-Bearing and Electroactive Tissues.," *Advanced Materials,* vol. 29, no. 8, 2017.

[7] M. Bustamante-Torres, D. Romero-Fierro, J. Estrella-Nuñez, B. Arcentales-Vera, E. Chichande-Proaño, and E. Bucio, "Polymeric Composite of Magnetite Iron Oxide Nanoparticles and Their Application in Biomedicine: A Review," *Polymers,* vol. 14, no. 4, p. 752, 2022.